Politecnico di Torino

Politecnico di Torino

Master's Degree in Biomedical Engineering

Ultrasonic Array Evaluation for a Wearable Biofeedback Device for Speech and Language Therapy

Supervisor:

Prof. Filippo Molinari

Co-supervisors:

Prof. Silvia Seoni
Prof. Sandy Cochran

Candidate:

Alessia Bruno

Academic Year 2025/2026

Graduation Session July 2026

In collaboration with

Abstract

Wearable ultrasound devices for head and neck could transform how speech and language therapists monitor and treat patients. They are a promising point-of care solution which represents an opportunity to move healthcare beyond traditional clinical environments. Rather than requiring hospital visits, these devices would allow continuous, non-invasive monitoring during everyday life and home-based rehabilitation, giving clinicians a much clearer long-term picture of how dysphagia patients' muscles and swallowing function over time. However, transitioning bulky hospital ultrasound equipment to ergonomic, wearable configurations introduces significant technical challenges in relation to hardware and acoustic restraints. High-frequency (HF) sound waves struggle to penetrate tissue effectively and physical constraints severely limit the space available for the sensing components, due to limited transducer apertures.

This thesis establishes the technological foundations for a wearable ultrasound device, focusing on the hardware integration, electrical interfacing, and experimental validation of a 14 MHz HF linear array transducer. The primary engineering challenge addressed is the architectural channel mismatch between the 192-element transducer aperture and the 128-channel limitation of the Verasonics Vantage 128 research platform. This constraint was addressed through the design of a custom 64-channel flexible printed circuit board (fPCB) interfacing board routed with controlled 50 Ω impedance matching to maximise signal integrity, keeping signal quality high and minimising interference between channels. This direct routing strategy achieved a sub-nanosecond propagation delay mismatch; it effectively mitigated beamforming phase errors and suppressed inter-channel crosstalk, preventing image distortion and reducing interference between signals, all without requiring complex serpentine trace geometries.

The baseline performance of the selected 14 MHz rigid array was evaluated against alternative HF configurations to justify its selection. Several alternative arrays were tested and ultimately rejected. A 25 MHz flexible array had manufacturing defects and unreliable performance (severe element dropout), while a 28 MHz rigid array could not image deep enough into tissue layers, suffering excessive acoustic attenuation.

A progressive testing pipeline was followed to ensure experimental validation. Testing moved from acoustic characterisation on tissue-mimicking phantoms to dynamic fluid imaging within a custom oesophageal stenosis model, before concluding with imaging sessions on cadaveric specimens at the University of Glasgow Anatomy Facility.

A comparative image processing framework was established using MATLAB scripts; this ensured a quantitative foundation for this analysis. This post-processing

pipeline, which operated on the reconstructed B-mode images, enabled the evaluation of image quality and acoustic penetration performance. The results confirmed that the 14 MHz probe successfully optimises the physical trade-off between spatial contrast resolution and effective deep penetration under highly attenuating conditions, striking the best balance between image clarity and depth of penetration.

In conclusion, this work delivers a verified hardware-software baseline. It provides a solid, validated technical foundation for future integration into fully conformable wearable systems and long-term clinical patient monitoring.

Table of Contents

List of Tables VI

List of Figures VII

List of Abbreviations XII

1 Introduction 1
- 1.1 Clinical and Technological Context . . . 1
  - 1.1.1 The Clinical Challenge: Dysphagia Post-Head and Neck Cancer 1
  - 1.1.2 The Rehabilitation Framework: Speech and Language Therapy and Ultrasound . . . 2
  - 1.1.3 The Engineering Solution: The Need for Wearable Ultrasound Monitoring . . . 2
- 1.2 Aims and Objectives of the Project . . . 2
- 1.3 Thesis Outline . . . 3

2 Technical Background 5
- 2.1 Ultrasound Imaging . . . 5
  - 2.1.1 Theoretical Principles . . . 6
  - 2.1.2 Nature of Ultrasound and Wave Propagation . . . 6
  - 2.1.3 Acoustic Impedance and Reflection: Interaction with Tissues 7
    - Energy Dissipation: Attenuation and Loss . . . 9
  - 2.1.4 The Resolution–Penetration Compromise . . . 9
  - 2.1.5 Ultrasound Transducers and the Piezoelectric Effect . . . 9
  - 2.1.6 B-mode Image Formation . . . 10
  - 2.1.7 Signal Processing and Display . . . 11
- 2.2 Anatomy of the Neck and Dysphagia . . . 12
  - 2.2.1 Physiology of Swallowing . . . 13
  - 2.2.2 Head and Neck Cancer and Related Dysphagia . . . 14
    - Pharyngo-oesophageal Strictures in HNC Patients . . 16
  - 2.2.3 Ultrasound Landmarks in the Submental Region . . . 17

Swallowing Structures 17
Scanning Planes and Probe Positioning 19
Detection of Dysphagia 19
2.3 Speech and Language Therapy 20
2.3.1 Clinical Context and Rehabilitation 21
2.3.2 Ultrasound Biofeedback 22
2.3.3 Transition to Point-of-Care and Wearable Ultrasound 22
USES Procedure and Instrumentation 23
2.4 Validation Models for Ultrasound Imaging 25
2.4.1 Tissue-Mimicking Material Phantoms 26
2.4.2 Cadaveric Specimens 27
2.5 Image Quality Metrics 28
2.5.1 Signal-to-Noise Ratio (SNR) 28
2.5.2 Contrast-to-Noise Ratio (CNR) 29
2.5.3 Maximum Penetration Depth (MPD) 29
2.6 Coded Excitation and Beamforming 29
2.6.1 Coded Excitation 30
2.6.2 Beamforming Framework and Performance Trade-offs 31

3 Design and Integration of the 14 MHz Flexible Interface 33
3.1 Transducer Selection and System Rationale 34
Evaluation of Preliminary Prototypes 34
3.2 Transmission and Data Acquisition System: Verasonics Vantage 128 36
3.3 14 MHz Transducer Characteristics 36
Technical Specifications 36
Physical Architecture and Connection Tabs 36
Interfacing Requirements 37
3.4 Hardware Architecture 37
3.4.1 Layout Constraints and Signal Integrity 38
Impedance Control and Trace Geometry 38
Routing Strategy and Crosstalk Mitigation 40
3.4.2 Material Specifications and Stackup 41
3.5 Preliminary Electrical Characterisation 41
3.5.1 Measurement Setup and Technical Challenges 42
3.5.2 Observations and Experimental Constraints 42
3.6 Final Assembly and Physical Realisation 43

4 Experimental Validation: From Tissue-Mimicking Phantoms to Cadaveric Specimens 45
4.1 Development of Tissue-Mimicking Phantoms 46
4.1.1 Fabrication Procedure 46

Reference Protocol . . . 47
Experimental Deviations and Observations . . . 48
4.1.2 Preliminary Validation: Plain Phantom . . . 49
4.1.3 Oesophageal Model Design . . . 50
Design Requirements . . . 50
3d-Printing and Casting . . . 50
4.1.4 Ultrasound Imaging Validation . . . 51
Structural Verification with PLA Inserts . . . 52
Acoustic Artifacts from PLA Infill . . . 52
Acoustic Validation and Attenuation Analysis without PLA Inserts . . . 54
Post-Testing Assessment and Long-term Storage . . . 55
4.1.5 Dynamic Bolus Transit Validation . . . 57
Experimental Design and Materials . . . 58
Interface Development: The Sealing Challenge . . . 58
Experimental Setup I and Technical Challenges . . . 59
Experimental Setup II and Optimised Protocol . . . 62
4.2 Validation on Cadaveric Specimens . . . 65
4.2.1 Session I: Baseline Assessment (December 2025) . . . 65
Cadaveric Preparation . . . 66
Imaging Protocol . . . 66
Operational Role and Data Acquisition . . . 66
4.2.2 Session II: 14 MHz Array Validation (March 2026) . . . 66
Custom fPCB Performance . . . 66
Experimental Setup and Integration . . . 66
Clinical Benchmarking . . . 67
4.2.3 Qualitative Ultrasound Analysis and Comparison . . . 67
Low-Frequency Standard vs. High-Frequency Coded Excitation . . . 67
Custom 14 MHz System Performance . . . 67
Clinical Benchmarking (SonixTouch Q^+ System) . . . 68
4.3 Summary of Experimental Results . . . 70

5 Comparative Analysis 72
5.1 Quantitative Evaluation of Prototype Constraints . . . 72
5.1.1 Assessment of the Flexible Prototype Integrity . . . 72
5.1.2 Rigid Array Integrity (14 MHz and 28 MHz) . . . 74
5.1.3 Signal Integrity and Acoustic Penetration Trade-offs . . . 74
5.1.4 Direct Functional Validation of the 14 MHz Array via Imaging Tests . . . 74

5.2 Quantitative Imaging Performance and MATLAB Validation 75
5.2.1 Acoustic Distribution Analysis 75
5.2.2 Axial Signal Intensity Profile and Penetration Depth 77
5.2.3 Summary of Analysis Results 78

6 Conclusions and Future Developments 81
6.1 Impact of the Work 81
6.2 Summary of Final Results 82
6.3 Future Work 83
6.3.1 Preliminary Ergonomic Study and Wearable Band Setup . . 84
6.4 Final Conclusions 84

List of Tables

2.1 Speed of sound in various human tissues and media (data from [8, 9]). 7
2.2 Acoustic impedance values for various human tissues and media (data from [8]). 8

3.1 Geometric and acoustic specifications of the evaluated high-frequency (HF) ultrasound arrays. 35
3.2 fPCB Layer Stack-up and Thickness 42

4.1 Composition of the 2.03 % agar tissue-mimicking material, showing the weight percentage and corresponding mass for each component. 46
4.2 Design parameters for the oesophageal phantom. 50
4.3 Manufacturing specifications for the 3D-printed tooling components. 51

5.1 Quality metrics comparison. 75

List of Figures

2.1 Schematic representation of longitudinal wave propagation. The diagram highlights the areas of compression and expansion (rarefaction), and the fundamental parameters: wavelength (λ) and amplitude (adapted from [10]). 7

2.2 Schematic representation of the pulse-echo principle, illustrating the interaction between the incident beam and acoustic interfaces (adapted from [6]). 10

2.3 Comparison of scan formats: (A) linear, (B) curved, and (C) sector/phased array. The linear format (A) is preferred for neck imaging as it provides a uniform rectangular field of view (adapted from [11]). 11

2.4 Reconstruction of a B-mode image from raw ultrasonic data. The process illustrates how individual A-mode signals (right) are converted into grayscale scan lines (middle) and then integrated to form the complete 2D B-mode anatomical map (left) (adapted from [12]). 12

2.5 Midsagittal section of the head and neck anatomy, showing the primary structures, including the oral cavity, pharynx, larynx, and cervical oesophagus (adapted from [13]). 13

2.6 Biomechanical simulation of the swallowing process stages. The sequence illustrates the bolus transit from the oral phase (A-B) through the pharyngeal phase (C-D-E) and into the oesophageal phase (F), highlighting the coordination of the tongue, hyoid bone, and laryngeal structures (adapted from [15]). 15

2.7 Progression of pharyngo-oesophageal injury post-chemoradiotherapy: (A) acute mucositis, (B) cicatricial scarring with partial narrowing, and (C) complete pharyngo-oesophageal stricture (PES) (adapted from [18]). 17

2.8 Anatomical representation of the submental muscular complex. These muscles play a crucial role in swallowing and serve as the structural basis for measuring muscle thickness and displacement via ultrasound (adapted from [21]). 18

2.9 Transverse submental ultrasound view mapping the primary suprahyoid musculature and anatomical landmarks for swallowing assessment (adapted from[6]). 19
2.10 Ultrasound detection of food residue in different anatomical site: (A) transverse scan showing hyperechoic food residue accumulated within the epiglottic vallecula; (B) visualisation of food residue remaining in the pyriform sinus (adapted from [19]). 20
2.11 The Ultrafit probe stabilisation headset developed by Articulate Instruments in collaboration with Queen Margaret University for ultrasound swallowing and tongue imaging (adapted from [31]). . . 25
2.12 Flowchart of the coded excitation (CE) signal processing chain, illustrating the transmission, reception, and matched filtering stages. 31
2.13 Conceptual representation of the coded excitation (CE) process: (a) the transmitted linear frequency modulated (LFM) chirp signal distributes high energy over a long duration; (b) the matched filter output condenses the echo into a sharp, narrow pulse to maximise the signal-to-noise ratio (SNR) while exhibiting characteristic temporal side-lobes (adapted from [43]). 32

3.1 Comparison of the high-frequency (HF) transducer arrays: the 14 MHz Vermon array (left), the rigid 28 MHz Vermon array (centre), and the flexible 25 MHz Novosound array (right). The ruler highlights the dual-tab architecture and the larger physical footprint of the 14 MHz array compared to the other prototypes (adapted from [47]). 35
3.2 Schematic design of the 64-channel flexible printed circuit board (fPCB) module. The diagram illustrates the pin-mapping strategy between the Samtec SS5 series connector (transducer-side) and the Panasonic AXK5F series connector (system-side). The routing and grounding schemes were implemented to match the specific requirements of the Vermon array tabs and the Verasonics interface cable, respectively, ensuring shielding continuity across the entire signal path. 39
3.3 High-density routing layout of the flexible printed circuit board (fPCB). The red traces represent the copper traces for signals on the top layer, optimised for 50 Ω impedance and maximised inter-channel isolation to mitigate electromagnetic coupling. 40
3.4 Close-up view of the flexible printed circuit board (fPCB) connector region showing the localised rigid stiffener layer underneath the component pads. 42

3.5 Preliminary characterisation phase: (a) laboratory setup for baseline electrical validation using the Keysight E4990A impedance analyser and the Mic-Fi digital microscope; (b) microscopic view of the transducer pins (0.15 mm pitch) during the procedure. 43

3.6 Physical realisation of the custom interface: (a) overview of the soldering quality and mechanical reinforcements of a flexible printed circuit board (fPCB); (b) complete assembly with the 14 MHz transducer connected to two boards. 44

4.1 Phases of tissue-mimicking material (TMM) preparation using the Camlab MS-H280-Pro hotplate: (a) initial mixing stage reached at 75.7 °C; (b) incubation phase with a protective foil seal maintained at 82.9 °C. 48

4.2 Design and pre-experimental setup: (a) Computer-aided design (CAD) model of a conical lumen insert; (b) CAD representation of the external mould housing; (c) visual inspection of the final assembly pre-casting. The setup includes petroleum jelly for easier extraction, elastic bands to maintain axial alignment against the pressure of the hot agar, and sealing clay to prevent leaks at the insert ports. 52

4.3 B-mode ultrasound imaging comparison between high-frequency (HF) and low-frequency (LF) transducers with custom polylactic acid (PLA) inserts in place: (a) the HF probe (15 MHz) is restricted to the superficial layer due to higher attenuation, whereas (b) the LF probe (10 MHz) configuration provides a sufficient field of view to capture the entire stenosis profile. 53

4.4 Visual inspection of the oesophageal phantom after the successful extraction of the 3D-printed lumen inserts. The image confirms the structural integrity of the gel matrix, showing a well-defined, smooth hollow lumen that has not collapsed. 55

4.5 B-mode ultrasound scans of the phantom after insert extraction: (a) the high-frequency (HF) probe (30 MHz) provides high-resolution details of the stenotic tract, whereas (b) the low-frequency (LF) probe (10 MHz) shows the full geometry and the bottom reflection of the mould, with minor interface artifacts visible inside the lumen, possibly due to petroleum jelly residues. 56

4.6 Phantom storage preparation: (a) filling of the lumen with a water-glycerol mixture via a syringe, with the mould tilted to prevent air bubbles; (b) final setup with lateral caps reinforced with modelling clay to ensure a hermetic seal during refrigeration. 57

4.7 Evolution of the phantom-tubing interface: a) first sealing attempt using modelling clay and elastic bands; b) second sealing attempt with custom 3D-printed gaskets. 60

4.8 Initial experimental setup that highlighted critical issues in manual fluid management and circuit geometry: a) pre-filling: tubes positioned vertically using supports; b) post-test: yogurt and water collected in the waste tray after the transit. 61

4.9 Longitudinal ultrasound scan of the oesophageal phantom during the post-transit phase (setup I). The image illustrates two critical limitations of the initial setup: (1) bolus fragmentation, visible as hyperechoic yogurt particles drifting within the lumen instead of a cohesive mass; and (2) acoustic shadowing, visible on the right side of the frame as an opaque artifact caused by air entrapment, which partially obscures the distal portion of the channel. 62

4.10 Optimised experimental setup. The configuration highlights the collaborative protocol and the physical refinements, such as the use of shortened horizontal tubes to minimise gravitational effects and ensure bolus integrity. 63

4.11 Representative ultrasound frames extracted from a video showing the bolus transit dynamics. Despite minor ambient lighting reflections, the interaction between the yogurt bolus and the stenotic geometry is clearly discernible: a) bolus approach; b) bolus compression; c) bolus residuals. The green arrows indicate flow direction (left to right); the yellow scale bar represents an estimated length of 1 cm, derived from a nominal image depth of 4 cm. 65

4.12 Experimental imaging results on a cadaveric specimen from Session I (December): (a) low-frequency (LF) commercial probe (L11-5v) operating in standard mode, displaying deep anatomical landmarks in the submental/laryngeal region; (b) high-frequency (HF) commercial probe (L35-16v) operating at 28 MHz with an 8-cycle coded excitation (CE) chirp; the image is dominated by acoustic shadowing and attenuation, with no structural details discernible below the superficial fascia. 68

4.13 Submental transverse ultrasound scan acquired during Session II using the custom 14 MHz array. The field of view illustrates the successful penetration of the acoustic energy, with multiple hyperechoic lines tracking the horizontal tissue interfaces of the suprahyoid muscles. 69

4.14 Reference submental transverse ultrasound scan acquired using the SonixTouch Q$^+$ clinical system during Session II, acquired at 30 MHz. The high-resolution image clearly delineates the superficial muscular stratification of the neck, alongside a reduction in structural contrast and boundary definition in the deeper regions due to acoustic attenuation. 70

5.1 Experimental element mapping across five distinct prototypes of the 25 MHz flexible array. Green blocks represent fully operational elements, while red blocks indicate dead or disconnected elements resulting from manufacturing failures or structural stress (courtesy of X. Miller). 73
5.2 Reconstructed B-mode ultrasound scans of the stenotic oesophageal phantom: a) L35-16vX commercial probe showing high resolution but severe attenuation limiting depth to 3 cm; b) Custom rigid 14 MHz array demonstrating full acoustic penetration across the entire phantom structure. The depth axes represent an estimated scale based on the known geometric dimensions of the phantom. . . 76
5.3 Acoustic intensity distribution analysis displaying the probability density of the agar wall (red), internal oesophageal channel (green), and background noise (blue): a) L35-16vX Verasonics probe; b) custom rigid 14 MHz array. 77
5.4 Comparison of the axial signal intensity profiles relative to their respective baseline noise floors, displaying the 6 dB safety threshold for Maximum Penetration Depth (MPD) detection: a) L35-16vX Verasonics probe; b) custom rigid 14 MHz array. 79

6.1 Ergonomic and positioning study: (a) transverse (coronal) and (b) longitudinal (mid-sagittal) alignment of the 3D-printed transducer replica secured with an adjustable fabric band to evaluate physical footprint, stability, and contact compliance during dynamic jaw movements and speech production. 85

List of Abbreviations

BAC

benzalkonium chloride.

CAD

computer-aided design.

CE

coded excitation.

CNR

contrast-to-noise ratio.

CRT

chemo-radiotherapy.

CT

computed tomography.

DAS

delay-and-sum.

DFM

design for manufacturing.

FDM

fused deposition modelling.

FEES

fibreoptic endoscopic examination of swallowing.

FFT

fast Fourier transform.

fPCB

flexible printed circuit board.

FTC

freeze-thaw cycle.

GND

ground.

HF

high-frequency.

HNC

head and neck cancer.

HPV

human papillomavirus.

IFFT

inverse fast Fourier transform.

I/Q

in-phase and quadrature.

LF

low-frequency.

LFM

linear frequency modulated.

MDT

multidisciplinary team.

MPD

maximum penetration depth.

MRI

magnetic resonance imaging.

MV

minimum-variance.

NC

not connected.

PES

pharyngo-oesophageal stricture.

PET

positron emission tomography.

PLA

polylactic acid.

POCUS

point-of-care ultrasound.

PVA

polyvinyl alcohol.

RF

radio frequency.

ROI

region of interest.

SLT

speech and language therapy.

SNR

signal-to-noise ratio.

SSD

speech sound disorders.

TGC

time gain compensation.

TMM

tissue-mimicking material.

TW

transmit waveform.

UES

upper oesophageal sphincter.

USB

universal serial bus.

USES

ultrasound evaluation of swallowing.

U-VBF

ultrasound visual biofeedback.

VFSS

videofluoroscopic study of swallowing.

Chapter 1

Introduction

This chapter establishes the foundational framework of this thesis, introduced by evaluating how advanced hardware engineering can address the critical clinical needs of contemporary speech and language therapy (SLT). To map out the development of a point-of-care medical technology, this introduction explores the physiological challenges of dysphagia, particularly in post-oncological cases, alongside the current technological limitations of standard diagnostic equipment. Finally, it outlines the specific engineering aims of the project and provides a comprehensive roadmap of the entire thesis structure.

1.1 Clinical and Technological Context

To contextualise the engineering solutions developed in this work, this section reviews the impact of post-treatment dysphagia, the role of ultrasound in speech rehabilitation, and the technical necessity for wearable monitoring devices.

1.1.1 The Clinical Challenge: Dysphagia Post-Head and Neck Cancer

As a complex physiological process, swallowing is an intricate biological mechanism which relies on the highly synchronised activity of multiple muscle groups and structural tissues. When patients are treated for head and neck cancer (HNC), undergoing therapeutic interventions, including radiotherapy or surgical tumour resection, this coordinated sequence is often disrupted and impaired by severe tissue fibrosis and localised atrophy of muscles, making it difficult or impossible to swallow normally [1]. This condition, defined as dysphagia, can have serious critical complications. Patients are at greater risk of aspiration pneumonia as a result of food or liquid entering the lungs, compromised nutritional intake, and

often experience a profoundly reduced quality of life. In severe cases, chronic tissue degradation can cause permanent structural obstructions within the upper digestive tract, such as cervical oesophageal stenosis, a physical narrowing blocking the passage of food altogether. This requires careful and ongoing clinical assessment and treatment.

1.1.2 The Rehabilitation Framework: Speech and Language Therapy and Ultrasound

Targeted treatment is essential to help patients regain independence and return to normal daily routines [2]. While traditional speech therapy rehabilitation covers a wide range of conditions, modern approaches increasingly use technological tools to monitor the active biomechanics in swallowing. Medical ultrasound has emerged as a useful tool in this area. It is safe, non-invasive, and radiation-free, and it is capable of providing clinicians with real-time evaluation of soft tissue structures [3]. When integrated into a rehabilitative workflow, which aims to optimise patient functioning and minimise secondary disabilities [4], submental ultrasound enables the safe, dynamic visualisation of mouth floor stratification and tongue kinetics, offering immediate visual biofeedback during therapeutic exercises.

1.1.3 The Engineering Solution: The Need for Wearable Ultrasound Monitoring

Although ultrasound imaging offers substantial benefits for SLT, standard diagnostic equipment consists of large, expensive bedside systems that require a highly-trained clinician to manually maintain transducer contact on the patient's neck [3]. This operational constraint severely restricts natural patient movement during speech and swallowing tasks and prevents continuous monitoring. To overcome these limitations and transition ultrasound into a truly accessible, point-of-care solution, the development of wearable monitoring devices is critical. Designing a hands-free, ergonomic system requires addressing complex hardware and acoustic challenges. Crucially, selecting and validating the optimal operating frequency is an essential step to achieve the spatial resolution necessary for tracking superficial muscle dynamics while ensuring a compact device footprint [5].

1.2 Aims and Objectives of the Project

The primary goal of this research project is to lay the technological and methodological foundations for the development of a wearable ultrasound monitoring device dedicated to SLT. Specifically, this work aims to experimentally validate and

establish the superiority of a high-frequency (HF) 14 MHz array over alternative configurations for submental muscle tracking. Although the definitive system requirements emerged progressively through the initial investigative phases, this thesis focuses on proving that the spatial resolution and penetration depth of the 14 MHz array are critical to accurately monitor the superficial anatomical structures involved in swallowing and speech.

To clear the path to make this wearable technology a reality, this project investigates the hardware, acoustic and anatomical constraints, exploring the practical limitations around hardware, sound, and human anatomy. It has three main objectives:

1. **Development and Validation of an Oesophageal Phantom Framework:** To build and test a custom-made anatomical phantom that replicates the cervical oesophagus. This objective focuses on creating a narrowing within the internal lumen to simulate oesophageal stenosis, a condition that severely restricts food passage and directly leads to dysphagia. This setup establishes a targeted benchtop tool to evaluate the ultrasound system's capability to detect structural changes and execute preliminary dynamic imaging of bolus transit, laying the technical groundwork for optimising future testing protocols.

2. **Hardware Integration and Custom fPCB Design:** To complete the physical hardware integration of the selected 14 MHz HF array by developing a dedicated flexible printed circuit board (fPCB) interfacing platform. This objective focuses on implementing specific HF design constraints, such as controlled 50 Ω impedance matching for the signal traces, to minimise signal attenuation and reflections during data acquisition.

3. **Anatomical Proof-of-Concept and Performance Mapping:** To evaluate the performance of the 14 MHz array through preliminary anatomical imaging sessions. The aim is to confirm, not only qualitatively but also quantitatively, its superior feasibility for tracking superficial submental muscles, compared with higher frequencies arrays, while establishing a baseline for the future implementation of advanced signal optimisation techniques.

1.3 Thesis Outline

The outline of this thesis is structured as follows to present the hardware interfacing, experimental methodology, and validation framework developed:

- **Chapter 2 - Technical Background:** This chapter provides the clinical and technical background necessary to contextualise the project. It reviews the anatomy of the neck, the physiology of swallowing, the clinical impact

of dysphagia, and the role of SLT. On the technological side, it explores ultrasound imaging principles, tissue-mimicking materials (TMMs) for phantom fabrication, and cadaveric imaging studies. The final part introduces methods dedicated to signal optimisation; specifically, beamforming and coded excitation (CE) are evaluated for their capacity to maximise signal-to-noise ratio (SNR) in HF transducers.

- **Chapter 3 - Design and Integration of the 14 MHz Flexible Interface:** The core hardware architecture engineered for the current prototype is analysed within this section. Specifically, it covers the layout, routing and assembly of a custom fPCB, which serves as the physical interface linking a 14 MHz linear array transducer to the Verasonics Vantage 128 research ultrasound platform (Verasonics Inc., Kirkland, WA, USA). It also covers the design rationale and the selection process, including the technical evaluation that led to discarding two alternative array configurations during early stages.

- **Chapter 4 - Experimental Validation: From Tissue-Mimicking Phantoms to Cadaveric Specimens:** The experimental framework established to validate the system is presented here. The testing methodology follows a step-by-step approach, moving from initial acoustic characterisation on a homogeneous TMM phantom to a custom-fabricated oesophageal one simulating a stenotic tract that causes dysphagia. Finally, the practical deployment of these steps is validated through experimental imaging data collected on fresh-frozen cadavers in the Anatomy Department of the University of Glasgow.

- **Chapter 5 - Comparative Analysis:** Based on experimental data, this section provides a critical performance analysis regarding both acoustic and system parameters. It outlines the specific technical constraints and deployment challenges linked to alternative methodologies designed for continuous dysphagia monitoring. Furthermore, a quantitative performance comparison is presented between the HF commercial Verasonics probe and the custom 14 MHz prototype in terms of SNR, contrast-to-noise ratio (CNR), and maximum penetration depth (MPD), thereby justifying the selection of the 14 MHz rigid prototype as the optimal trade-off.

- **Chapter 6 - Conclusions and Future Developments:** The thesis concludes with a summary of the main results and the basic work done for future wearable ultrasound systems. It then outlines future research areas, including a first ergonomic and anatomical study. This part examines specifically the best way to place the device on the body to ensure proper acoustic coupling during hands-free use.

Chapter 2

Technical Background

This chapter formulates the theoretical and technical framework required to assess non-invasive, wearable ultrasonic systems inside SLT environments. It leads with a brief review of how sound waves behave, how ultrasound imaging works, and how transducers convert electrical signals into sound. It then details the anatomy of the neck, specifically the physiology of swallowing and the key structures involved. Next, it outlines the scope of SLT in clinical practice, including the growing shift towards point-of-care and wearable monitoring tools. The chapter closes in exploring the validation models used during the experimental phase, including tissue-mimicking phantoms and cadaveric specimens, along with signal processing techniques like CE and beamforming; it also provides a brief overview of relevant image quality metrics.

2.1 Ultrasound Imaging

Medical ultrasound has evolved into a very widely used, non-invasive, and non-ionizing diagnostic tool that allows the real-time visualisation of internal organs and soft tissues. It is based on the propagation of sound waves, which are reflected by various biological structures and converted into electrical signals for subsequent digital image reconstruction. Due to minimal infrastructure requirements and low equipment costs, the demand for ultrasound services has grown steadily; however, providing reliable diagnostic outcomes remains heavily dependent on highly trained and skilled operators [3].

In clinical research and rehabilitation, defined by the World Health Organization as a set of interventions aimed at optimising functioning, reducing disability, and restoring independence in everyday activities [4], ultrasound provides a safe and dynamic method to monitor physiological processes. To effectively apply this technology to real-time monitoring, it is helpful to examine the physical principles

governing wave behaviour, acoustic impedance, and the technical parameters that influence image quality.

2.1.1 Theoretical Principles

The generation of medical ultrasound images is governed by the physical interaction between acoustic waves and biological tissues [6]. This process relies on the fundamental laws of wave propagation, reflection, and attenuation. To understand how ultrasound can be utilized to monitor the submental region and the swallowing process, it is necessary to define the nature of these mechanical waves and the parameters that influence their behaviour within the human body. This section addresses the foundational physics of ultrasound by focusing on three interconnected aspects:

- The principles of the pulse-echo approach;
- The role of acoustic impedance within medium transitions;
- The direct connection between operating frequency and final image quality.

2.1.2 Nature of Ultrasound and Wave Propagation

How does ultrasound propagate? As mechanical longitudinal waves (Figure 2.1), whose acoustic vibrations exceed the human hearing threshold, typically operating above 20 kHz [7]. Unlike electromagnetic radiation, energy transmission depends entirely on the local oscillation of particles; thus, a physical medium is strictly required: sound cannot travel through a vacuum.

The velocity of the waves depends on the density and elasticity of the medium; in medical ultrasonography, which utilises a broad frequency range (typically from 1 MHz up to 30 MHz for high-resolution applications), the propagation speed in soft tissues is conventionally token to be at $1540\,\mathrm{m\,s^{-1}}$ [6]. However, this value represents a generalised acoustic average for human soft tissue. In reality, the human body is a highly heterogeneous medium, and individual biological tissues exhibit distinct acoustic speeds depending on their specific macromolecular and structural composition (see Table 2.1). For instance, ultrasound travels significantly slower in fatty layers, whereas highly dense structural tissues, such as bone, exhibit substantially higher propagation speeds.

This value is a fundamental parameter used by ultrasound systems to calculate the depth of internal structures by measuring the time delay of reflected echoes, assuming a linear path and constant velocity within the body. This velocity (v) is linked to the operating frequency (f) and the wavelength (λ) by the relation [3]:

$$v = f\lambda \tag{2.1}$$

Table 2.1: Speed of sound in various human tissues and media (data from [8, 9]).

Tissue/Medium	**Speed of Sound ($\mathbf{m\,s^{-1}}$)**
Air	333
Fat	1430
Water	1480
Soft Tissue (Avg)	1540
Liver	1578
Muscle	1647
Bone	3190 – 3406

In ultrasound imaging, the wavelength is a critical parameter as it directly limits the axial resolution: shorter wavelengths (associated with higher frequencies, such as the 28 MHz used in this study) allow for the visualisation of smaller anatomical details. The signal intensity depends directly on the acoustic pressure, which is represented by the wave amplitude; as propagation occurs, this intensity naturally drops because of attenuation mechanisms.

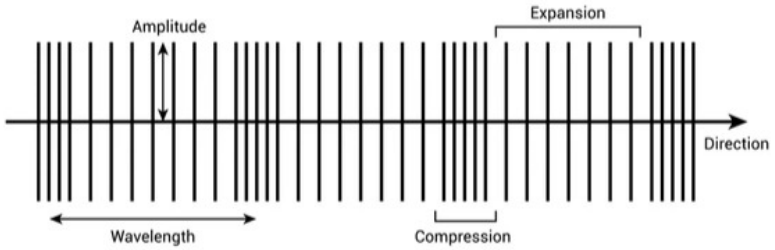

Figure 2.1: Schematic representation of longitudinal wave propagation. The diagram highlights the areas of compression and expansion (rarefaction), and the fundamental parameters: wavelength (λ) and amplitude (adapted from [10]).

2.1.3 Acoustic Impedance and Reflection: Interaction with Tissues

As ultrasound waves pass through anatomical structures, interactions naturally and continuously occur at the various tissue boundaries and interfaces. These interactions are fundamentally governed by the differences in the physical and mechanical properties of adjacent media. Recognising that different tissues possess distinct sound speeds is essential: it is precisely this localised variation in speed,

combined with changes in tissue density, that creates mismatches in acoustic impedance (Z) at anatomical borders.

The most critical interaction for image formation is reflection, which is central to the pulse-echo technique. The transition between layers with distinct acoustic impedances causes a fraction of the ultrasound energy to reflect back as an echo [7]. The strength of this reflected signal is directly proportional to the magnitude of the impedance mismatch; this returned echo is subsequently detected by the transducer and used to reconstruct the structural interface of the internal anatomy.

Acoustic impedance (Z) represents the resistance of a tissue to the passage of ultrasound and is defined as the product of the tissue density (ρ) and the propagation speed (v) [3]:

$$Z = \rho v \tag{2.2}$$

Acoustic impedance is measured in units called Rayls, where $1\ \text{Rayl} = 1\,\text{kg}\,\text{m}^{-2}\,\text{s}^{-1}$. As body tissues have very high impedance values, these are conventionally expressed in MegaRayl, where $1\,\text{MRayl} = 10^6$ Rayl.

How stiff a tissue is plays a key role here, as stiffness is the primary mechanical characteristic that dictates speed of propagation throughout the medium, determining how fast sound travels through it. This relationship means that any dynamic changes in acoustic impedance are directly driven by changes in both the density or the stiffness of the tissue.

While the speed remains relatively constant across most soft tissues (assumed to be $1540\,\text{m}\,\text{s}^{-1}$), a greater impedance mismatch at an anatomical interface results in a stronger reflection. For example, the soft tissue/bone and soft tissue/air interfaces produce high-intensity echoes due to their extreme differences in stiffness and density, appearing as bright (hyperechoic) landmarks [7]. Table 2.2 summarizes Z values for several human tissues and media.

Table 2.2: Acoustic impedance values for various human tissues and media (data from [8]).

Tissue / Medium	**Acoustic Impedance (MRayl)**
Air	0.00043
Fat	1.33
Water	1.48
Liver	1.66
Bone	6.47

Energy Dissipation: Attenuation and Loss As the ultrasound beam traverses tissue structures, it progressively loses energy through a phenomenon known as attenuation. This weakening is the result of absorption (conversion of energy into heat), scattering, and refraction [7].

A fundamental principle in ultrasound physics is that the attenuation coefficient increases approximately linearly with frequency in soft tissues. Consequently, as the wave propagates deeper into the body, its intensity undergoes an exponential decay [8]. While HF transducers provide superior resolution for superficial layers, they suffer from much higher energy loss due to this exponential decay, limiting the effective imaging depth. For effective neck monitoring, frequency selection, including the 14 MHz configuration in this study, determines whether deeper targets like the oesophageal wall stay detectable despite their depth and attenuation in superficial layers [5].

2.1.4 The Resolution–Penetration Compromise

Developing an ultrasound system requires a design decision regarding transducer frequency [5]. This forces a direct balance between wave penetration and image resolution. For general submental neck imaging, utilising a 14 MHz frequency provides the necessary depth to reach deeper anatomical layers. Shifting to a higher, 28 MHz, setup maximises both axial and lateral resolution; this allows the system to capture fine anatomical details and subtle tissue effects at the expense of penetration. This resolution gain, however, directly increases signal attenuation. Navigating this strict balance remains central to both the experimental protocols and the wearable device optimizations detailed later.

2.1.5 Ultrasound Transducers and the Piezoelectric Effect

The transducer, or probe, is a fundamental component in an ultrasound system, acting as both the source of acoustic energy and the detector of reflected signals. Its operation is based on the piezoelectric effect, a physical phenomenon where certain crystalline materials generate an electric potential in response to mechanical deformation or stress [7].

In the imaging process, these crystals function in two distinct modes, as shown in Figure 2.2:

- **Transmission:** An alternating signal is applied to the piezoelectric crystals, causing them to vibrate at a high frequency and generate a longitudinal ultrasound beam directed into the tissues.
- **Reception:** After a short transmission pulse, the crystals act as receivers. When reflected echoes return from the tissue, the resulting pressure causes

the crystals to vibrate, converting the mechanical energy back into electrical signals for computerised processing.

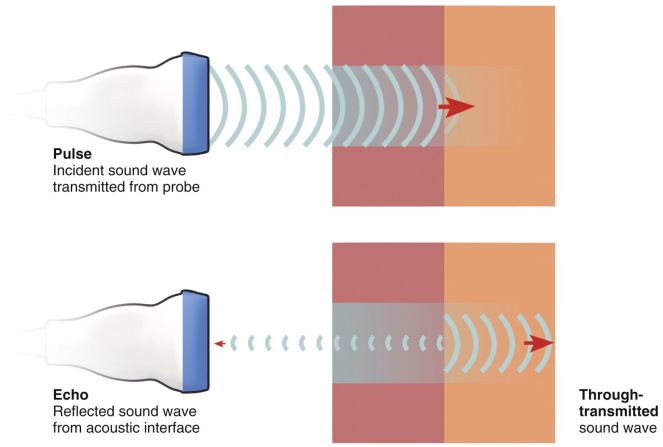

Figure 2.2: Schematic representation of the pulse-echo principle, illustrating the interaction between the incident beam and acoustic interfaces (adapted from [6]).

The transducer can be moved by the operator to change the angle of incidence, allowing the visualisation of different anatomical planes [6]. Furthermore, since ultrasound cannot propagate through air pockets between the probe and the skin, a conducting gel is mandatory to ensure acoustic coupling and efficient wave transmission into the body [3].

For the experimental sessions in this study, various frequencies were employed to balance resolution and penetration; however, flat linear array transducers were used exclusively. Unlike curved or phased arrays, a linear transducer activates a group of piezoelectric elements in a precise sequence to produce parallel scan lines, as shown in Figure 2.3. This ensures a rectangular field of view and a constant scan line density across the entire width of the image.

Because target structures in neck anatomy are highly superficial, this choice remains the baseline standard. To image the thin, horizontal muscle layers and airway interfaces characteristic of the submental region, flat linear arrays offer the ideal flat footprint combined with parallel scan lines.

2.1.6 B-mode Image Formation

The signals received by the piezoelectric crystals are amplified and processed to be displayed as pixels of varying brightness on a grayscale monitor. In Brightness mode (B-mode), each echo is represented by a pixel whose intensity (shade of gray) corresponds to the echo's amplitude [6]. The spatial position of each pixel on the

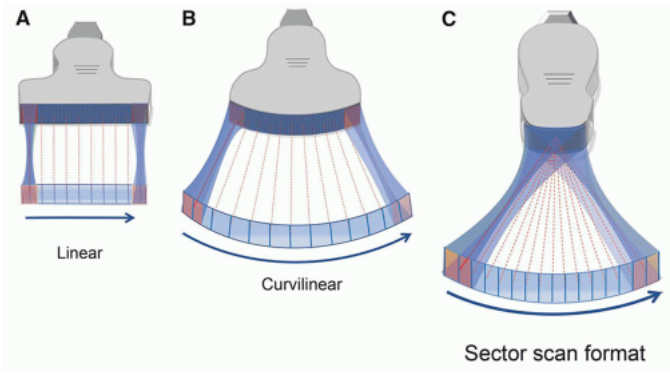

Figure 2.3: Comparison of scan formats: (A) linear, (B) curved, and (C) sector/phased array. The linear format (A) is preferred for neck imaging as it provides a uniform rectangular field of view (adapted from [11]).

screen represents the depth of the reflector, calculated through the time-of-flight of the pulse. By scanning multiple scan lines across the tissue, the B-mode assembles a 2-dimensional anatomical map, as illustrated in Figure 2.4. While other modes like A-mode (Amplitude) and M-mode (Motion) may be used for specific diagnostic purposes, B-mode remains the standard for structural anatomical imaging.

The relationship between the raw ultrasonic signals and the final image formation is fundamental. These raw signals captured by the transducer are HF analog waveforms, conventionally referred to as RF signals. As illustrated in Figure 2.4, the B-mode image is essentially a 2-dimensional assembly of multiple A-mode signals. Each pulse returned from the tissue scatterers is initially processed as an A-mode (Amplitude mode) signal, where the intensity of the reflection is represented by spikes along a baseline. These amplitudes are then converted into pixels of varying brightness to form individual scan lines; by integrating these lines across the transducer's field of view, the system reconstructs the final anatomical B-mode map [12].

2.1.7 Signal Processing and Display

Once the returning echoes reach the transducer, the generated piezoelectric signals are electronically processed before being displayed. This signal processing chain consists of four fundamental stages [3]:

1. **Amplification:** Because the intensity of the returning echoes is only a tiny fraction of the original transmitted pulse, the resulting voltage generated at the transducer is extremely small and must be amplified to become processable.

2. **Time Gain Compensation:** Acoustic attenuation can be compensated for

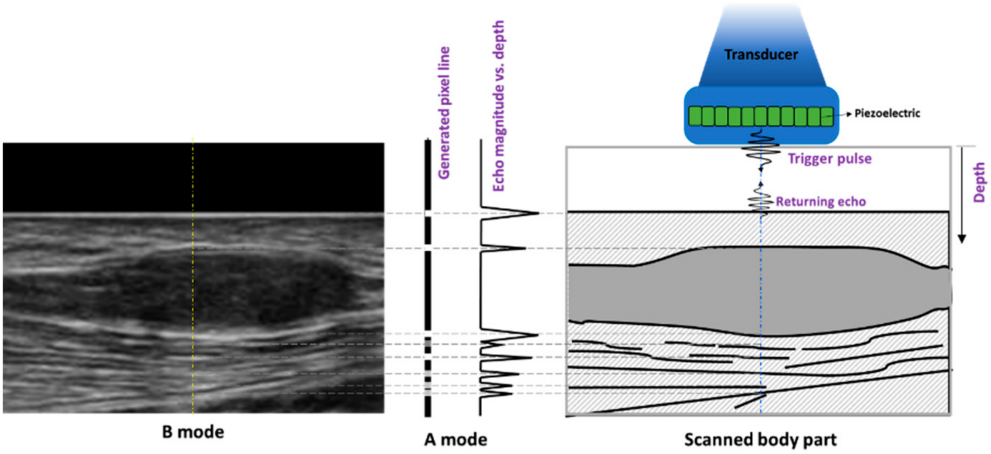

Figure 2.4: Reconstruction of a B-mode image from raw ultrasonic data. The process illustrates how individual A-mode signals (right) are converted into grayscale scan lines (middle) and then integrated to form the complete 2D B-mode anatomical map (left) (adapted from [12]).

through time gain compensation (TGC), which, according to depth, applies amplification. Echoes originating from deeper tissue structures travel longer distances and are amplified to a greater extent than superficial ones. This ensures that identical tissue boundaries produce equal-sized signals, regardless of their depth.

3. **Compression:** The dynamic range of incoming signal is often too large for standard display screens. To reduce this range, logarithmic compression is applied, which maps the incoming signals into a scale suitable for visual representation.

4. **Filtering:** Extremely weak signals that fall below a set threshold are removed electronically. This process reduces noise and eliminates low-amplitude signals with an increased probability of being associated with artifacts, rather than real tissue.

2.2 Anatomy of the Neck and Dysphagia

Deploying ultrasound imaging as a practical tool for diagnosis and rehabilitation demands a thorough grounding in upper aerodigestive tract anatomy. Indeed, the act of swallowing represents an intricate, highly coordinated physiological event, relying entirely on synchronous interactions between specific muscle groups and cartilaginous structures. For patients facing HNC, such mechanisms face severe

disruption either directly from the malignancy or following aggressive clinical interventions, such as radiotherapy-induced tissue fibrosis and surgical resections. Understanding these factors requires a closer look at healthy swallowing physiology, the onset of oncology-related dysphagia, and how specific anatomical landmarks present under submental ultrasound imaging. A detailed representation of the cervical anatomy, highlighting the relationship between the oral cavity, the pharynx, and the airway, is shown in Figure 2.5.

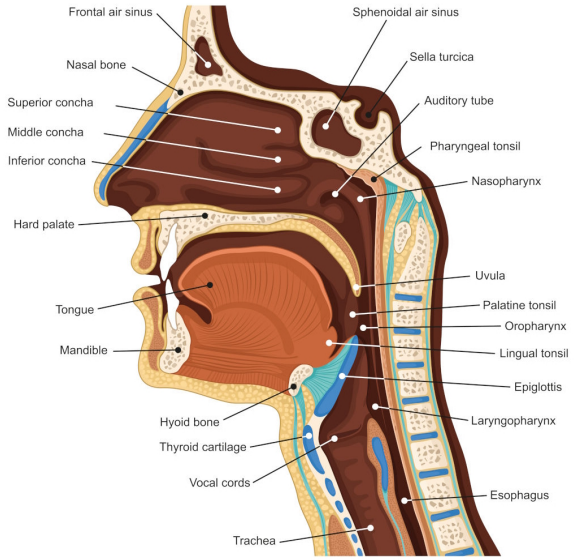

Figure 2.5: Midsagittal section of the head and neck anatomy, showing the primary structures, including the oral cavity, pharynx, larynx, and cervical oesophagus (adapted from [13]).

2.2.1 Physiology of Swallowing

Swallowing is a rapid and highly coordinated pressure-driven event that involves the synchronised action of over 29 muscles and various oropharyngeal structures [14]. Although this entire sequence spans less than a second, clinical tradition categorises it into distinct stages based on the corresponding anatomical cavities:

- The oral phase (which includes both bolus preparation and transport);
- The pharyngeal phase;
- The oesophageal phase.

The swallowing process begins with an anticipatory phase: before food even enters the mouth, the sight and smell of food prime the system for bolus entry. During the next stage, the oral preparatory phase, mastication and salivary mixing form a soft, cohesive bolus. The tongue then drives the phase known as oral transport, serving as the primary manipulator and sealing against the hard palate to propel the bolus backward into the pharynx.

The pharyngeal phase constitutes a critical transition, where the cavity acts as a pathway from the oral cavity to the oesophagus. The mechanism must prevent the bolus from entering either the nasal cavity or airway in order to guarantee safe passage. It achieves this in several ways:

- **Laryngeal Elevation:** The hyoid bone and larynx move upward and forward (hyolaryngeal excursion) to help close off the airway.
- **Epiglottic Inversion:** The epiglottis folds down over the entrance to the laryngeal inlet, acting as a "shield" that redirects the bolus around the airway towards the oesophagus instead.
- **Vocal Fold Closure:** The vocal folds adduct to provide a final internal seal of the airway.

Once the bolus passes through the upper oesophageal sphincter (UES), the oesophageal phase begins, propelling the nutrients toward the stomach via peristaltic waves.

The biomechanical coordination required for bolus transit is illustrated in Figure 2.6. As modelled by the Artisynth OPAL project [15], the transition from the oral to the pharyngeal phase involves a precise sequence of tongue elevation, hyoid bone excursion, and epiglottic inversion to protect the laryngeal inlet.

2.2.2 Head and Neck Cancer and Related Dysphagia

HNC includes various malignancies affecting the mouth, throat, and larynx. While the exact causes are not always clear, several risk factors significantly increase the probability of development. According to Macmillan Cancer Support, approximately 75 % of HNC cases are linked to tobacco and alcohol consumption. Furthermore, there has been a recent increase in oropharyngeal cancers (specifically of the tonsils and base of the tongue) associated with the human papillomavirus (HPV) [16].

Regardless of the specific etiology, the clinical focus for rehabilitation lies in the severe functional consequences of the disease and its treatments. Dysphagia is a highly prevalent and disabling complication in this population. As discussed by Schellen et al. [1], swallowing dysfunction arises from a combination of chemo-radiotherapy (CRT) and surgical interventions, which contribute to the following mechanisms:

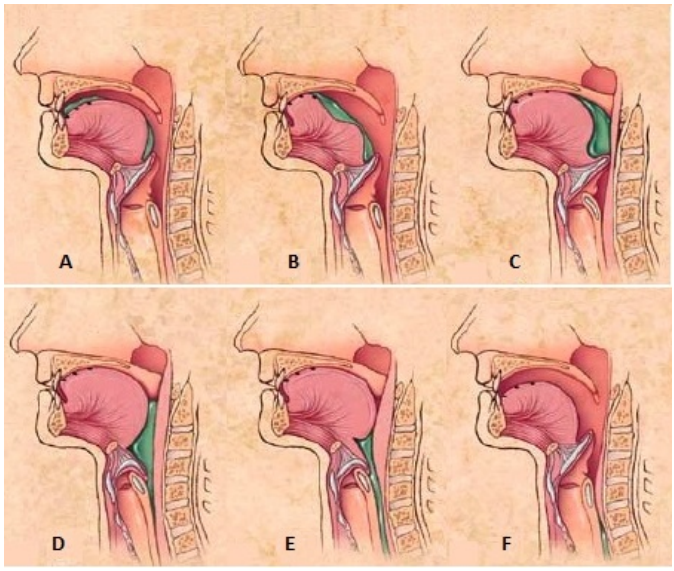

Figure 2.6: Biomechanical simulation of the swallowing process stages. The sequence illustrates the bolus transit from the oral phase (A-B) through the pharyngeal phase (C-D-E) and into the oesophageal phase (F), highlighting the coordination of the tongue, hyoid bone, and laryngeal structures (adapted from [15]).

- **Fibrosis and Edema:** Radiation-induced fibrosis causes a progressive stiffening of the tissues, which restricts the movement of the muscles involved in the swallow.
- **Muscle Atrophy and Disuse:** Often linked to surgical trauma or CRT side effects, this lack of use leads directly to a drop in both strength and functional performance.
- **Neuropathic Effects:** Damage to the lower cranial nerves degrades the coordination and sensory feedback needed to ensure a safe swallow.
- **Anatomical Alterations:** Surgical resections change the actual landscape of the neck, directly impacting the biomechanics of bolus transit.

As highlighted in current research, understanding these specific changes in biomechanics is essential for developing effective rehabilitation strategies. While strength-based and functional exercises show benefits, there is a clear need for objective studies to examine the effect of different intervention modalities on swallowing outcomes [1].

Pharyngo-oesophageal Strictures in HNC Patients Pharyngo-oesophageal stricture (PES) represents a severe late complication in patients treated for HNC, affecting up to one-third of those undergoing external beam radiotherapy or CRT [17]. As noted in the literature, PES is the clinical endpoint of a progressive process initiated by treatment-related mucosal injury. While some injuries heal with little consequence, others evolve into fibrosis, leading to muscular dysfunction and, eventually, partial or complete luminal narrowing [18].

Understanding this pathological cascade is essential for early clinical recognition, as it typically follows three distinct stages:

- **Acute Phase (Mucositis):** The process begins with mucosal injury or mucositis (Figure 2.7A), which often accounts for the acute dysphagia experienced during treatment. While many cases resolve spontaneously, deeper injuries involving the submucosa or muscular anatomy can trigger a pathological cascade.

- **Chronic Phase (Cicatricial Scarring):** In approximately 50 % of patients, the injury leads to chronic dysphagia associated with cicatricial scarring of the lumen (Figure 2.7B). This stage represents a significant restriction of the passage.

- **Final Stage (Complete Stricture):** In around one in three patients, the narrowing becomes a complete stricture (Figure 2.7C), defined as the total absence of food or liquid passage. At this point, the condition is often irreversible, and the patient may need permanent gastrostomy, a feeding tube inserted directly into the stomach, or complex surgical reconstruction of the passage.

Research suggests that up to 37 % of patients reach the stage of a symptomatic stricture [18]. One of the biggest challenges for clinicians is telling the difference between an early, treatable injury and one that is becoming permanently worse (see Figure 2.7). Early detection and monitoring of structural changes is crucial. It gives speech and language therapists the opportunity to initiate timely interventions, treatments such as swallowing manoeuvres or referring the patient for endoscopic dilation, a procedure to widen the passage.

This is where ultrasonography is key. It provides a non-invasive way to monitor the structural integrity of the pharyngo-oesophageal junction without the need for more invasive procedures. With this in mind, the "stricture model" research phantom used in this study was designed to simulate a luminal narrowing. This created a controlled test environment to assess whether ultrasound can reliably detect and support early clinical action, and can therefore be recommended as a tool for early recognition and clinical intervention.

The experimental setup, the scanning protocols adopted, and the results obtained from the tests performed on this specific model are extensively documented and discussed in Chapter 4.

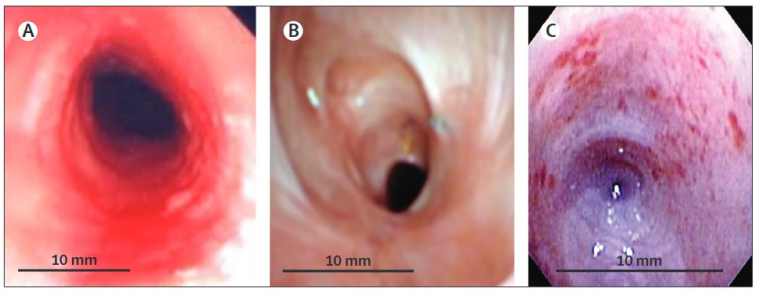

Figure 2.7: Progression of pharyngo-oesophageal injury post-chemoradiotherapy: (A) acute mucositis, (B) cicatricial scarring with partial narrowing, and (C) complete pharyngo-oesophageal stricture (PES) (adapted from [18]).

2.2.3 Ultrasound Landmarks in the Submental Region

As highlighted by recent clinical literature, ultrasonography has emerged as a valuable non-invasive tool for assessing swallowing-related structures that were traditionally difficult to examine without expensive or invasive procedures, such as videofluorography or fibreoptic endoscopic evaluation [19]. The portability of modern ultrasound equipment allows for real-time bedside evaluation of several key muscles and anatomical landmarks.

Swallowing Structures In the submental region, the following structures are essential for SLT assessment of swallowing function, shown in Figure 2.8. The specific clinical role and interventions of SLT in this context are detailed in Section 2.3.

- **Suprahyoid Muscle Group (Geniohyoid, Mylohyoid, and Digastric):** These are the principle muscles responsible for hyolaryngeal excursion. Ultrasound can measure the thickness and cross-sectional area, both of which critical indicators of muscle health, especially in cases of sarcopenic dysphagia or radiation-induced atrophy [19]. While sarcopenic dysphagia is primarily linked to generalised muscle loss, it represents a critical factor in HNC patients. The combination of radiation-induced fibrosis and disuse atrophy can lead to a secondary sarcopenic state of the swallowing musculature, which ultrasound can effectively monitor.
- **The Hyoid Bone and Larynx:** The hyoid bone, a small bone in the throat, shows up clearly on ultrasound as a hyperechoic structure with a distinct

acoustic shadow. Monitoring its displacement is crucial for evaluating the safety of the pharyngeal phase. Ultrasound can also show the cartilages that make up the laryngeal framework (such as the thyroid and cricoid cartilages). These act as useful reference points for measuring how far the voice box moves upward during swallowing, which is a key part of how the body protects the airway from food and liquid entering the lungs during the airway protection phase.

- **Tongue and Genioglossus:** Ultrasound gives a detailed view of tongue pressure and movement against the hard palate, which is essential for gathering food into a manageable lump and moving it towards the throat ready for swallowing. When the probe is placed under the chin, the genioglossus and the intrinsic muscles of the tongue can be clearly seen, allowing clinicians to assess how well they are working together during the the oral preparatory phase.

- **Pharyngeal and Oesophageal Structures:** Advanced protocols include the visualisation of the pharynx and the cervical oesophagus to detect signs of dysfunction. In the submental and anterior neck window, the oesophagus is identified just posterior to the trachea, descending from the level of the sixth cervical vertebra [20], allowing for the assessment of bolus transit and potential UES clearance issues.

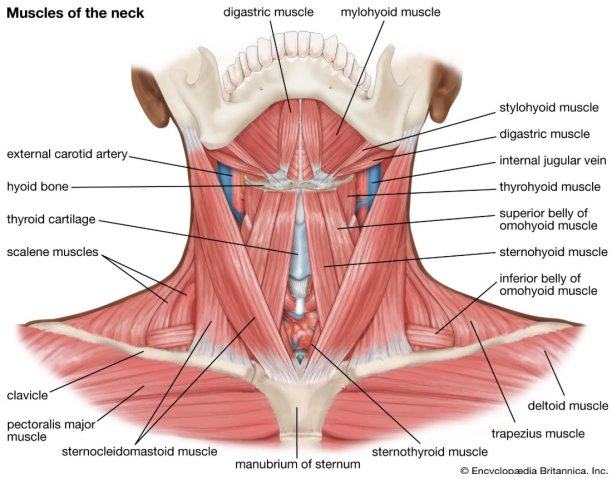

Figure 2.8: Anatomical representation of the submental muscular complex. These muscles play a crucial role in swallowing and serve as the structural basis for measuring muscle thickness and displacement via ultrasound (adapted from [21]).

Scanning Planes and Probe Positioning To visualise these landmarks, the probe is typically placed in the submental region using two primary scanning planes [6]:

- **Transverse (Coronal) Plane:** The probe is placed horizontally under the chin. This view is best for seeing the stratification of the mouth, allowing for viewing of the different layers. Working from the skin inward, one can make out three distinct muscles: the anterior belly of the digastric, the thin band of the mylohyoid, and the thicker geniohyoid running through the centre.
- **Longitudinal (Mid-sagittal) Plane:** The probe is rotated 90° along the midline of the body. This orientation is essential for tracking how the hyoid bone moves upward and forward during swallowing, as well as observing the overall movement of the tongue.

The standard sonographic positioning for capturing these landmarks, specifically through a transverse submental view, is illustrated in Figure 2.9.

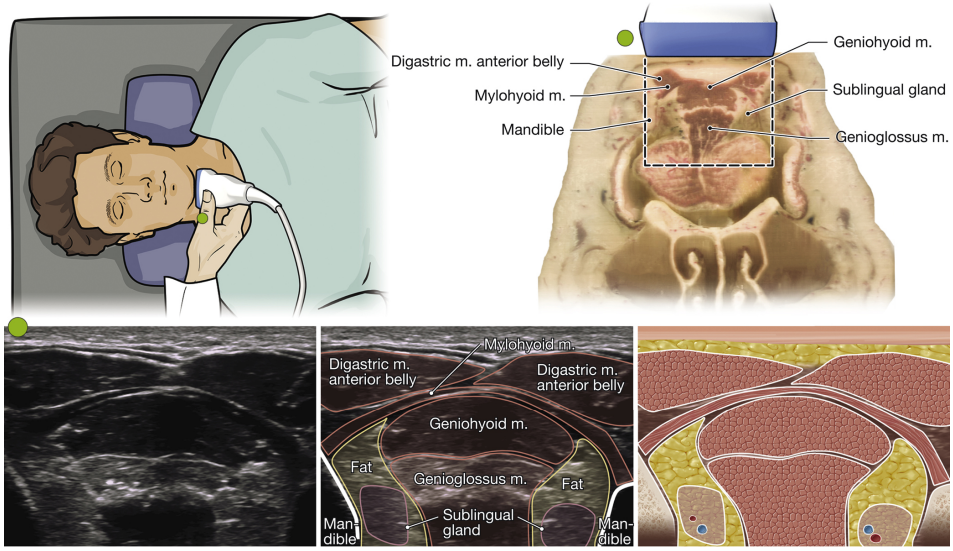

Figure 2.9: Transverse submental ultrasound view mapping the primary suprahyoid musculature and anatomical landmarks for swallowing assessment (adapted from[6]).

Detection of Dysphagia Beyond anatomical measurements, ultrasonography is capable of identifying direct clinical signs of dysfunction. A significant example is the detection of food residue within the oropharyngeal cavities or the pharyngeal recesses, as shown in Figure 2.10. In patients with impaired muscular strength or

coordination, ultrasound can visualise hyperechoic material remaining after the swallow, providing immediate feedback on the efficiency of bolus clearance [19].

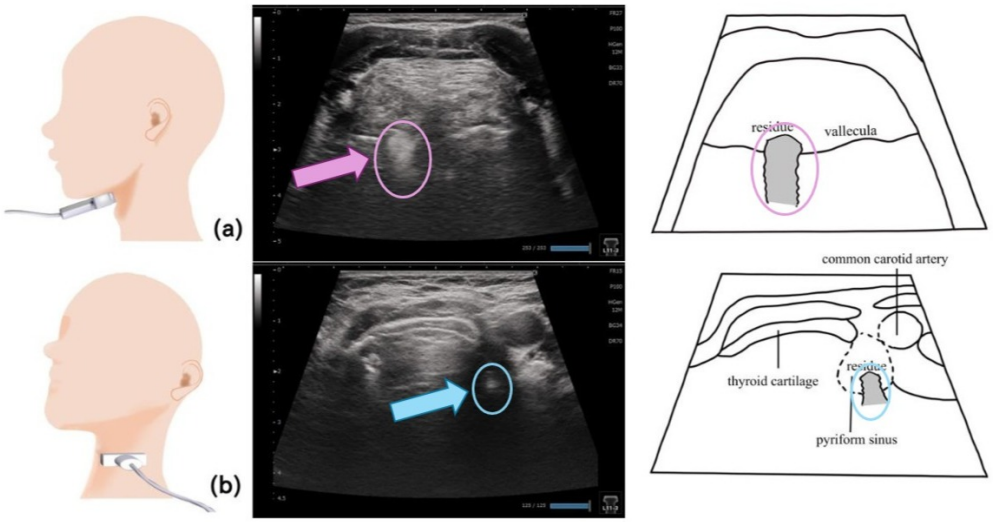

Figure 2.10: Ultrasound detection of food residue in different anatomical site: (A) transverse scan showing hyperechoic food residue accumulated within the epiglottic vallecula; (B) visualisation of food residue remaining in the pyriform sinus (adapted from [19]).

2.3 Speech and Language Therapy

SLT is a multi-faceted clinical profession dedicated to the assessment, diagnosis, and treatment of a wide range of communication and swallowing disorders. According to the Royal College of Speech and Language Therapists [2], the role of the therapist is essential in managing complex clinical conditions to improve a patient's quality of life through both direct rehabilitation and instrumental assessment.

While speech and language therapists have traditionally focused on speech production, language processing and voice quality, the field has increasingly embraced technology over recent decades to better understand the complex biomechanics of deglutition. Ultrasound imaging has become a particularly valuable tool in this area, as it allows therapists to see internal structures moving in real time without any radiation or invasive procedures, making it useful for both diagnostic precision and guiding feedback. This technological integration is particularly important in managing complex cases, such as those involving head and neck oncology, where visualising structural movement is key to successful rehabilitation.

2.3.1 Clinical Context and Rehabilitation

The rehabilitation of complex clinical conditions requires a multidisciplinary team (MDT), where the SLT plays a pivotal role in restoring functional autonomy and reducing the impact of treatment-related consequences. In patients diagnosed with HNC, impairments often result from a combination of the pathology itself and advanced oncological interventions, including intensity-modulated radiotherapy, immunotherapy, and transoral or reconstructive surgery [22].

Parallel to the evolution of these treatment modalities, patient survival has seen a major increase. Over recent decades, advancements in intensity-modulated radiation therapy, systemic therapy standardisation, and diagnostic imaging, such as magnetic resonance imaging (MRI) and positron emission tomography (PET)-computed tomography (CT), have increased the 5-year overall survival rate for HNC patients from roughly 52.7 % to more than 65.9 % [23]. As a result, a growing cohort of cancer survivors brings new demands for the SLT regarding the long-term management of late treatment toxicities and pathologies.

In response to these shifting clinical needs, specific survivorship care guidelines have been established by major international oncological bodies, including the American Cancer Society [24] and specialty networks across the UK and Australia [23]. UK clinical guidelines, for instance, highlight that evaluating speech and swallow rehabilitation requirements must occur before initiating any oncological protocol, with structured interventions extending across the entire patient pathway and into long-term follow-ups [25].

To keep assessments accurate and maintain objective clarity across different clinical disciplines, tools like videofluoroscopy are essential to pinpoint silent deficits and break down swallow mechanics that may not be obvious and for analysing how swallowing works in detail. Ultimately, good clinical care hinges on carrying out a thorough initial assessment through multidimensional baseline evaluation. This is vital, not only to catch acute deficits early, but also to guide patient education, allowing them to know what changes to expect, and for putting prophylactic, compensatory, and rehabilitative strategies in place from day one to achieve optimal long-term functional recovery. Mapping both the efficiency and safety of the swallow remains a core priority to prevent risks of nutritional deficits, respiratory compromise, and silent aspiration [22].

Furthermore, severe late complications, such as dysphagia caused by pharyngeal stenosis after chemoradiotherapy, are difficult to correct; managing these complex, refractory cases requires highly specialised, expert clinical teams [25]. Because patients may experience reduced sensitivity or progressive fibrosis (as discussed in Section 2.2), the SLT requires objective, high-quality tools to monitor progress beyond subjective bedside observation. This necessity drives the transition from traditional therapy to instrumental-aided rehabilitation, providing a clear rationale

for the integration of ultrasound imaging into the clinical setting to visualise and quantify structural movement in real-time.

2.3.2 Ultrasound Biofeedback

As the application of ultrasound imaging expands beyond traditional radiology settings, its role within the SLT profession has evolved from a purely diagnostic tool to an interactive rehabilitative modality. In the past, high costs and restricted access blocked the widespread adoption of this technology. However, a steep drop in these barriers has recently driven a surge of interest in deploying ultrasound visual biofeedback (U-VBF) as an active therapeutic intervention [26].

Even though a growing number of studies validate the clinical utility of U-VBF, especially when addressing speech sound disorders (SSD), recent international consensus data indicate that establishing its full translation into routine, everyday practice remains an ongoing effort [27]. Using formal methodologies, speech and language pathologists have highlighted that alongside its use for biofeedback, there remains a critical research priority to establish standardised data reliability, validity, and baseline normative values for swallowing and laryngeal assessments.

In clinical implementation, U-VBF protocols typically integrate specific motor learning frameworks, dividing the intervention into pre-practice and practice phases to guide the patient through explicit visual-motor monitoring, as demonstrated in open-access clinical training repositories [28]. During these sessions, the ultrasound transducer is positioned submentally to capture the dynamic, real-time contour of the tongue surface. By converting an otherwise hidden internal movement into an immediate target on a monitor, the patient can observe their tongue placement and shape, adjusting the kinematics instantaneously to match the correct articulatory targets.

2.3.3 Transition to Point-of-Care and Wearable Ultrasound

The integration of ultrasound into SLT practice is currently moving toward a more flexible and immediate application, often described as point-of-care ultrasound (POCUS). This transition aims to bring instrumental assessment directly to the patient's bedside, allowing for real-time evaluation during natural feeding sessions, in various clinical settings, including challenging ones such as emergency departments, intensive care units, and remote rural areas [29].

Originally conceptualised in the late 20th century and often referred to as the "visual stethoscope" of modern medicine, POCUS has fundamentally redefined diagnostic timelines by shifting from comprehensive, hours-long consultative imaging to goal-directed, real-time evaluations completed in minutes [30]. Handheld devices linked to smartphones or tablets have significantly broadened the scope of bedside

imaging, a shift directly facilitated by rapid hardware miniaturisation, falling costs, and enhanced signal processing power [29]. Moving from highly regulated clinical rooms to unpredictable bedside environments, however, brings up difficult technical hurdles, especially concerning how to keep the scanning window stable.

- **Experimental Stabilization Systems:** In an effort to cut down on the tracking errors linked to manual transducer handling, recent prototype rigs, including adjustable headsets or dedicated collars, have emerged [31]. These systems aim to anchor the probe in a steady submental alignment, helping to secure consistent, repeatable measurements across extended biofeedback protocols and active swallowing tasks.
- **Emerging Wearable Technologies:** Looking further into the future, the development of flexible and wearable ultrasound sensors represents a significant area of interest. Driven by the recent miniaturisation of hardware and the large increase in computational signal capacity [30], these "ultrasound patches" could potentially allow for continuous, non-invasive monitoring of swallowing frequency and muscular effort throughout the day. This approach provides a wealth of dynamic data that traditional, point-in-time assessments cannot capture, establishing a new paradigm for long-term patient monitoring.

Though much of this technology is still confined to experimental setups or early prototypes, it signals a definitive shift toward making rehabilitation ultrasound both automated and miniature. This technological shift highlights why rigorous validation protocols are becoming so urgent. Deploying standardised phantoms, such as the primary prototype evaluated in this work, elaborated in Chapter 4, is important to ensure that portability and wearability do not come at the expense of data accuracy or clinical reliability.

USES Procedure and Instrumentation A dynamic clinical procedure developed for this purpose is ultrasound evaluation of swallowing (USES), an initiative originated by the Division of Speech and Hearing Sciences at Queen Margaret University (Edinburgh, UK) and hosted on the Swallow Vision platform [31].

It allows the oral and pharyngeal functions involved in swallowing to be observed directly and in real time. Carried out primarily by speech and language therapists, the USES protocol tracks the coordinated movement of the mandible, tongue, and hyoid bone along the midline to evaluate critical clinical parameters such as bolus preparation and propulsion and the time for oral transmission. Crucially, the displacement of the hyoid bone in relation to the mandible is used within this framework as a proxy for the pharyngeal stage of swallowing [31].

From an instrumental perspective, USES relies on a highly portable, pocket-sized diagnostic ultrasound system operating in B-mode, typically equipped with

a 2-5 MHz 60 mm convex transducer that achieves high temporal resolution with frame rates ranging between 80 and 119 frames per second. For dynamic and comprehensive assessments, a convex probe is often preferred. This choice allows for a wider, divergent field of view that can capture the entire range of tongue motion and hyoid displacement during swallowing, which might otherwise extend beyond the lateral boundaries of a linear scan.

To ensure clinical utility and reproducibility, USES utilises specific hardware components designed to stabilise the acoustic window and capture data:

- **Stabilisation Headset:** To bypass the tracking errors of manual scanning, the ultrasound probe is mechanically locked into position via a rigid headset framework, known as the Ultrafit frame [31], as illustrated in Figure 2.11. Even so, this fixed approach brings severe structural limits. The whole setup, combining the headset, a heavy standard probe, and the required rear counterweights, reaches a total weight of roughly 600 g. Carrying this rigid, heavy assembly puts an immediate physical strain on the patient, meaning muscle fatigue and general discomfort, making extended testing sessions quite difficult [31]. On top of that, the bulk limits natural head mobility, which risks distorting the baseline swallowing dynamics.

- **Contoured Gel Pad:** A soft, shaped gel pad is placed directly between the probe and the submental skin to improve contact and maximise acoustic coupling, ensuring a clear ultrasound signal. It adapts well to the contours of the neck and helps block air gaps, but it is a disposable item that needs to be replaced. It also requires careful manual alignment and tends to shift out of place during jaw movement.

- **Micro-Camera Integration:** A small, lightweight camera can optionally be clamped to the headset to record profile footage of the patient's chin and lips. While this can help pinpoint exactly the start of pre-swallow motion, adding the camera increases the overall bulk and layout complexity of the wearable device.

Compared to traditional gold-standard instrumental techniques like videofluoroscopic study of swallowing (VFSS) or fibreoptic endoscopic examination of swallowing (FEES), the USES procedure represents a non-invasive, radiation-free alternative. However, current setups remain deeply tied to bulky, rigid, and heavy head-mounted hardware,limiting their widespread integration into daily clinical workflows. Such severe weight and ergonomic bottlenecks pinpoint a major technological gap. This reality demands a decisive pivot toward lightweight, flexible, and genuinely wearable ultrasound designs. Such architectures must secure stable monitoring tracks while prioritising patient comfort as a core requirement.

Figure 2.11: The Ultrafit probe stabilisation headset developed by Articulate Instruments in collaboration with Queen Margaret University for ultrasound swallowing and tongue imaging (adapted from [31]).

2.4 Validation Models for Ultrasound Imaging

The validation of advanced ultrasound imaging techniques and signal processing methods requires stable, controlled experimental platforms before clinical implementation. While *in vivo* testing represents the ultimate clinical target, it introduces significant limitations for engineering validation, primarily due to unpredictable physiological movements, such as deglutition or respiration, and severe ethical constraints regarding prolonged acoustic exposure and patient comfort [32]. Building a reliable reference framework requires combining biological *ex vivo* models with synthetic *in vitro* systems. These twin strategies serve complementary purposes during validation. Synthetic, tissue-mimicking phantoms provide a stable, fixed structure for testing, as they have a stationery, pre-defined geometry. Because their acoustic parameters can be precisely controlled, they give a reliable baseline for checking how accurately the ultrasound captures geometry. Cadaveric specimens, on the other hand, offer real anatomical complexity and acoustic attenuation profiles that artificial materials cannot fully replicate. By combining the geometric reproducibility and consistency of phantoms with the realism of biological tissues, these two approaches together create a thorough testing framework for evaluating how well the transducer performs and how effectively the signal penetrates through tissue.

2.4.1 Tissue-Mimicking Material Phantoms

To validate ultrasound imaging techniques and ensure the reliability of clinical measurements, the use of tissue-mimicking phantoms is essential. Unlike biological tissues, phantoms provide a stable, controlled geometry with known dimensions, representing a "ground truth" that is unaffected by dynamic physiological movements like respiration or swallowing. A primary consideration in phantom design is the choice of the base matrix for water-based TMMs, which typically lies between agar, gelatine, and polyvinyl alcohol (PVA) [33]. This material must accurately replicate the acoustic properties of human soft tissue, such as a speed of sound of approximately $1540\,\mathrm{m\,s^{-1}}$ and a specific attenuation coefficient.

In literature, PVA cryogels are widely cited for their versatility; by altering the molecular weight and the number of freeze-thaw cycles (FTCs), researchers can precisely tune both the acoustic and mechanical properties of the material, making it ideal for cardiovascular or elastography applications [34]. However, PVA fabrication is a lengthy, complicated, and time-consuming process requiring rigorous temperature-controlled cycling often over several days. Crucially for geometric validation, PVA exhibits structural instability, as its size and volume change dynamically with an increase in the number of FTCs [33]. Such volumetric variations and potential shrinking would heavily compromise the spatial accuracy required to model a fixed stricture in the pharyngo-oesophageal segment.

On the contrary, agar has remained a gold standard for TMM phantom fabrication since 1980, with specific formulations recommended for simulating soft tissues due to their excellent native acoustic compatibility. Compared to gelatine, agar offers a higher melting point, ensuring superior thermal and structural stability at room temperature. Furthermore, its physical properties can be precisely tailored through the addition of specific enhancers: glycerol is utilised to increase the speed of sound, while aluminium oxide (Al_2O_3) or silicon carbide (SiC) is added to optimise the attenuation coefficient and scattering properties, respectively, as detailed by Souza et al. [35]. Additionally, preservatives like benzalkonium chloride (BAC) can be integrated to maintain long-term stability against potential bacterial degradation.

For the specific scope of this project, which focuses on validating the geometric spatial accuracy of ultrasound imaging within a stricture rather than testing dynamic tissue elasticity, the advanced mechanical properties of PVA are not required. Therefore, an agar-based formulation provides a structurally stable, geometrically rigid, and acoustically accurate alternative. This choice fulfills the requirement to maintain stable stricture geometries (as will be discussed in Chapter 4) without the manufacturing complexities and geometric distortions inherent to PVA.

2.4.2 Cadaveric Specimens

While synthetic phantoms offer geometric stability and controlled conditions, human cadaveric specimens provide the primary anatomical reference framework required to evaluate ultrasound imaging under realistic structural conditions. In ultrasound research, the preservation technique applied to the specimen drastically influences both its mechanical flexibility and its acoustic properties, directly impacting the quality of the visualised anatomy [36].

Traditionally, three main types of cadaveric models are discussed in ultrasound literature based on their preservation methods:

- **Formalin-Embalmed Cadavers:** Traditional formalin fixation relies on solutions containing formaldehyde (typically around 4 %), ethanol, glycerol, and phenol perfused under pressure. This process causes extensive chemical cross-linking of proteins, leaving the specimens highly rigid with stiff joints [37]. From an engineering perspective, this severe rigidity limits anatomical manipulation (such as neck rotation), alters the viscoelastic behaviour of tissues, and drastically degrades ultrasound image quality by increasing acoustic attenuation and hindering the clear differentiation of layers.

- **Thiel-Embalmed (Soft-Preserved) Cadavers:** Developed by Professor Thiel in 1992 and adopted by advanced anatomical centres such as the University of Dundee [38], the Thiel method utilises a specialized mixture of salts, boric acid, and morpholine, with minimal concentrations of formaldehyde [36]. This chemical composition avoids protein cross-linking, allowing the specimens to retain lifelike tissue elasticity, natural skin suppleness, and complete passive joint mobility without requiring refrigeration. Crucially for ultrasonography, the fluid distribution in Thiel-embalmed tissues artificially increases the echogenicity of muscles, which enhances the acoustic contrast between muscular structures and surrounding fascial planes [36].

- **Fresh-Frozen Cadavers:** Fresh-frozen specimens are widely considered the gold standard for ultrasound applications focusing on pure, unaltered tissue acoustics. Prepared by keeping the cadavers in deep freezing refrigeration (typically at $-20\,^{\circ}\mathrm{C}$) immediately post-mortem, these specimens avoid the introduction of chemical preservation fluids [36]. Consequently, they undergo zero artificial modifications of their native acoustic impedance, providing excellent native visibility of muscles, fascial boundaries, and vascular structures under ultrasound that closely mimics *in vivo* tissue properties.

While soft-preserved and fresh-frozen models offer high anatomical fidelity, *ex vivo* biological tissues bring specific physical constraints not found in synthetic phantoms or living subjects. For one thing, acoustic properties vary heavily based

on temperature. Living tissues operate at a stable core body temperature of 37 °C, whereas thawed cadaveric specimens are generally scanned at room temperature, typically maintained between 20 °C and 25 °C. This thermal gap lowers the baseline speed of sound across water-based soft tissues, away from the traditional 1540 $\mathrm{m\,s^{-1}}$ calibration and risking minor errors in spatial measurements.

Additionally, because these tissues lack active blood perfusion and internal physiological pressure, compliant structures like the pharyngo-oesophageal lumen tend to partially collapse. Simulating true patency therefore demands manual stabilisation or active fluid instillation. Finally, progressive tissue dehydration and potential post-mortem gas accumulation introduce strong acoustic impedance mismatches, which generate artifacts, such as acoustic shadowing, and increase attenuation.

In the context of the wider research group's work associated with this study, fresh-frozen cadaveric specimens provided by the Laboratory of Human Anatomy at the University of Glasgow [39] were selected to analyse the submental acoustic window using low-frequency (LF) and HF probes, detailed in Chapter 4. While HF transducers provide the superior spatial resolution necessary to identify subtle muscular layers of the tongue and floor of the mouth, their signal attenuates rapidly in biological media, a challenge further exacerbated by post-mortem tissue changes. This specific limitation establishes the direct technical rationale for employing advanced signal processing, such as CE (discussed in Section 2.6.1), to rescue the SNR in highly attenuating biological targets.

2.5 Image Quality Metrics

To quantitatively evaluate and compare ultrasound imaging performance across different configurations, various standard acoustic metrics are used. These allow for an objective, mathematical assessment of image quality, contrast resolution, and signal integrity, suggesting reliable visualisation of the targeted anatomical structures in the neck.

2.5.1 Signal-to-Noise Ratio (SNR)

The SNR is the ratio of the ultrasound signal power to the background electronic and acoustic noise power. In the context of envelope-detected echo signals, it is typically defined within a homogeneous region of interest (ROI) as [40]:

$$\mathrm{SNR} = \frac{\mu_s}{\sigma_s} \tag{2.3}$$

where μ_s represents the mean intensity of the signal in the target ROI, and σ_s is the standard deviation of the background noise floor. Alternatively, expressed in

decibels (dB):

$$\mathrm{SNR}_{\mathrm{dB}} = 20 \log_{10} \left(\frac{\mu_s}{\sigma_s} \right) \tag{2.4}$$

2.5.2 Contrast-to-Noise Ratio (CNR)

The CNR measures the system's ability to distinguish between different tissue types or between a target structure and the surrounding background in the presence of noise. It is mathematically formulated as [40]:

$$\mathrm{CNR} = \frac{|\mu_t - \mu_b|}{\sqrt{\sigma_t^2 + \sigma_b^2}} \tag{2.5}$$

where μ_t and σ_t are the mean and standard deviation of the target tissue ROI, while μ_b and σ_b are the mean and standard deviation of the background tissue ROI, respectively.

2.5.3 Maximum Penetration Depth (MPD)

The MPD defines the maximum distance from the transducer face at which usable acoustic backscattered signals can be detected above the noise floor. It is determined by evaluating the depth, $z_{\max}$, where the local SNR drops to a specific threshold, set at 6 dB in this framework to ensure a robust signal-to-noise margin against acoustic artifacts [41]:

$$\mathrm{MPD} = \sup \{ z \mid \mathrm{SNR}(z) \geq 6\,\mathrm{dB} \} \tag{2.6}$$

2.6 Coded Excitation and Beamforming

To overcome the severe acoustic attenuation highlighted in post-mortem tissue characterisation, advanced transmission strategies and robust reconstruction frameworks must be integrated into the imaging pipeline. Instead of relying on conventional short-pulse transmission, which inherently suffers from a trade-off between penetration depth and spatial resolution, software-defined ultrasound imaging allows for the implementation of complex RF modulation alongside digital spatial focusing.

Converting these raw acoustic echoes into high-resolution diagnostic frames requires a dedicated, two-step processing sequence triggered directly upon signal reception. If the architecture transmits an encoded ultrasound pulse, the incoming backscattered data must immediately undergo pulse compression; this operation

decodes the sequence to reclaim the axial resolution otherwise degraded by attenuating media. Following this compression stage, spatial beamforming algorithms are executed to focus the processed signals into a coherent spatial matrix.

In this study, the practical execution of these advanced software-defined strategies relies on the Verasonics Vantage 128 system, which provides programmable, independent control over individual transmission and reception channels [42]. This section details the theoretical framework of CE and the subsequent beamforming trade-offs implemented to achieve high image quality in highly attenuating biological targets.

2.6.1 Coded Excitation

In conventional medical ultrasound, transducers emit a short, high-amplitude pulse to achieve optimal axial resolution. However, when imaging highly attenuating media, such as post-mortem biological tissues, this standard approach faces a severe physical trade-off between imaging penetration depth and spatial resolution. To increase the SNR in deep or highly attenuating structures, conventional systems are limited to two main strategies: either increasing the pulse excitation voltage, which risks damaging the transducer crystals and biological tissues, or increasing the number of excited oscillations, which inherently degrades axial resolution. To overcome these physical boundaries without compromising spatial resolution or subject safety, advanced ultrasound imaging implements CE techniques.

The fundamental principle of CE involves transmitting a longer, frequency- or phase-modulated pulse sequence that carries a lower peak power but a significantly higher total energy over time [43]. In this work, within the technical framework implemented by the wider research group, a linear frequency modulated (LFM) waveform, commonly known as a chirp, was utilised as the excitation sequence (Figure 2.13a). Upon receiving the backscattered echoes, the long time-scale signal must be decoded to restore spatial accuracy. This pulse compression is achieved via a matched filter, a linear system whose frequency response is the complex conjugate of the input signal, to maximise the output SNR [44]. This compression mechanism condenses the long returning echo into a sharp, narrow pulse, effectively decoupling pulse energy from axial resolution, as shown in Figure 2.13b. However, the compression of LFM waveforms inherently introduces temporal side-lobes resembling a sinc function, which can generate artifacts and compromise imaging clarity.

The complete processing pipeline for the CE sequence is schematically summarised in the flowchart in Figure 2.12. Upon acquiring the raw RF data and the replica of the transmit waveform (TW) from the Verasonics platform, both signals are matched to the system's sampling frequency (125 MHz). The pulse compression is then efficiently performed in the frequency domain by computing the fast Fourier

transform (FFT) of both the RF data and the matched filter. After performing the convolution operation in the frequency domain, the signal is transformed back in the time domain via an inverse fast Fourier transform (IFFT), making it available for the final B-mode image reconstruction.

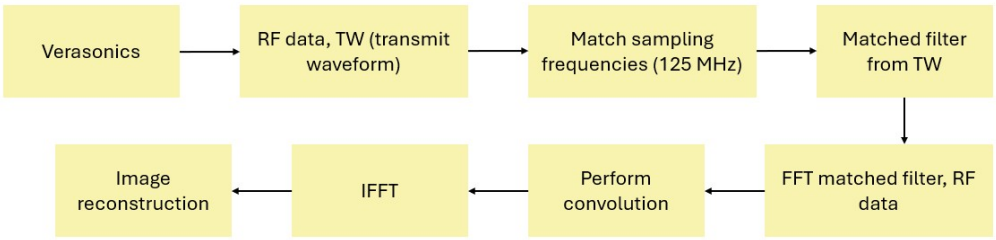

Figure 2.12: Flowchart of the coded excitation (CE) signal processing chain, illustrating the transmission, reception, and matched filtering stages.

For the practical scope of this research framework, this advanced processing pipeline represents a crucial enabling methodology rather than a direct implementation task. While the hardware execution, chirp modulation parameters, and subsequent digital beamforming algorithms were managed and developed by the doctoral researcher X. Miller, understanding their acoustic implications is vital for interpreting the experimental outcomes. The integration of CE allows LF probes and, especially, HF probes to successfully bypass tissue attenuation and resolve the subtle mucosal layers of the submental window. Concurrently, the presence of compression side-lobes highlights the importance of a stable, geometrically rigid validation framework using synthetic phantoms (detailed in Chapter 4), to benchmark structural imaging accuracy under optimised signal conditions.

2.6.2 Beamforming Framework and Performance Trade-offs

Following pulse compression, the reconstructed ultrasound frame is generated through digital beamforming. Within signal processing pipelines, the delay-and-sum (DAS) algorithm remains the most widely implemented technique due to its simplicity, numerical robustness, and computational efficiency [45]. As highlighted by comparative literature, the primary advantages of DAS arise from its data-independent nature: it is easily parallelised and strictly preserves the temporal coherence and statistical properties of the acoustic envelopes.

Despite its widespread popularity, DAS is occasionally criticised in the literature as mediocre, though this is often caused by its suboptimal configuration rather than intrinsic flaws. As demonstrated by Perrot et al. [45], the overall image

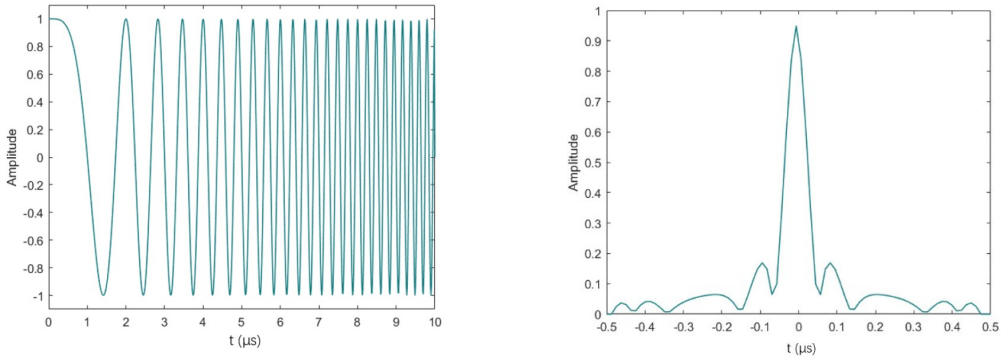

(a) **(b)**

Figure 2.13: Conceptual representation of the coded excitation (CE) process: (a) the transmitted linear frequency modulated (LFM) chirp signal distributes high energy over a long duration; (b) the matched filter output condenses the echo into a sharp, narrow pulse to maximise the signal-to-noise ratio (SNR) while exhibiting characteristic temporal side-lobes (adapted from [43]).

quality, specifically in terms of lateral resolution and CNR, is heavily dependent on the precise pre-setting of physical and geometric parameters, most notably the receive aperture settings and the assumed speed of sound. If these parameters are neglected or improperly calibrated, severe image degradation occurs, particularly when imaging highly attenuating or non-homogeneous targets.

Bypassing the resolution limits inherent to standard operators demands alternative, data-dependent frameworks, such as the adaptive minimum-variance (MV) beamformer [46]. Instead of relying on fixed weights, these advanced methods dynamically tune the signal composition using incoming data samples, which effectively sharpens spatial resolution and cuts down on acoustic artifacts. The core bottleneck, however, lies in their data-dependent nature: adaptive beamforming schemes are based on an exponential increase in computational complexity. This makes them heavily expensive in terms of processing latency when measured against the linear, straightforward operations of standard DAS [45].

Therefore, for the practical scope of this research framework, the DAS algorithm was selected as the optimal baseline. A properly designed and optimised DAS framework can be highly effective even in challenging imaging scenarios, providing a robust, fast, and computationally viable reference architecture, establishing a stable geometric starting point before further computational optimisations are introduced.

Chapter 3

Design and Integration of the 14 MHz Flexible Interface

This chapter details the practical implementation of the hardware interface between the ultrasound transducer array and the digital acquisition system. The primary objective was the development of a high-density, 128-channel fPCB system designed to bridge the gap between specialised medical transducers and the Verasonics Vantage 128 research platform (Vantage 128, Verasonics Inc., Kirkland, WA, USA) [42] equipped with the UTA 260-S universal transducer adapter. This hardware interface was specifically optimised to preserve signal integrity within the 14 MHz centre frequency range of the array.

The chapter begins with a comparative analysis of the transducer prototypes evaluated within the research group, justifying the selection of the 14 MHz array over previous 25 MHz and 28 MHz iterations, with their different characteristics. The focus of the chapter then shifts to the technical challenges addressed during the layout and routing phase using EasyEDA design software (EasyEDA, Shenzhen, China); these include managing high-density routing with a 0.15 mm pad pitch, ensuring 50 Ω impedance matching, and implementing mechanical strain relief. It also documents an initial attempt at a preliminary electrical characterisation focused exclusively on the transducer array pins. While encountering critical connectivity issues at this stage that prevented its completion due to project schedule constraints, this highlighted the practical challenges of handling the micro-pitch elements before full system integration. Finally, the complete hardware architecture is presented as an integrated solution capable of acting as a bridge between the selected transducer and the research acquisition system.

3.1 Transducer Selection and System Rationale

A foundational step in the broader development of the wearable monitoring system framework was the selection of a suitable transducer array. This choice was driven by a comparative analysis of three distinct prototypes, with the aim of identifying the optimal trade-off between the spatial resolution and acoustic penetration depth required for continuous monitoring applications.

Evaluation of Preliminary Prototypes Prior to the current design phase, a preliminary evaluation and comparison of two alternative HF array configurations was conducted by X. Miller to assess their suitability. This comparative analysis led to the rejection of those initial designs, with the findings subsequently presented at the CEEUS 2026 conference [47].

- **28 MHz Single-Crystal Array (Vermon, France):** A rigid 128-element array with an ultra-fine pitch of 0.07 mm. While providing outstanding axial resolution, its operating frequency caused severe signal attenuation in tissue. This resulted in poor depth penetration that remained inadequate for deep neck structures, even when deploying advanced CE techniques intended to improve penetration without sacrificing resolution.
- **25 MHz Flexible Thin-Film Array (Novosound, UK):** A 32-element array with a piezoelectric thin-film deposition on a metal substrate. Despite its ergonomic flexibility, it exhibited overall weak signal transmission and severe element dropout issues at higher voltages, likely linked to the thin-film manufacturing technique. Furthermore, the flexible nature of the substrate introduced element position uncertainty when conformed to complex anatomical surfaces like the neck, causing significant complications for phase coherence during image reconstruction.

As shown in Figure 3.1 and quantitatively summarised in Table 3.1, the **14 MHz Linear Array (Vermon, France)**, model **LA 14.0/192-2100**, was ultimately selected as it represents the optimal trade-off for this application. It provides sufficient penetration depth to reach deep neck structures while maintaining a spatial resolution high enough for real-time biofeedback.

However, implementing this transducer introduced a substantial integration challenge. Unlike the alternative custom configurations previously evaluated, the 14 MHz array featured a hockey-stick geometry but was completely unhoused, requiring the development of custom hardware interfaces and dedicated software configurations to establish a functional connection with the Verasonics research ultrasound platform.

As a consequence, the author's contribution focused on the hardware integration of the selected 14 MHz array. With its 192 elements and dual-tab architecture, this array required a significantly more complex interconnection strategy than the previous prototypes. This necessitated the development of high-density custom fPCBs to bridge the gap between the transducer tabs and the Verasonics system, managing both the strict geometric tolerances and the impedance matching requirements.

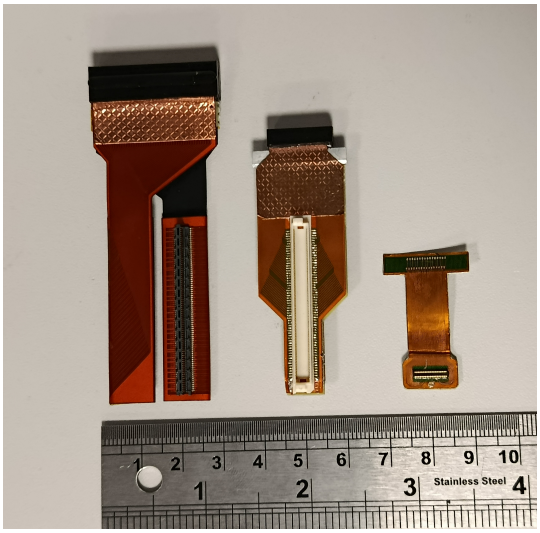

Figure 3.1: Comparison of the high-frequency (HF) transducer arrays: the 14 MHz Vermon array (left), the rigid 28 MHz Vermon array (centre), and the flexible 25 MHz Novosound array (right). The ruler highlights the dual-tab architecture and the larger physical footprint of the 14 MHz array compared to the other prototypes (adapted from [47]).

Table 3.1: Geometric and acoustic specifications of the evaluated high-frequency (HF) ultrasound arrays.

Parameter	**14 MHz Array**	**28 MHz Array**	**25 MHz Array**
Centre Frequency (MHz)	13.3	28	25
Number of Elements	192	128	32
Pitch (mm)	0.15	0.07	0.30
Configuration	Rigid (Hockey Stick) / Custom	Rigid / Custom	Flexible / Custom

3.2 Transmission and Data Acquisition System: Verasonics Vantage 128

To collect data in real time and apply advanced signal processing, the transducer array needed to be integrated with a high-performance ultrasound research platform. For this work, a Verasonics Vantage 128 system equipped with a UTA 260-S was applied as the central digital back-end.

The Vantage 128 platform configuration provides up to 128 independent transmit and receive channels. From a functional perspective, the Vantage architecture allows full software-programmable control over individual channel excitation pulse shapes, apodization profiles and raw radio frequency (RF) data saving, making it an ideal reference architecture for characterising custom transducers [42].

However, there was a significant mismatch between the two components: while the custom 14 MHz probe featured a total of 192 acoustic elements, the Vantage 128 system was physically limited to 128 active channels. This meant a direct connection was not possible, and some of the elements of the array had to be left unconnected within the routing matrix. A custom interfacing hardware solution was therefore required to handle the channel down-mapping while adaptive routing accommodated the micro-pitch pad layout. The design of this custom board, including parameters choice, channels mapping strategies and geometric constraints, is the main engineering focus of this chapter.

3.3 14 MHz Transducer Characteristics

As established by the selection criteria, the LA 14.0 transducer introduced specific architectural complexities for the design of the custom interface.

Technical Specifications According to the manufacturer's data [48], the LA 14.0 operates at a centre frequency f_c of 13.3 MHz ($\pm 10\%$). It consists of 192 piezoelectric elements with a pitch of 0.15 mm and an element width of 0.135 mm. These parameters ensure high spatial resolution but impose strict requirements on signal routing density for the custom interface.

Physical Architecture and Connection Tabs The electrical interface of the LA 14.0 is physically split into two separate flexible tabs, which manage the even and odd numbered elements respectively. Each tab terminates with a Samtec Ultrafine Pitch Header (P/N: ST5-80-1.00-L-D-P-TR) [48]. This architecture posed a significant interfacing challenge: signals had to be routed from these two distinct flexible connectors into the acquisition system without compromising signal integrity.

Interfacing Requirements To integrate this transducer with the Verasonics platform, a custom hardware solution was needed with some key constraints:

1. **Mechanical Adaptation:** The system needed to ensure a stable connection for the two flexible tabs, adapting them to the Verasonics interface cable for custom arrays.

2. **Channel Mapping:** A strategy was necessary to map the 192 elements of the array to the 128 available channels of the UTA 260-S interface.

3. **Impedance Matching:** To minimise reflections at 14 MHz, it was essential for the signal paths to maintain a controlled 50 Ω characteristic electrical impedance throughout the interface.

3.4 Hardware Architecture

The hardware interface was designed using a modular approach to manage a total of 128 signal channels, consisting of two identical 64-channel fPCBs operating in parallel. In this architecture, one module was dedicated to the transducer's odd-element flexible tab, while the second handled the even-element tab. This configuration was chosen to simplify the routing complexity of the high-density traces and to ensure the maintainability of the probe assembly. The primary objective of the system was to bridge the connection between the transducer elements and the Verasonics platform. To achieve this, specific connectors were selected for each interface:

- **System side**: A Panasonic AXK5F70547YG female connector [49] was utilised to match one plug of the Verasonics cable, featuring 70 pins (64 active signal pins and 6 ground (GND) pins).

- **Transducer side**: A Samtec SS5-80-3.00-L-D-K-TR female socket [50] with 160 pins was selected to connect one tab of the array.

A specific pin mapping strategy was implemented to accommodate the 128-channel limitation of the acquisition system while optimising the active aperture of the 192-element transducer. The transducer signals are split onto two symmetric tabs, providing 96 active elements per side. Consequently, each designed fPCB interfaces with a connector featuring 160 total pins, organised into 96 active signal pins and 64 GND pins.

To match the hardware constraints of the Verasonics platform, only 64 active channels were routed from each fPCB ($64 \times 2 = 128$ total channels), focusing exclusively on the central elements of the array to maintain a centred and symmetrical

imaging aperture on the probe face. This configuration left $96 - 64 = 32$ available signal pins as not connected (NC) per fPCB.

To preserve symmetry, these 32 unused signal elements were equally divided between the ends of the array, meaning 16 active pins at the beginning and 16 active pins at the end of the signal sequence were left NC. Due to the interlaced distribution of signal and ground lines within the connector geometry, these 16 boundary signal channels correspond exactly to the first 26 total physical pins (13 on each side of the connector rows) and the last 26 total physical pins (13 on each side), respectively.

The grounding strategy was implemented by adhering to the technical specifications of both interfaces to ensure shielding continuity. For the transducer side, the ground pin distribution followed the specific pattern of the Vermon flexible tabs to minimise return path loops. On the system side, the grounding scheme followed the Verasonics cable datasheet requirements [51]. This layout provided a low-impedance path to the reference ground using the dedicated pins of the Panasonic connector. This organisation of signal and ground lines directly affected the high-density routing of the board. Here, trace geometries were designed for clear impedance matching and good inter-channel isolation (Figure 3.3).

It is worth noting that, within the EasyEDA schematic shown in Figure 3.2, the SS5-80-3.50-L-D-K-TR library model was temporarily adopted as a virtual component, since it was the only available footprint matching the required 160-pin configuration. The numerical variation between the two part numbers relates to the nominal stack height, changing from 3.00 mm for the physical socket to 3.50 mm for the digital model. Since both variants share the exact same land pattern and footprint geometry, this software substitution had no impact on trace routing or pad placement, while the correct physical spacing was preserved during the manual assembly phase.

3.4.1 Layout Constraints and Signal Integrity

The routing parameters for the fPCB were defined in accordance with IPC-2223 standards for flexible circuits [52], ensuring both mechanical reliability and a controlled impedance of 50 Ω, as specified in IPC-2141A [53]. To maintain signal integrity at the 14 MHz operating frequency, the design has a surface microstrip configuration where the top layer carries the signal traces and the bottom layer acts as a continuous ground plane, separated by a 1 mil (25 µm) Polyimide core.

Impedance Control and Trace Geometry To prevent signal reflections and image artifacts, the characteristic impedance (Z_0) of the fPCB traces was designed to match the 50 Ω standard of the acquisition system. This matching is critical to comply with the "Maximum Power Transfer Theorem", ensuring the signal is

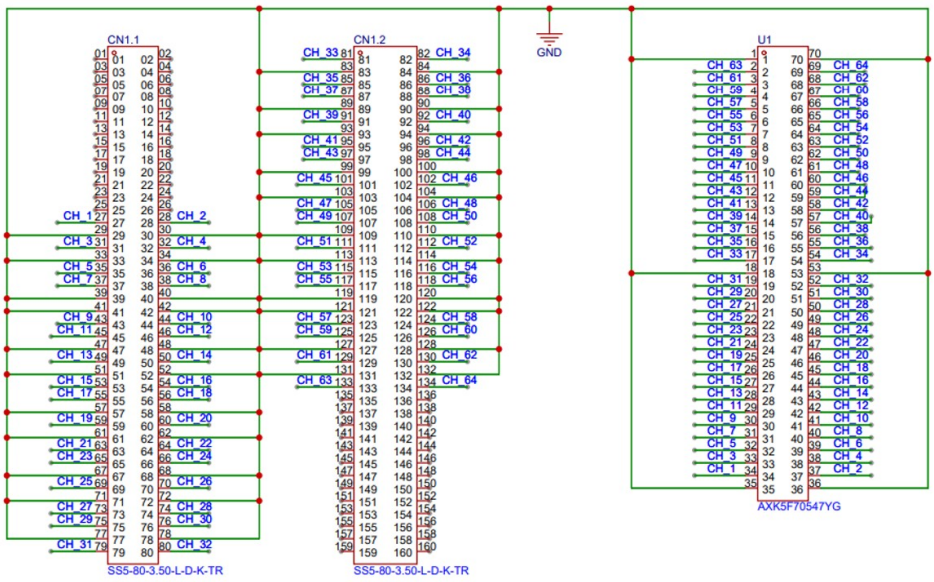

Figure 3.2: Schematic design of the 64-channel flexible printed circuit board (fPCB) module. The diagram illustrates the pin-mapping strategy between the Samtec SS5 series connector (transducer-side) and the Panasonic AXK5F series connector (system-side). The routing and grounding schemes were implemented to match the specific requirements of the Vermon array tabs and the Verasonics interface cable, respectively, ensuring shielding continuity across the entire signal path.

conducted from the transducer to the system with minimal loss and preventing parasitic reflections that would otherwise lead to "ghost" artifacts.

Given a substrate height, $h = 25\,\mu\text{m}$, and a relative permittivity of the polyimide core, $\epsilon_r \approx 3.4$, the characteristic impedance was calculated with the empirical formula from the IPC-2141A standard [53]:

$$Z_0 = \frac{87}{\sqrt{\epsilon_r + 1.41}} \ln\left(\frac{5.98h}{0.8W + t}\right) \tag{3.1}$$

where W is the trace width and t is the copper thickness. This layout gives a target value of $Z_0 \approx 50\,\Omega$. A specific 2:1 width-to-height ratio was chosen (2 mil on a 1 mil core, which means 50 µm width on a 25 µm core); this choice effectively balances the inductive and capacitive parts of the transmission line, keeping the impedance controlled and lowering return loss.

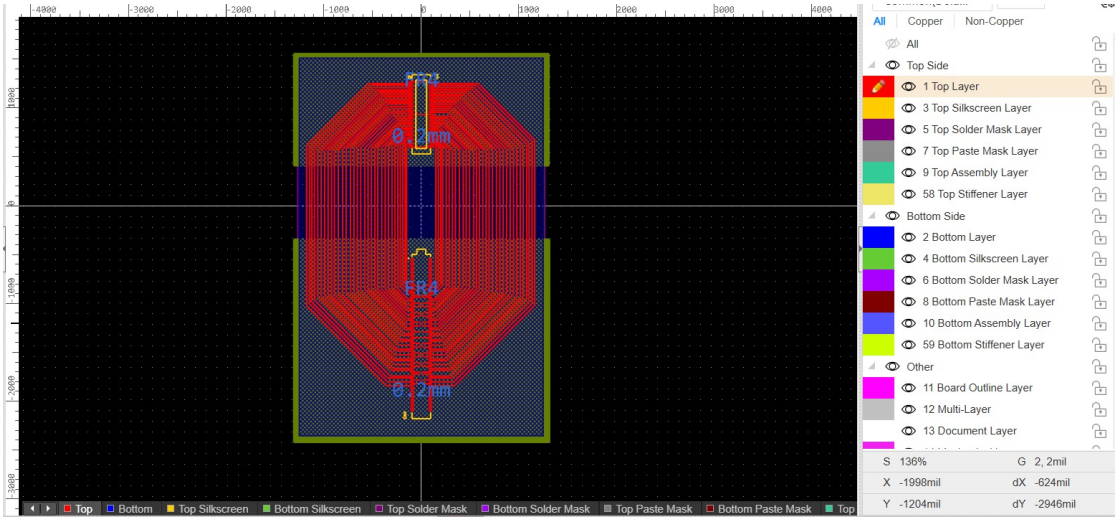

Figure 3.3: High-density routing layout of the flexible printed circuit board (fPCB). The red traces represent the copper traces for signals on the top layer, optimised for 50 Ω impedance and maximised inter-channel isolation to mitigate electromagnetic coupling.

Routing Strategy and Crosstalk Mitigation A direct routing strategy was prioritised over length-matching serpentines to further protect signal quality and minimise parasitic cross-talk. At the operating frequency of 14 MHz, the signal period (T) is approximately 71.4 ns. The maximum length difference between the shortest and longest traces ($\Delta L \approx 73$ mm) introduces a propagation delay mismatch (Δt) that can be calculated using the transmission line relations defined in IPC-2141A [53]:

$$\Delta t = \frac{\Delta L \cdot \sqrt{\epsilon_r}}{c} \approx \frac{0.073\,\text{m} \cdot \sqrt{3.4}}{3 \times 10^8\,\text{m/s}} \approx 0.45\,\text{ns} \tag{3.2}$$

where c is the speed of light in vacuum and ϵ_r is the relative dielectric constant of the polyimide substrate. This relative delay mismatch represents less than 0.7 % of the total signal period, which is well within the acceptable tolerance margins for ultrasound beamforming phase coherence. Therefore, the effect is negligible, justifying the use of direct routing.

To accommodate the high-density requirements of the 64 signal channels within the restricted footprint, the trace clearance was reduced from the default 10 mil (250 µm) to 2 mil (50 µm). This reduction allowed all signal paths to be routed through the extremely tight geometry of the component pins.

To further ensure signal integrity, the spacing between adjacent signal traces was managed according to the standard $3W$ rule guidelines for crosstalk mitigation

[53]. This design rule specifies that the centre-to-centre distance between two parallel traces should be at least three times the width (W) of a single trace. By implementing this layout constraint, the mutual electromagnetic coupling (crosstalk) was significantly reduced, keeping the electric and magnetic fringe fields associated with each signal path sufficiently isolated.

In the specific case of this fPCB, given the 2 mil (50 µm) trace width, a target separation of 6 mil (150 µm) between trace edges was maintained where the connector density permitted, balancing the need for high-density routing with the requirement for low inter-channel interference.

The combination of this precise clearance and the 50 Ω impedance control led to three main results:

- **Minimised Reflections:** Signal flow at the 14 MHz central frequency remained smooth.
- **Crosstalk Mitigation:** Physical isolation followed the $3W$ rule where feasible, despite high-density constraints.
- **SNR Optimization:** Power transfer from the piezoelectric elements to the front-end acquisition electronics was efficient, maximising the SNR.

3.4.2 Material Specifications and Stackup

The fPCB utilizes a 25 µm Polyimide core, selected for its mechanical flexibility and ability to support high-density routing. To ensure structural integrity during clinical use and planarity during the assembly, FR4 stiffeners (0.20 mm thickness) were applied locally to the connector areas, as shown in Figure 3.4.

FR4, a composite material made of woven fiberglass cloth with an epoxy resin binder, was selected for its high strength-to-weight ratio and excellent dimensional stability. This rigid backing supported the mating forces of the micro-connectors, preventing mechanical stress on the sub-millimetric solder joints and keeping the rest of the functional circuit flexible.

The final layout was then exported in Gerber format for fabrication by JLCPCB (Shenzhen, China). During this stage, a design for manufacturing (DFM) check confirmed all high-density constraints.

3.5 Preliminary Electrical Characterisation

Before the final assembly of the custom fPCB interface, a preliminary electrical characterisation of the 14 MHz transducer array was conducted. The objective was to establish a functional benchmark and ensure the uniformity of the piezoelectric elements before permanent integration with the custom hardware.

Table 3.2: fPCB Layer Stack-up and Thickness

Layer	**Material**	**Thickness (µm)**
Top Coverlay	Polyimide + Adhesive	27
Top Layer (Signals)	Electro-deposited Copper	12
Core (Dielectric)	Polyimide (PI)	25
Bottom Layer (GND)	Electro-deposited Copper	12
Bottom Coverlay	Polyimide + Adhesive	27

Figure 3.4: Close-up view of the flexible printed circuit board (fPCB) connector region showing the localised rigid stiffener layer underneath the component pads.

3.5.1 Measurement Setup and Technical Challenges

The characterisation was performed using an E4990A Impedance Analyser (Keysight Technologies, Santa Rosa, CA, USA). To contact the high-density pads of the array's "Odd Tab", standard hook-tip test leads were adapted by soldering a pair of fine-gauge twisted wires to the tips. This custom-made extension was necessary to reach the miniature pads. The measurement was conducted under the visual guidance of a Plus 2 digital microscope (Mic-Fi, Rivoli, TO, Italy) to ensure precise positioning of the tips, as illustrated in the complete laboratory setup in Figure 3.5a. Prior to the measurements, an open-short calibration compensated for the leads' impedance.

However, the process faced major physical and electrical difficulties. The 0.15 mm pitch of the pads made manual probes positioning difficult and the layout caused parasitic capacitance effects, which distorted impedance readings above 10 MHz. Furthermore, the fragility of the flexible tabs imposed a conservative approach to probing to avoid permanent damage to the transducer, requiring continuous monitoring of the contact point under microscopic guidance (Figure 3.5b).

3.5.2 Observations and Experimental Constraints

The preliminary impedance measurements performed on the "Odd Tab" elements yielded inconsistent results, primarily due to the extreme difficulty of maintaining stable electrical contact on the sub-millimeter pitch pads. The manually adapted

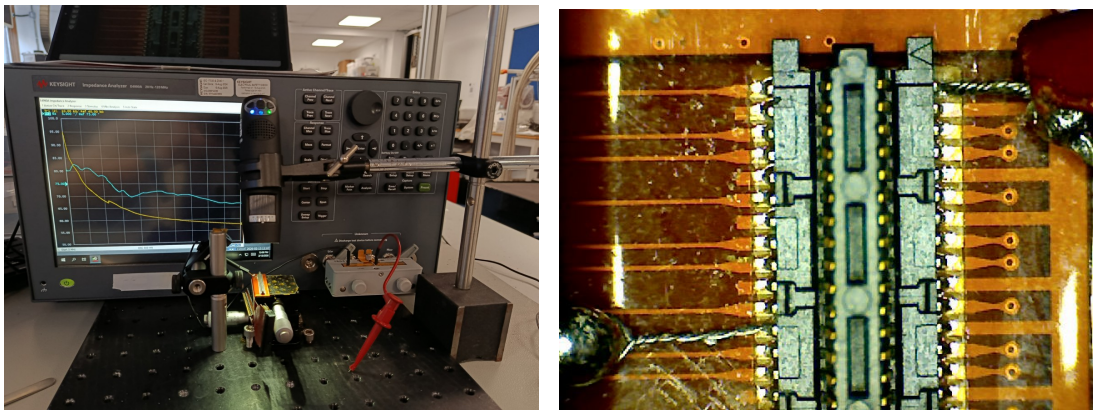

(a) **(b)**

Figure 3.5: Preliminary characterisation phase: (a) laboratory setup for baseline electrical validation using the Keysight E4990A impedance analyser and the Mic-Fi digital microscope; (b) microscopic view of the transducer pins (0.15 mm pitch) during the procedure.

probes, while providing the necessary reach, introduced significant contact resistance and parasitic fluctuations. Despite initial open-short calibration attempts, the instability of the manual contact at high frequencies masked the expected resonance and anti-resonance peaks of the piezoelectric crystals.

At the 14 MHz operating frequency, minor instabilities in the probing setup distorted the phase readings. Due to these limitations and the risk of damaging the fragile flexible tabs, hardware integration became the main priority. As a result, electrical characterisation was suspended to focus on the final assembly.

Further experimental validations, including pulse-echo tests and water tank field mapping, were deferred to a later testing stage due to project schedule constraints and the need to advance the system development workflow. It was determined reliable functional verification will be more effectively performed once the transducer is securely connected to the fPCB, at which stage stable paths will allow for comprehensive validation of the full system in a controlled environment.

3.6 Final Assembly and Physical Realisation

Upon receiving the manufactured prototypes from JLCPCB, the assembly of the high-density connectors was performed via manual micro-soldering by X. Miller. Given the sub-millimetric pitch of the pads and the thermal sensitivity of the polyimide substrate, a low-temperature solder paste was applied, and the process was carried out using ultra-fine soldering tips under microscopic guidance. Precise

thermal management was maintained around 200 °C to prevent the formation of solder bridges and ensure reliable electrical contact. At this stage, the localized FR4 stiffeners proved critical: they acted as a thermal and mechanical barrier, providing a rigid, planar surface that effectively prevented the ultra-thin polyimide core from warping or deforming under the thermal stress of the soldering iron (Figure 3.6a). The successful completion of this micro-soldering phase enabled the final physical realisation of the custom interface, with the 14 MHz transducer successfully connected to the two fabricated boards, as shown in Figure 3.6b.

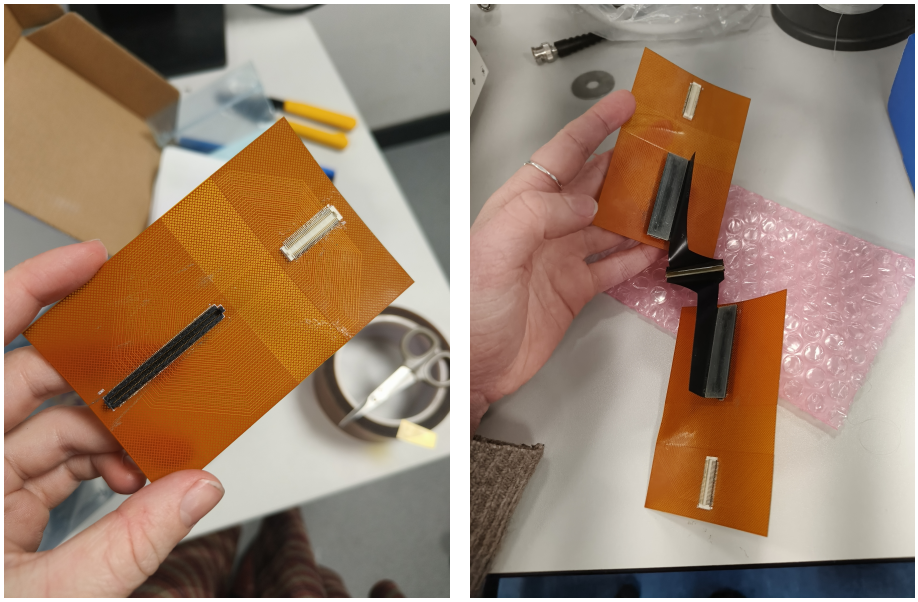

(a) **(b)**

Figure 3.6: Physical realisation of the custom interface: (a) overview of the soldering quality and mechanical reinforcements of a flexible printed circuit board (fPCB); (b) complete assembly with the 14 MHz transducer connected to two boards.

Chapter 4

Experimental Validation: From Tissue-Mimicking Phantoms to Cadaveric Specimens

Validating the ultrasound imaging strategy involved a series of experimental steps detailed in this chapter. Work focused on evaluating the custom hardware performance alongside the phantoms' structural fidelity. Initial testing used a basic phantom to verify how the agar-based matrix handled acoustic stability. After confirming these material properties, a complex TMM was designed to simulate a cervical oesophageal stricture. This model was created using an optimised casting protocol to reduce the structural inconsistencies and artifacts found during the first testing phase.

Validation of this model was performed with a SonixTouch Q^+ (BK Medical, Herlev, Denmark) clinical ultrasound system. This instrumentation acted as a benchmark to evaluate the intrinsic trade-off between spatial resolution and penetration depth. By using the SonixTouch probes at their operational limit, up to 30 MHz, this study demonstrates that extreme HF arrays, while providing superior morphological detail, lack the penetration required to fully visualise the extent of such oesophageal pathologies.

This finding confirms the technical and clinical justification for the development of a 14 MHz system for this specific application. Clinical validation also showed the phantom is suitable not just for high-resolution B-mode imaging detailed but also has potential for bolus dynamic testing. By simulating the real-time passage of food through the stenotic segment, the phantom proved a versatile tool

that, by capturing transient fluid-structure interactions, bridges the gap between static morphological characterisation and functional clinical scenarios. Custom mechanical interfaces and a multi-operator protocol were required during these dynamic trials to keep experimental stability and get repeatable data.

The custom 14 MHz HF array was then tested on cadaveric specimens. This moved the work from a controlled TMM environment to a real biological setting. The system performance was evaluated in this complex environment, verifying the robustness needed for future clinical translation steps.

4.1 Development of Tissue-Mimicking Phantoms

To conduct the preliminary acoustic validation of the developed flexible interface, a dedicated TMM was required. The phantom was prepared by adopting an agar-based formulation originally proposed by Souza et al. [35] and subsequently modified and validated within the research group by L. Buzzatto [54] for HF ultrasound applications. In his work, the recipe was optimised by fixing the agar concentration at 2.03 % and removing the silicon carbide scatterers originally present in the literature recipe, relying exclusively on the fine aluminium oxide particles to provide a uniform acoustic backscattering matrix. This specific chemical baseline is summarised in Table 4.1.

Table 4.1: Composition of the 2.03 % agar tissue-mimicking material, showing the weight percentage and corresponding mass for each component.

Component	**Weight (%)**	**Weight (g)**
Glycerol	11.38	21.220
Deionized Water	85.79	160.00
Benzalkonium Chloride	0.480	0.8900
Al_2O_3 (0.3 µm)	0.160	0.3000
Al_2O_3 (3 µm)	0.160	0.3000
Agar	2.030	3.7900
Sum	**100.00**	**186.50**

4.1.1 Fabrication Procedure

The fabrication process was executed by adopting the research group's established laboratory protocol as a baseline framework, aiming to ensure a uniform and bubble-free sample block. This structured approach provided the operational guidance for producing the custom tissue-mimicking structures required for the

subsequent hardware validation phases. While the core guidelines were derived from standardised practices, the procedure was locally adapted to accommodate specific laboratory constraints and material availability. The main phases of the production protocol are illustrated in Figure 4.1.

Reference Protocol The preparation of TMM followed a structured protocol to ensure chemical homogeneity and acoustic stability. The procedure is described as follows:

1. **Solvent Preparation:** The required mass of water was measured using a precision balance and transferred to an Erlenmeyer flask.
2. **Heating and Evaporation Control:** The flask was placed on a digital hot plate (MS-H280-Pro, Camlab, Cambridge, UK), set between 200 °C and 250 °C. The opening was sealed with aluminium foil to prevent evaporation, thus maintaining the precise concentration of the components.
3. **Thermal Monitoring:** Thermal measurements were performed using a Dual Channel Digital Thermometer (RSPRO1316, RS Components Ltd, Corby, UK) connected to Type-K thermocouples. It was used to monitor the temperature by piercing the foil seal.
4. **Solute Preparation:** While heating the water, the following components were weighed and combined in a separate beaker:
   - Glycerol (acoustic attenuator);
   - 3 µm (B8052, Logitech Ltd, Glasgow, UK) and 0.3 µm (210517, Logitech Ltd, Glasgow, UK) particles of Aluminium Oxide: scatterers;
   - BAC (80001-54-5, Trade Chemicals LTD, Blackpool, UK): preservative/antimicrobial agent.
5. **Pre-mixing:** Glycerol, scatterers, and BAC were stirred using a glass rod until a homogeneous slurry was obtained.
6. **Integration of Components:** Once the water reached approximately 70 °C, the glycerol-based mixture was added to the flask.
7. **Gelation Agent:** Agar (AS1296, Merck KGaA, Darmstadt, Germany) powder was then added to the solution under constant magnetic stirring (Figure 4.1a).
8. **Thermal Processing and Incubation:** The solution was heated to a temperature range of 80 °C to 90 °C and maintained within this interval for one hour to ensure full gelation and homogeneity (Figure 4.1b).

9. **Controlled Cooling and Casting:** The mixture was allowed to cool naturally to approximately 40 °C. It was poured into the mould under a fume hood to ensure safety and minimise environmental contamination.

10. **Setting and Preservation:** The phantom was allowed to set at room temperature for 24 h. A protective layer of water and glycerol was then added to the top surface to prevent dehydration before final refrigeration.

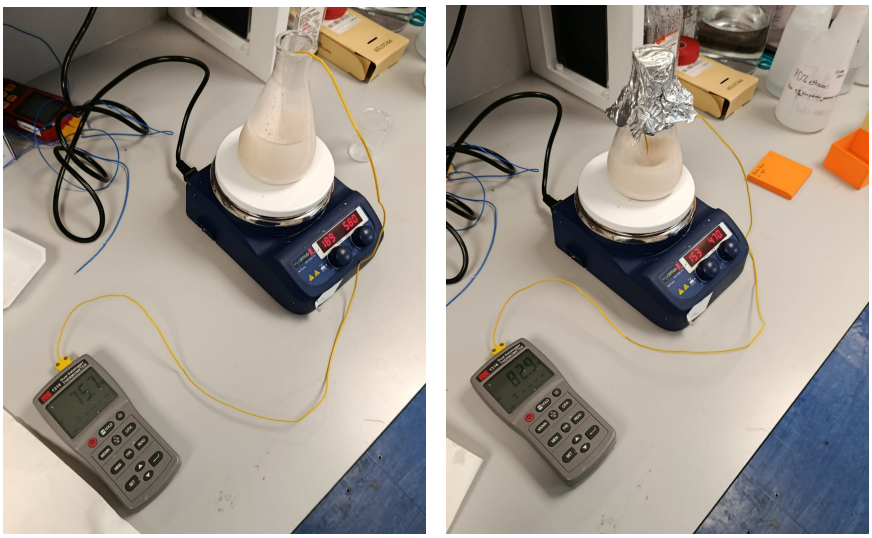

(a) **(b)**

Figure 4.1: Phases of tissue-mimicking material (TMM) preparation using the Camlab MS-H280-Pro hotplate: (a) initial mixing stage reached at 75.7 °C; (b) incubation phase with a protective foil seal maintained at 82.9 °C.

Experimental Deviations and Observations During the activity, the following adjustments were implemented. These include both refinements to the protocol and deviations necessitated by laboratory constraints:

Refinement: Mould Preparation To facilitate the extraction of the phantom and prevent mechanical damage to its structure, a thin layer of petroleum jelly (Cotton Tree, Manchester, UK) was applied to the inner surfaces of the mould.

Deviation: Water Source Tap water replaced deionised water due to a temporary lack of availability. Deionised water is standard for chemical purity and to prevent ion-related acoustic interference. A boiling process was used

to degas the solvent: this action lowered the risk of air bubbles, ultimately protecting the ultrasound signal clarity.

Deviation: Evaporation Control The flask remained uncovered for the first 30 min of heating. An aluminium foil seal was applied later when it became available. Extra water was added at the start to compensate for evaporation, but the final mixture was not weighed before casting. Therefore, the 2.03 % agar concentration is a nominal value and any minor deviation is negligible for the scope of this study.

Adjustment: BAC Measurement BAC was measured by mass rather than volume. Since its role is antimicrobial and not acoustic, this approach provided sufficient accuracy without compromising the phantom's performance.

4.1.2 Preliminary Validation: Plain Phantom

To perform the initial acoustic coupling checks and verify the fundamental signal transmission through the custom fPCB interface, a preliminary validation was conducted on a baseline plain phantom. For this initial test block, the TMM was prepared by maintaining the exact reference masses summarised in Table 4.1 (total of 186.50 g), ensuring a direct correlation with the group's validated baseline performance.

The mechanical containment for the liquid mixture during the setting phase was provided by a custom rigid mould. It was fabricated via fused deposition modelling (FDM) using a Bambu Lab P1S 3D-printer (Bambu Lab, Shenzhen, China), equipped with a 0.4 mm nozzle and operating at a standardised layer height of 0.2 mm. The internal geometry of the 3D-printed enclosure featured nominal dimensions of 70 mm×40 mm×70 mm, providing an optimised volume to host the reference formulation without requiring any scaling factors.

Once the gel had reached full structural setting, the plain phantom was used as an acoustic test target to confirm functionality of the custom fPCB interface designed in this work, detailed in Chapter 3. This setup was essential to verify that the routing successfully established the connection between the 14 MHz transducer array and the Verasonics platform.

This initial hardware verification confirmed a satisfactory acoustic backscattering uniformity and the absence of major structural artifacts within the agar core. Testing then shifted towards macro-structural one, requiring extended laboratory sessions. Due to the shared scheduling constraints of the Verasonics research platform, subsequent characterisations on larger scaled phantoms were transitioned onto a dedicated SonixTouch Q^+ ultrasound system. This allowed for systematic testing of the other version of the phantom without monopolising the primary

research platform, while relying on the interface connectivity already demonstrated in this preliminary phase.

4.1.3 Oesophageal Model Design

The phantom was designed to provide a controlled environment for evaluating ultrasound performance in the context of PESs. While oropharyngeal dysphagia involves complex neuromuscular coordination and irregular anatomical structures, this study focuses on the structural manifestations of post-treatment fibrosis, which often result in significant narrowing within the cervical segment of the digestive tract.

Design Requirements The phantom was designed to be anatomically realistic while remaining practical for the technical constraints of ultrasound testing. Focusing on the cervical anatomy provided a stable and reproducible geometry and avoided the more complex muscles of the pharyngeal region. The cubic mould dimensions provided a wide surface area for probe contact while remaining manageable during casting.

The lumen centre was positioned at a depth of 30 mm reflecting its posterior position relative to the trachea. It also represents a rigorous test for HF transducers, matching their maximum effective scanning range. For the diameters, a healthy lumen represented the upper physiological range of a distended oesophagus. An 8 mm benchmark was chosen for the stenotic region to simulate critical clinical narrowing.

The specific geometric parameters resulting from these considerations are summarised in Table 4.2.

Table 4.2: Design parameters for the oesophageal phantom.

Parameter	**Value**
Overall Mould Size	80 mm×80 mm×80 mm
Healthy Lumen Diameter	20.4 mm
Stenotic Lumen Diameter	8.0 mm
Target Depth (Centre of Lumen)	30.0 mm

3d-Printing and Casting The physical realisation of the phantom required the design of custom tooling to ensure precise geometry and long-term stability. This was done with computer-aided design (CAD) software (Fusion 360, Autodesk,

San Rafael, CA, USA). Production used a Bambu Lab P1S configuration with a 0.4 mm nozzle and 0.2 mm layer height.

Three primary 3D-printed elements formed the system: the internal lumen inserts, a mould lid, and flanged storage caps. The inserts consisted of two mirrored conical segments. They defined the biconical lumen geometry during the casting and gelation of the agar-based mixture. To increase the structural rigidity of these conical inserts, the infill density was set to 50 % with a grid pattern. Tree supports helped maintain the integrity of the geometries, providing a smooth surface finish for easier post-processing. The flanged caps and the custom-fit lid provided an airtight seal. This setup prevented dehydration of the TMM to ensure long-term preservation of the phantom. The technical specifications for these components, including printing parameters and dimensions, are summarised in Table 4.3.

Table 4.3: Manufacturing specifications for the 3D-printed tooling components.

Component	**Mechanical Detail**	**Value/Feature**
Mould Lid	Dimensions	84.5 mm×84.5 mm; Height: 12 mm
	Wall Thickness	2.0 mm
Lumen Inserts	Architecture	Two mirrored conical segments
(2 units)	Surface Finish	Smooth (0.2 mm layer)
Storage Caps	Geometry	Mushroom-shaped flanged seal
(2 units)	Plug Interface	Matches external mould ports
	Head Diameter	Ø 25.87 mm (Housing for sealing clay)

As illustrated in Figure 4.2, the inserts were designed to meet at the centre of the housing, forming the 8.0 mm stenotic neck. The pre-casting assembly (Figure 4.2c) was carefully inspected to ensure that the inserts were perfectly coaxial and that the structure was watertight, preventing leaks of the liquid TMM during the solidification phase.

4.1.4 Ultrasound Imaging Validation

Following the fabrication phase, preliminary ultrasound imaging was performed to validate the phantom's structural integrity and evaluate its acoustic appearance. This validation checked if the TMM provided a homogeneous background and a correctly defined internal geometry. The process had two distinct phases: structural verification with the 3D-printed polylactic acid (PLA) inserts still inside, and evaluation of the hollow lumen after insert extraction. The BK SonixTouch Q^+ ultrasound system was used for all acquisitions.

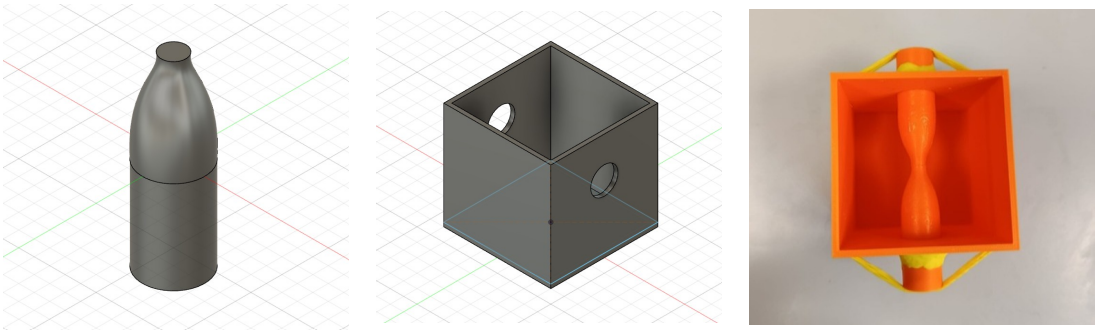

(a) **(b)** **(c)**

Figure 4.2: Design and pre-experimental setup: (a) Computer-aided design (CAD) model of a conical lumen insert; (b) CAD representation of the external mould housing; (c) visual inspection of the final assembly pre-casting. The setup includes petroleum jelly for easier extraction, elastic bands to maintain axial alignment against the pressure of the hot agar, and sealing clay to prevent leaks at the insert ports.

Structural Verification with PLA Inserts Imaging started on the phantom before extracting the 3D-printed lumen inserts. This configuration allowed for a direct assessment of the geometric accuracy of the design. The phantom was imaged using two different commercial linear transducers to compare their performance: a Linear Array L40-8/12-GEN-General (HF probe, set to 15 MHz) and a Linear Array L14-5/38-VAS-General (LF probe, set to 10 MHz).

As illustrated in Figure 4.3, significant differences are visible between the two probes. The HF probe (15 MHz, Figure 4.3a) provides high resolution in the superficial tissue, as evidenced by the clear representation of the cavity's top surface. However, its low penetration depth (set to 30 mm, which is the maximum depth that the probe can reach), does not provide sufficient depth of field to visualise deeper sections of the oesophageal lumen and stenosis.

In contrast, the LF probe (10 MHz, Figure 4.3b) allows for a significantly higher depth of field (set to 7.50 cm), making the entire hourglass geometry of the stenosis visible. This configuration is better suited for visualising the complete target volume within the 80 mm cube, despite a slight loss of resolution.

Acoustic Artifacts from PLA Infill In the LF image (Figure 4.3b), the presence of acoustic artifacts within the PLA inserts is prominent. The upper surface of the inserts is extremely bright (hyperechoic). This is due to the strong acoustic impedance mismatch between the agar matrix and the solid PLA exterior, causing the majority of the ultrasound wave to be reflected at this interface.

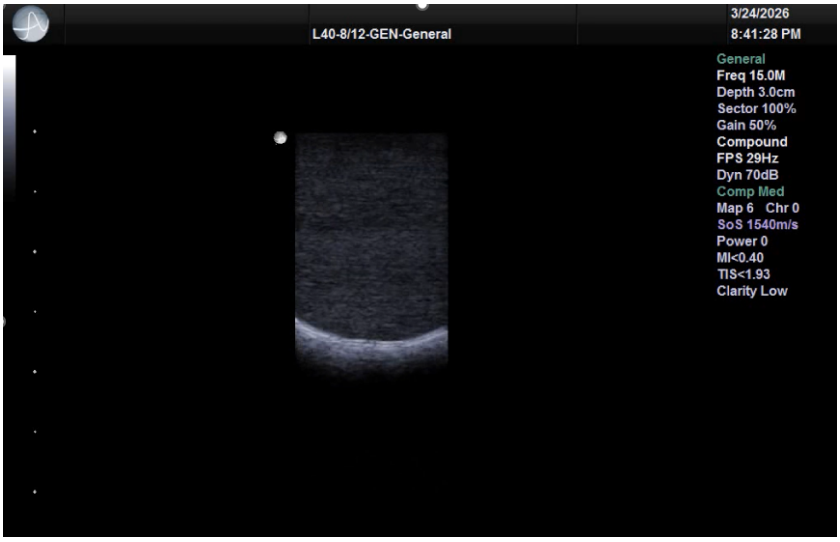

(a)

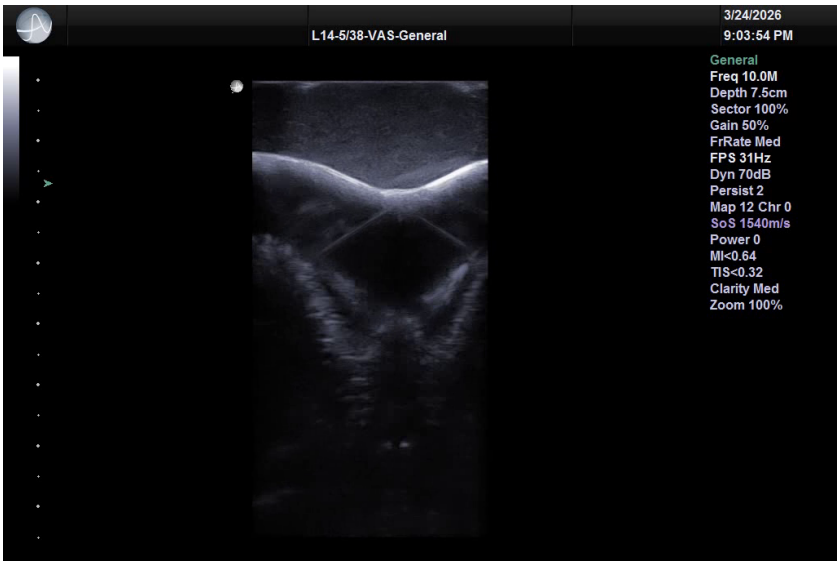

(b)

Figure 4.3: B-mode ultrasound imaging comparison between high-frequency (HF) and low-frequency (LF) transducers with custom polylactic acid (PLA) inserts in place: (a) the HF probe (15 MHz) is restricted to the superficial layer due to higher attenuation, whereas (b) the LF probe (10 MHz) configuration provides a sufficient field of view to capture the entire stenosis profile.

Furthermore, repetitive, equidistant patterns, characteristic of "ghost artifacts", appear inside and beneath the inserts. This pattern stems from their internal structure, specifically the 50 % grid infill noted in Table 4.3. This setup created a porous interior where PLA alternated with air-filled gaps. Because air acts as a near-perfect ultrasound reflector, multiple reflections between the insert surfaces and these air pockets caused the observed "ghost artifacts".

Deeper in the matrix, a distinct duplication of the lumen's lower boundary is visible. This effect is likely a mirroring artifact, where the highly reflective top surface of the insert acts as an acoustic mirror to create a false duplication of deeper structures. The central section of the phantom still shows a clear, symmetrical biconical profile. In the longitudinal plane, this profile resembles a "butterfly" shape, marking the transition toward the 8.0 mm stenotic neck. The sharp convergence of these hyperechoic boundaries confirms the precise axial alignment of the two mirrored inserts during the casting process. Ultimately, while these preliminary scans validate the geometric accuracy of the phantom, they also confirm that the PLA inserts must be removed to achieve an artifact-free acoustic lumen for subsequent experimental phases.

Acoustic Validation and Attenuation Analysis without PLA Inserts
Following the structural verification, the PLA inserts were extracted to assess the acoustic behaviour of the finalised oesophageal phantom. This stage focuses on evaluating the hollow lumen's visibility and the attenuation properties of the agar-based matrix without the interference of 3D-printing artifacts. To ensure optimal ultrasound coupling and prevent air-related reflections, the resulting cavity was filled with the previously described water-glycerol mixture.

As shown in Figure 4.4, a preliminary visual inspection confirmed that the agar matrix successfully maintained the complex biconical geometry. The resulting hollow lumen appeared smooth and stable, with no signs of structural collapse or deformation.

To perform the acoustic validation, the resulting cavity was then filled with the previously described water-glycerol mixture. This step was crucial to eliminate air-related acoustic interfaces at the inner boundary, which would otherwise cause total ultrasound reflection.

While the initial scans with the inserts (Figure 4.3) were primarily used to verify the correct positioning of the components, the post-extraction imaging (Figure 4.5) serves as the final validation of the phantom's acoustic quality. In these final B-mode scans, the most striking improvement is the complete disappearance of the large "butterfly-shaped" ghost artifacts that affected the earlier setup. The TMM matrix now appears perfectly homogeneous, confirming that the casting and extraction protocol successfully eliminated internal delamination and air trapping.

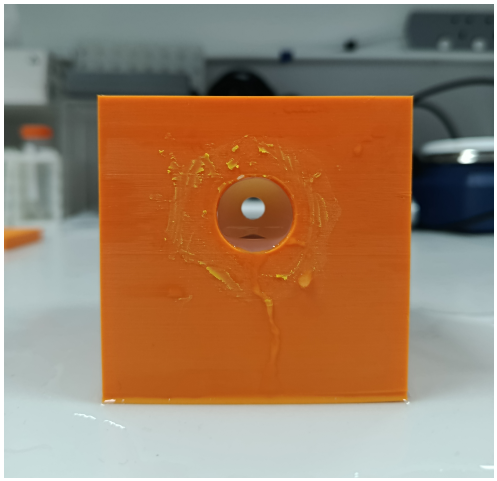

Figure 4.4: Visual inspection of the oesophageal phantom after the successful extraction of the 3D-printed lumen inserts. The image confirms the structural integrity of the gel matrix, showing a well-defined, smooth hollow lumen that has not collapsed.

In Figure 4.5a, the HF probe was intentionally operated at its maximum frequency of 30 MHz to maximise the spatial resolution. This allowed for better characterisation of the 8.0 mm stenotic neck, providing a detailed view of the wall morphology. Nevertheless, the inherent penetration limit of this HF setting (30 mm) remains a physical constraint, preventing the visualisation of the entire structure in a single field of view.

In contrast, with the 10 MHz imaging in Figure 4.5b, the entire lumen and the mould's bottom reflection are clearly visible, demonstrating the phantom's correct acoustic attenuation. However, at this frequency, reverberation artifacts are detectable inside the lumen cavity. Furthermore, the wall definitions do not appear uniformly bright at every point. This non-uniform brightness is primarily due to the varying angle of incidence between the ultrasound beam and the curved biconical surface; as the walls slope away from the probe, the specular reflection back to the transducer decreases. Additionally, microscopic residues of petroleum jelly remaining after the insert extraction may contribute to the local loss of definition at the interface and to the reverberation artifacts inside the cavity.

Post-Testing Assessment and Long-term Storage Post-fabrication, the preservation of the phantom's structural and acoustic properties was addressed through a specific storage protocol. The internal cavity was completely filled with a mixture of water and glycerol (in an approximate 9:1 volume ratio) to prevent the dehydration of the agar-based matrix. As illustrated in Figure 4.6, the filling

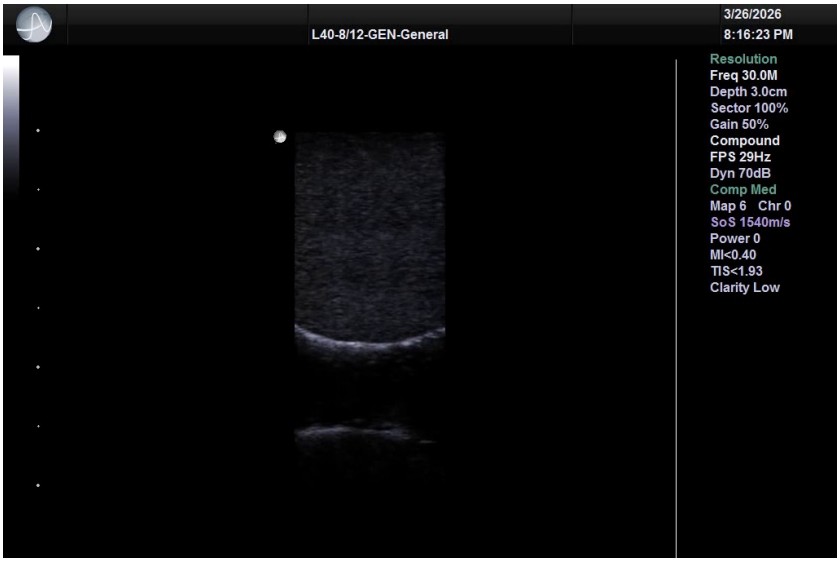

(a)

(b)

Figure 4.5: B-mode ultrasound scans of the phantom after insert extraction: (a) the high-frequency (HF) probe (30 MHz) provides high-resolution details of the stenotic tract, whereas (b) the low-frequency (LF) probe (10 MHz) shows the full geometry and the bottom reflection of the mould, with minor interface artifacts visible inside the lumen, possibly due to petroleum jelly residues.

procedure was performed by tilting the mould diagonally, with one lateral hole sealed by a storage cap. The mixture was then carefully injected into the cavity using a syringe through the opposite open hole to minimise air entrapment. Once the lumen was completely filled, the second cap was secured.

Prior to final sealing, any residual coupling gel from the imaging sessions was carefully removed, and a final layer of the mixture was poured over the phantom's top surface before the assembly with the lid. To ensure a hermetic, watertight barrier, the flanged heads of the caps were reinforced with a non-drying modelling clay (ColorClay, Scola, Winsford, UK). This method proved effective in preventing fluid leakage and dehydration during refrigerated storage between experimental sessions.

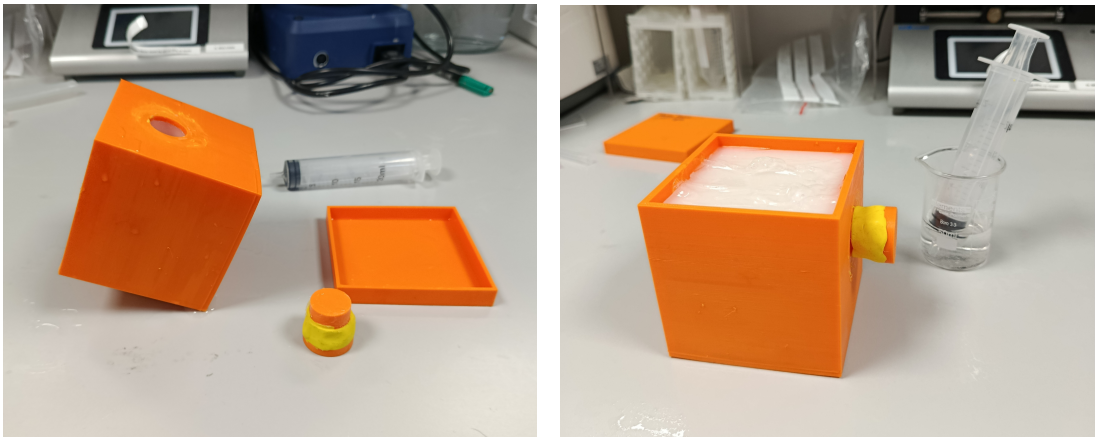

(a) **(b)**

Figure 4.6: Phantom storage preparation: (a) filling of the lumen with a water-glycerol mixture via a syringe, with the mould tilted to prevent air bubbles; (b) final setup with lateral caps reinforced with modelling clay to ensure a hermetic seal during refrigeration.

4.1.5 Dynamic Bolus Transit Validation

The final experiments on TMM phantoms involved dynamic validation of the bolus transit through the stenotic model. Previous tests used static conditions to check the basic acoustic visibility of the lumen. In contrast, this stage captured the interaction between a moving fluid and the lumen geometry. This step required major changes in the experimental workflow to resolve technical challenges with system hermeticity and operational management.

Specifically, the following sections detail the transition from initial unsuccessful attempts to an optimised setup. This progression involved overcoming substantial

sealing challenges and the implementation of a collaborative two-operator protocol. This coordination was essential to manage simultaneous requirements, while ensuring the digital preservation of the ultrasound scans via mobile recording.

By documenting the refinements made to the hydraulic circuit and the selection of the bolus simulant, this section provides an overview of the strategies implemented to mitigate acoustic artifacts. Although air entrapment remained a challenge during the sessions, these adjustments aimed to preserve bolus integrity as much as possible, allowing for a meaningful qualitative analysis of the transit dynamics despite the noise in the ultrasound sequences.

Experimental Design and Materials The setup used a modular structure for stability and acoustic coupling, incorporating the following items:

- **Imaging System**: The SonixTouch Q^+ system with the LF probe.
- **Fluid Delivery**: A 20 mL manual syringe to inject the food bolus and fill the circuit.
- **Hydraulic Components**: Two flexible transparent tubes for visual flow and water level monitoring.
- **Bolus Material**: Commercial plant-based yogurt (Alpro Plain No Sugar, Alpro, Ghent, Belgium). This specific product mimics food consistencies used by therapists in clinical SLT dysphagia assessments. Structurally, its non-Newtonian, shear-thinning behaviour models human bolus transit better than water. Nutrition facts show 2.3 g of fats and 4.0 g of proteins per 100 g, adding natural acoustic scatterers for tracking. Pectins and acidity regulators stabilise viscosity, while sea salt (0.24 g/100 g) alters the medium's acoustic impedance. Every trial started immediately after taking the product from the fridge to prevent temperature-induced viscosity shifts.
- **Acoustic Coupling**: Gel and water eliminated air gaps between probe and phantom for clear signal transmission.
- **Structural Support**: An optical breadboard with mechanical clamps held the components in alignment.

Interface Development: The Sealing Challenge Achieving a leak-proof connection between the hydraulic circuit and the phantom proved to be one of the most significant experimental hurdles, requiring an iterative design approach.

1) First Attempt: Modelling Clay Seal The initial sealing strategy involved the use of modelling clay to bridge the gap between the inlet/outlet tubes and the external mould.

- **Design**: The tubes (inner diameter of 10.0 mm and outer diameter of 17.0 mm) were inserted into the mould's 20.4 mm holes. The clay was packed around the junction and secured with elastic bands to hold it against the 3D-printed mould.

- **Failure Analysis**: This method was unsuccessful as the modelling clay lacked the necessary structural rigidity and adhesion to seal the 3.4 mm radial gap. Under the pressure of the fluid, the seal failed immediately, leading to significant water leakage.

2) Second Attempt: 3D-printed Gaskets To solve the structural failure of the first attempt, a custom mechanical solution was developed. Hollow cylindrical caps (gaskets) were specifically designed and 3D-printed to seal the clearance between the tube and the mould orifice. The gasket featured an outer diameter of 20.0 mm to precisely fit the mould frame, and an inner diameter of 18.2 mm. Although the nominal outer diameter of the silicon tube was 17.0 mm, the inner diameter of the enclosure was intentionally oversized to accommodate material tolerances and potential thermal shrinkage of the 3D-printed polymer, and to facilitate smooth manual assembly without inducing structural stress on the tube.

Although these caps were originally designed with an internal groove intended to house modelling clay, the sealing strategy was adapted during the final assembly to better suit the laboratory conditions:

- **Implementation**: The caps acted as a rigid adapter. To ensure a hermetic seal, modelling clay was applied only to the external spot before the head of the cap (Figure 4.7b), rather than within the internal groove. To address the remaining clearance between the tube and the cap's internal surface, several layers of absorbent paper were wrapped around the interface. This improvised gasket effectively filled the gap and provided a snug fit, while also acting as a secondary barrier to absorb potential micro-leakages. Finally, elastic bands were applied to keep the entire assembly under constant pressure.

- **Result**: This hybrid mechanical seal provided the necessary resistance to withstand the transit of fluids, allowing the experiment to proceed without losses even during high-pressure injections.

Experimental Setup I and Technical Challenges The first attempt to visualise the bolus transit was characterised by a highly manual and "open" configuration. This phase was crucial to identify the practical challenges of the experiment, particularly regarding fluid dynamics and coordination. The procedure was conducted as follows:

(a) **(b)**

Figure 4.7: Evolution of the phantom-tubing interface: a) first sealing attempt using modelling clay and elastic bands; b) second sealing attempt with custom 3D-printed gaskets.

- **Assembly**: The phantom was placed on an optical breadboard with the SonixTouch Q^+ probe secured longitudinally via a standard laboratory clamp. The hydraulic circuit consisted of long, flexible transparent tubes connected to the phantom's internal channel.

- **Pre-filling**: To fill the channel, the tubes were held vertically using auxiliary supports, such as clamps, paper rolls and containers, and filled with water using a flask (Figure 4.8a).

- **Bolus Injection and Data Acquisition**: A 20 mL syringe was used to introduce the yogurt bolus into the inlet tube. Simultaneously, the recording was initiated on the SonixTouch Q^+ system to capture the dynamic transit. Immediately after injection, the outlet tube was manually lowered into a waste tray to allow for gravity-assisted flow, as shown in Figure 4.8b, while additional water was poured from a flask to push the bolus through the phantom channel.

As mentioned in Figure 4.8, the first setup revealed technical challenges that hindered the quality of ultrasound acquisitions and the reproducibility of the experiment:

- **Fluid Dynamics and Bolus Fragmentation**: Yogurt bolus fragmentation from unstable fluid dynamics was the main technical failure. Water delivery from a flask failed: it injected too much volume at an excessive, non-uniform velocity. This effect and the high curvature of the long tubes destroyed the yogurt's cohesion before it reached the phantom. Instead of a single mass for

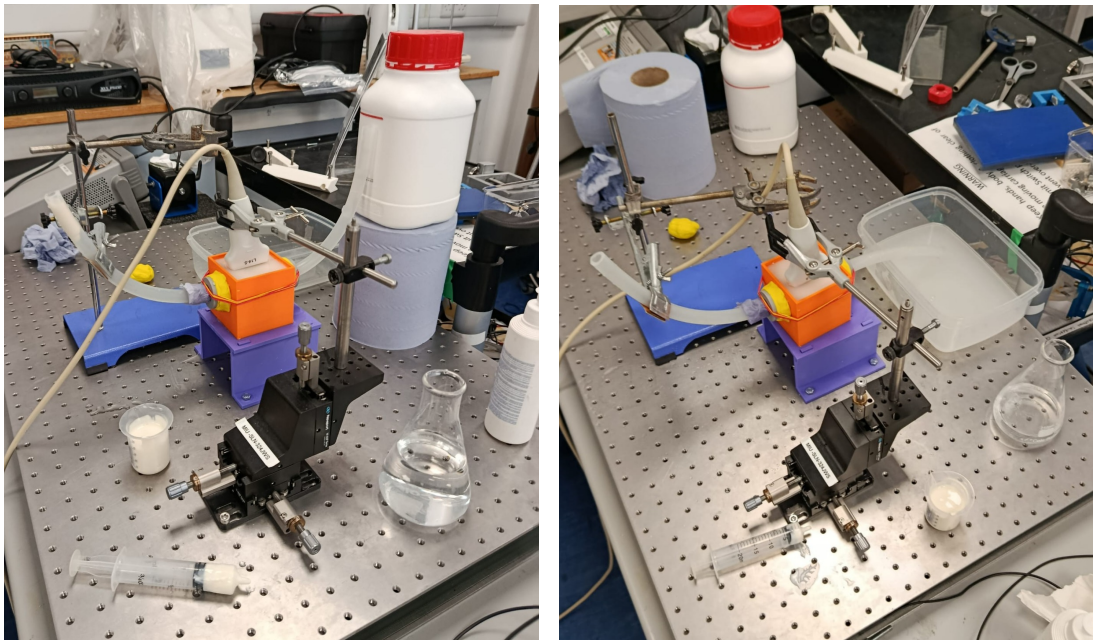

(a) **(b)**

Figure 4.8: Initial experimental setup that highlighted critical issues in manual fluid management and circuit geometry: a) pre-filling: tubes positioned vertically using supports; b) post-test: yogurt and water collected in the waste tray after the transit.

clinical SLT swallow assessments, the flow dispersed into particles. The setup could not replicate real clinical conditions.

- **Air Entrapment**: The rapid pouring from the flask and the vertical orientation of the tubes led to air entrapment. As documented in a relevant ultrasound frame (Figure 4.9), air bubbles acted as total acoustic reflectors; this created artifacts, visible as opaque vertical shadows on the right side of the image, which obscured the distal portion of the phantom's internal channel.
- **Probe Instability**: The manual adjustment of the standard laboratory clamp required a level of precision that proved difficult to maintain consistently during the bolus injection; even a slight rotation or tilt of the probe meant losing the alignment with the centre of the channel, making it hard to secure a stable and repeatable view of the bolus transit during manual manipulation.
- **Operational Complexity and Monitoring**: Running the experiment alone caused a major "blind spot". Having both hands busy with the tubes, supports,

and injection prevented real-time monitoring of the SonixTouch Q^+ screen. Because of this missing visual feedback, internal lumen issues, like the air artifacts, were discovered only during post-test review.

- **Data Loss and Technical Failures**: Even the post-test analysis was severely hindered by hardware limitations of the SonixTouch Q^+ system. Being an older generation device, the system exhibited significant instability when writing data to external universal serial bus (USB) storage. Consequently, the recordings of the actual bolus transit were not successfully captured. The only viable evidence retrieved was a recording of the post-transit phase, showing yogurt fragments suspended within the lumen: a definitive proof of the bolus fragmentation.

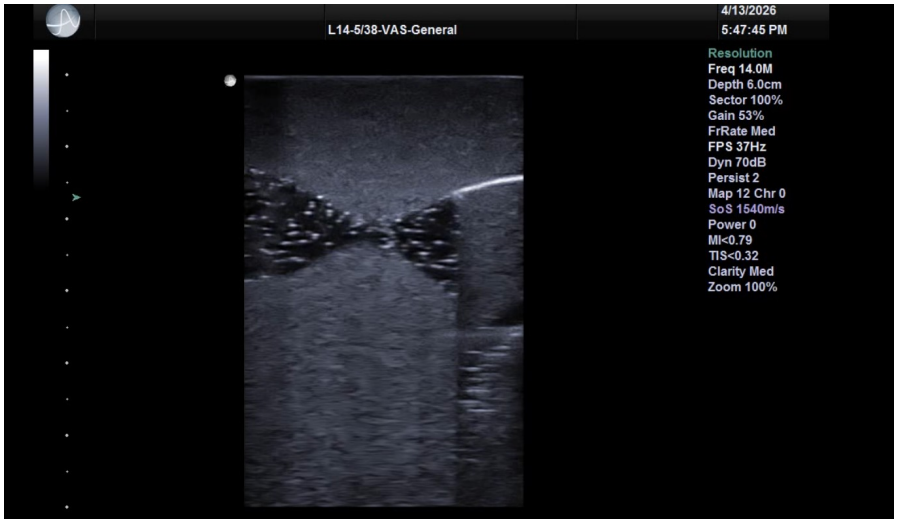

Figure 4.9: Longitudinal ultrasound scan of the oesophageal phantom during the post-transit phase (setup I). The image illustrates two critical limitations of the initial setup: (1) bolus fragmentation, visible as hyperechoic yogurt particles drifting within the lumen instead of a cohesive mass; and (2) acoustic shadowing, visible on the right side of the frame as an opaque artifact caused by air entrapment, which partially obscures the distal portion of the channel.

Experimental Setup II and Optimised Protocol A second experimental phase resolved the initial limitations. This stage updated the physical setup and created a collaborative protocol for data repeatability. Physical adjustments reduced experimental variables (Figure 4.10):

- **Tube Optimization**: Shortening the transparent tubes minimised flow resistance. Also, horizontal positioning limited the gravitational acceleration behind the previous bolus fragmentation.

- **Improved Probe Alignment**: With the help of a colleague, the laboratory clamp was carefully calibrated. This adjustment allowed for a superior longitudinal alignment of the probe, resulting in a significantly clearer acoustic view into the phantom's internal channel.

- **Controlled Fluid Displacement**: The use of a flask was entirely replaced by the syringe for both pre-filling and "push" phase. This facilitated a more uniform velocity and a "gentler" displacement of the bolus.

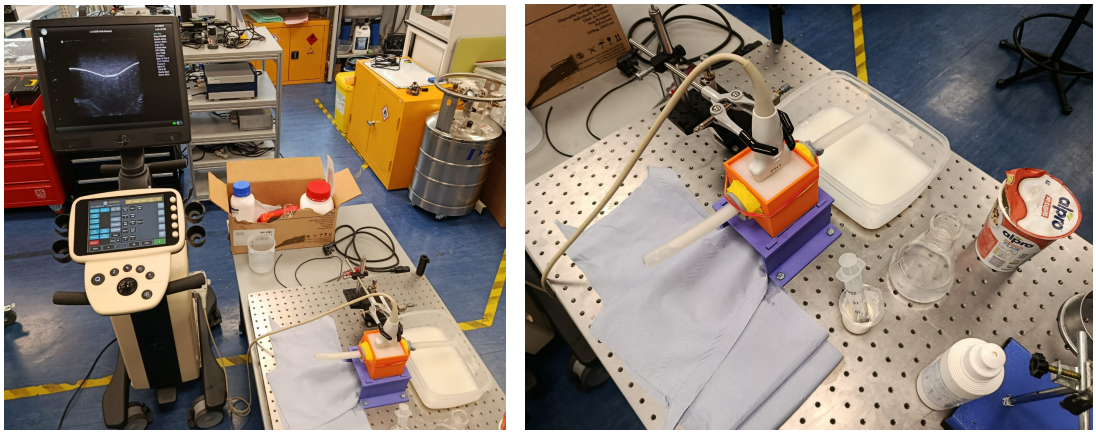

(a) **(b)**

Figure 4.10: Optimised experimental setup. The configuration highlights the collaborative protocol and the physical refinements, such as the use of shortened horizontal tubes to minimise gravitational effects and ensure bolus integrity.

A collaborative two-person workflow replaced individual operation to handle the system layout. The first operator injected the yogurt bolus and managed the subsequent water flush; this syringe delivery maintained a constant, lower-pressure flow than the flask method. Meanwhile, the second operator moved the outlet tube into the waste tray during transit while recording the SonixTouch Q^+ screen with a mobile phone for digital data preservation.

The experimental trials successfully demonstrated the effectiveness of the collaborative two-operator protocol. This coordination ensured that, for the first time, video data of the dynamic transit were successfully captured and preserved for post-test analysis.

The effectiveness of the developed interface and the overall experimental setup is qualitatively confirmed by the ultrasound imaging results. As shown in Figure 4.11, the transit of the yogurt bolus through the phantom's stenotic geometry was clearly captured:

- **Bolus Approach (Figure 4.11a)**: Illustrates the initial entry phase where the yogurt, acting as a contrast agent, allows for a clear identification of the bolus front approaching the narrowing.
- **Bolus Compression (Figure 4.11b)**: Shows the yogurt bolus as it goes through the stenotic tract; the deformation of the bolus highlights the high-pressure conditions generated during the manual injection.
- **Bolus Residuals (Figure 4.11c**): Provides insights into the post-transit phase, showing the remaining material distribution within the restricted lumen once the main flow has subsided.

The video data showed technical challenges despite a successful bolus transit capture due to the setup design:

- **Acoustic Shadowing and Air Entrapment**: Air bubbles trapped during manual pre-filling and injection stayed during the trials. High yogurt viscosity blocked micro-bubble evacuation. Also, surface tension at the phantom-fluid interface caused issues. Manual injection inside a non-pressurised circuit caused localised air pockets. These accumulations caused severe acoustic artifacts, including a "butterfly-shaped" shadow beneath the lumen due to the high acoustic impedance mismatch between air and the surrounding media. However, these artifacts were treated as a constant background and did not prevent the qualitative assessment of the bolus-stenosis interaction within the visible portion of the channel.
- **Ambient Lighting Reflections**: The use of a camera to record the SonixTouch Q^+ screen introduced minor chromatic artifacts and glare from the laboratory's overhead lighting. While these reflections are visible in the frames (Figure 4.11), they do not overlap with the region of interest, thus preserving the interpretability of the results.
- **Flow Discontinuity**: The transition between the yogurt injection and the subsequent water push required a brief pause to reload the syringe. While this resulted in a momentary halt of the bolus within the stenosis, it provided a unique opportunity to observe the bolus's structural stability and resistance to deformation under static conditions.

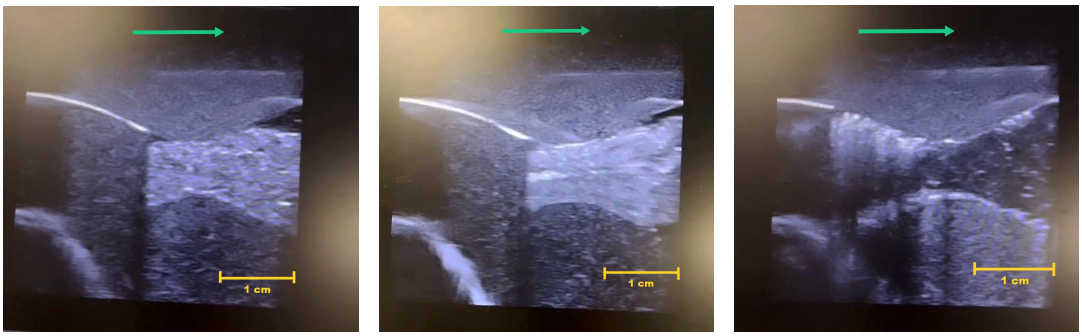

(a) **(b)** **(c)**

Figure 4.11: Representative ultrasound frames extracted from a video showing the bolus transit dynamics. Despite minor ambient lighting reflections, the interaction between the yogurt bolus and the stenotic geometry is clearly discernible: a) bolus approach; b) bolus compression; c) bolus residuals. The green arrows indicate flow direction (left to right); the yellow scale bar represents an estimated length of 1 cm, derived from a nominal image depth of 4 cm.

4.2 Validation on Cadaveric Specimens

To assess the clinical potential of the proposed ultrasound imaging strategy, two experimental sessions were conducted on cadaveric specimens:

- **Session I (December 2025)**: Commercial HF and LF probes provided a performance baseline on the Verasonics Vantage 128 research platform.
- **Session II (March 2026)**: The custom 14 MHz array underwent validation, with comparative clinical data gathered via the SonixTouch Q^+ system.

Tissue-mimicking phantoms allowed initial protocol optimisation in a controlled setup. Even so, real human tissue features complex acoustic properties and anatomical variations. *Ex vivo* studies handled this environment.

The *ex vivo* work followed institutional safety and ethical rules. Cadaveric specimens were provided by the Anatomy Facility of the University of Glasgow [39], and all imaging procedures were performed under the required permissions and oversight of the facility's technical staff.

4.2.1 Session I: Baseline Assessment (December 2025)

The first experimental session aimed to establish a performance baseline using the Verasonics system. Two commercial transducers were evaluated: the L35-16v HF probe and the L11-5v LF probe [42].

Cadaveric Preparation The donors were provided by the Anatomy Facility of the University of Glasgow [39]. Specimens were placed in a supine position with the head extended to maximise the exposure of the submental and laryngeal regions [55]. Prior to imaging, the skin was prepared to ensure optimal acoustic coupling.

Imaging Protocol Focused on key anatomical landmarks relevant to swallowing dynamics, such as suprahyoid muscles (digastric, mylohyoid, and geniohyoid), hyoid bone and laryngeal structures. To enhance image quality, various pulse compression waveforms were implemented via MATLAB (R2022a, The Mathworks, Cambridge, UK)-based scripts, specifically testing 1-cycle and 8-cycle chirp excitations.

Operational Role and Data Acquisition Biosafety protocols for cadaveric specimens limited the author's role to the technical management of the research platform. This task involved configuring the Verasonics Vantage system, running the MATLAB scripts for standard and CE, and supervising data acquisition in real time. Additional tasks covered the storage and organisation of RF and in-phase and quadrature (I/Q) data. These data represent the demodulated, complex-amplitude form of acoustic echoes split into orthogonal In-phase (I) and Quadrature (Q) components. This management ensured consistent imaging parameters across all probe positions.

Despite these advanced signal processing techniques, the session confirmed that the HF probe (L35-16v) suffered from excessive attenuation in biological tissues, failing to provide reliable visualisation of deep structures.

4.2.2 Session II: 14 MHz Array Validation (March 2026)

The second session was designed to overcome the penetration limits observed in the previous trials by testing the 14 MHz array. This session represented a crucial milestone for the validation of the custom hardware developed during this thesis, serving as a direct field test for the solutions engineered to bridge the research platform and the transducer.

Custom fPCB Performance This phase validated the custom fPCB described in Chapter 3. Its performance in a complex biological environment proved the effectiveness of the design's impedance matching and signal integrity measures.

Experimental Setup and Integration The donor was placed in a supine position with maximum neck extension, mimicking the first session. Anatomy Facility staff handled the cadaveric specimens, while the author managed hardware integration and monitored signal stability. Imaging targeted the submental and laryngeal regions [56].

Clinical Benchmarking The SonixTouch Q^+ clinical system provided high-quality reference scans of the targeted anatomy alongside the research setup. This "ground truth" imaging establishes a clear clinical benchmark to validate the features identified by the research platform.

4.2.3 Qualitative Ultrasound Analysis and Comparison

This section qualitatively compares the ultrasound scans from both experimental sessions. The evaluation checks how the custom hardware integration and the operational frequency shift affect image quality, tissue penetration, and anatomical landmark visibility.

Low-Frequency Standard vs. High-Frequency Coded Excitation Session I trials illustrated the physical trade-offs of ultrasound propagation in complex biological tissues. As shown in Figure 6.1a, the commercial LF probe (L11-5v) in standard mode achieved excellent penetration depth, delineating deeper neck muscle layers and tissue interfaces without advanced processing.

Conversely, the commercial HF probe (L35-16v) suffered severe acoustic attenuation from its high operating frequency (28 MHz), as seen in Figure 6.1b. Even using the maximum 8-cycle CE chirp to increase energy transmission, the ultrasound beam could not penetrate beyond the most superficial fascia. The resulting image is dominated by complete acoustic shadowing, leaving the underlying suprahyoid muscle and deeper anatomical structures entirely obscured. This baseline limitation directly justified shifting to a lower 14 MHz frequency configuration to balance spatial resolution and depth penetration.

Custom 14 MHz System Performance The ultrasound frames captured during Session II using the custom 14 MHz array, interfaced via the engineered fPCB platform, successfully demonstrated the structural validity and diagnostic potential of the selected frequency shift. As shown in Figure 4.13, the 14 MHz configuration effectively avoided the excessive acoustic attenuation that completely blinded the HF commercial probe during the December session.

The resulting image provides a reconstructed sector field of view, which directly reflects the hardware aperture reduction implemented to match the 128-channel limitation of the Verasonics Vantage platform, as previously detailed in Chapter 3. Because the outermost elements at both ends of the 192-element array were left as NC, a divergent steering transmission sequence was utilised to symmetrically widen the acoustic field in depth. Within this sector, multiple horizontal, hyperechoic interfaces are clearly discernible, tracking the acoustic boundaries between the subcutaneous fat and the superficial suprahyoid muscle layers.

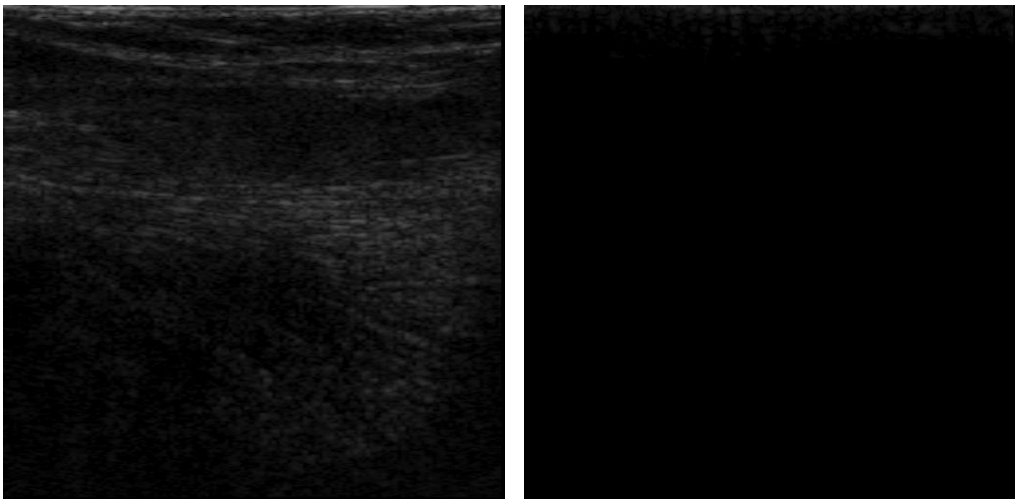

(a) **(b)**

Figure 4.12: Experimental imaging results on a cadaveric specimen from Session I (December): (a) low-frequency (LF) commercial probe (L11-5v) operating in standard mode, displaying deep anatomical landmarks in the submental/laryngeal region; (b) high-frequency (HF) commercial probe (L35-16v) operating at 28 MHz with an 8-cycle coded excitation (CE) chirp; the image is dominated by acoustic shadowing and attenuation, with no structural details discernible below the superficial fascia.

Additionally, a series of equidistant, parallel horizontal artifact lines can be observed traversing the deeper regions of the field of view. This phenomenon is hypothesised to be a multiple reverberation artifact arising from the experimental setup layout. Due to the high acoustic impedance mismatch between the anatomical specimen and the stainless-steel surface of the dissection table on which it was positioned, a near-total reflection of the ultrasonic wavefront likely occurred. Consequently, the acoustic energy trapped between this metallic boundary and the transducer face generated secondary echoes, which the beamformer reconstructed as deeper phantom structures.

Nevertheless, this outcome qualitatively confirms the electrical stability and signal integrity of the developed hardware interface under real-world experimental conditions, as the structural tissue layers remain identifiable despite the presence of these instrumental reverberations.

Clinical Benchmarking (SonixTouch Q$^+$ System) The reference scans acquired during Session II using the clinical system provided critical insights into the acoustic trade-offs of ultra-HF imaging in the submental region. Operating

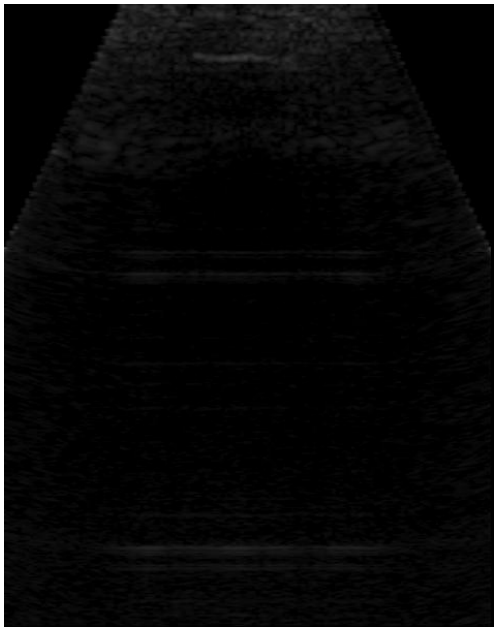

Figure 4.13: Submental transverse ultrasound scan acquired during Session II using the custom 14 MHz array. The field of view illustrates the successful penetration of the acoustic energy, with multiple hyperechoic lines tracking the horizontal tissue interfaces of the suprahyoid muscles.

at a transmission frequency of 30.0 MHz, the clinical scanner configured with the L40-8/12 transducer yielded a highly localised, narrow vertical field of view.

In the superficial region (within 2 cm of depth), the system demonstrates exceptional spatial resolution, clearly delineating the sharp, hyperechoic fascial interfaces of the superficial subcutaneous fat and the superior boundary of the anterior muscle layer. However, due to the severe acoustic attenuation characteristic of 30.0 MHz wavefronts in soft tissues, a reduction in structural contrast and boundary definition is observable beyond a depth of 2 cm. While acoustic energy still penetrates up to the 3 cm limit, the deeper muscle complexes essential for swallowing dynamics monitoring lose their distinct boundaries and cannot be reliably segmented within this acoustic window.

This outcome clinically justifies the development of the custom 14 MHz array framework, proving that a lower, optimised HF range is strictly necessary to balance the required spatial resolution with sufficient depth penetration for submental monitoring.

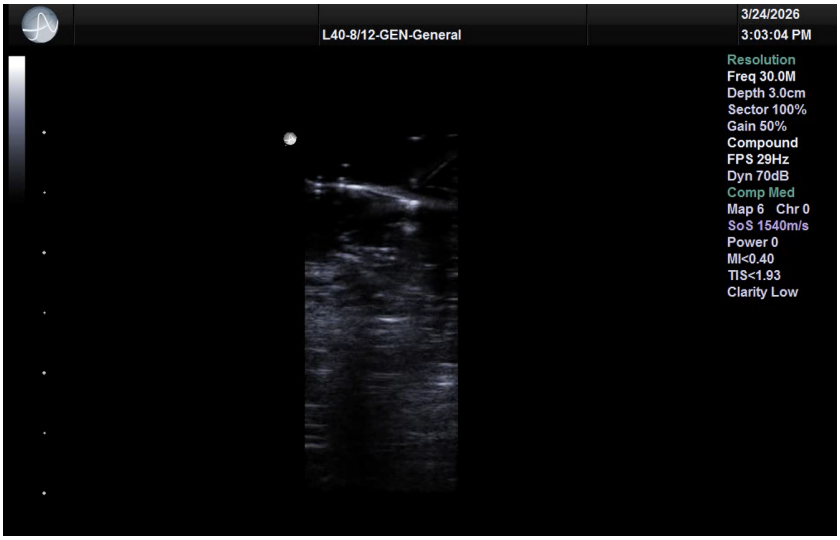

Figure 4.14: Reference submental transverse ultrasound scan acquired using the SonixTouch Q$^+$ clinical system during Session II, acquired at 30 MHz. The high-resolution image clearly delineates the superficial muscular stratification of the neck, alongside a reduction in structural contrast and boundary definition in the deeper regions due to acoustic attenuation.

4.3 Summary of Experimental Results

The experimental validation presented in this chapter successfully demonstrated the structural, functional, and hardware capabilities of the proposed ultrasound imaging strategy, moving systematically from material optimisation to *ex vivo* biological testing.

The initial phase focused on material characterisation, where a preliminary plain phantom was developed to verify the acoustic suitability and structural stability of the agar-based matrix. After establishing the baseline material properties, a more complex phantom replicated a cervical oesophageal stricture. Initial iterations had manufacturing inconsistencies and artifacts, but a systematic optimisation of the casting protocol resolved these issues, yielding a robust, anatomically accurate prototype.

When evaluated with the SonixTouch Q$^+$ clinical system, this optimised stenotic phantom allowed both morphological characterisation and functional testing. On a morphological level, testing the clinical system up to 30 MHz showed that extreme high frequencies suffer from excessive acoustic attenuation, failing to resolve deep oesophageal pathology. This result justified the custom 14 MHz framework. On

a functional level, a coordinated multi-operator protocol and custom mechanical interfaces enabled dynamic bolus testing, capturing transient fluid-structure interactions during simulated swallowing.

Following these controlled simulations, the final validation phase on cadaveric specimens tested the technology in a realistic biological setting. The December trials with commercial ultra-HF probes resulted in complete acoustic shadowing past the superficial fascia, even with a 8-cycle chirp CE. In contrast, the custom 14 MHz array framework bypassed these attenuation constraints. Interfaced via the engineered fPCB platform, the custom system reconstructed a field of view that clearly mapped the horizontal tissue interfaces of the suprahyoid musculature.

Qualitatively validated against the clinical references of the SonixTouch Q^+, these results confirm the structural robustness and signal integrity of the developed interface. Ultimately, while further hardware optimisations and software refinements will be necessary in future iterations, this work successfully establishes a verified and promising foundation for future wearable clinical translation.

Chapter 5

Comparative Analysis

While the initial criteria for selecting the 14 MHz transducer framework were qualitatively outlined in Section 3.1, this chapter provides a deeper quantitative evaluation of the experimental data. Analysing the reconstructed B-mode imaging datasets and their pixel intensity distributions allowed for a rigorous validation of the final system architecture performance. To this end, an initial integrity mapping is presented to investigate the structural and electrical constraints of the flexible thin-film prototype, justifying its exclusion from final imaging steps. Subsequently, a definitive quantitative benchmark is established between the selected custom 14 MHz rigid array and the HF commercial Verasonics probe, evaluating key image quality metrics extracted through a dedicated MATLAB post-processing pipeline.

5.1 Quantitative Evaluation of Prototype Constraints

Prior to performing the comparative imaging evaluations, an array integrity assessment was mandatory to benchmark the actual operational status of the evaluated transducers.

5.1.1 Assessment of the Flexible Prototype Integrity

As introduced in Chapter 3, the 25 MHz flexible thin-film array (Novosound, UK) was initially considered for its ideal wearable characteristics, being highly conformable to the irregular topography of the neck, lightweight, and capable of providing sub-millimetric spatial resolution. However, several critical limitations were anticipated prior to testing, including a low element count (32 elements) and an unusually wide pitch, which inherently complicates image reconstruction when conformed over complex skin surfaces.

During laboratory characterisation, the prototype exhibited severe structural and electrical degradation. To investigate this quantitatively, a channel-by-channel integrity mapping was analysed based on preliminary experimental data conducted by X. Miller across five distinct prototype samples from the same fabrication batch (denoted as Arrays #28, #29, #30, #32, and #35). The resulting connectivity matrix is illustrated in Figure 5.1 [57].

Each row in the matrix represents the specific electrical connectivity map of a single physical prototype, where functional channels are marked in green and non-operational or disconnected channels ("dead elements") are highlighted in red. The visual matrix highlights the severe fabrication consistency challenges of these flexible thin-film interfaces. Prototype #30 shows a high, continuous distribution of functional green channels. In contrast, the remaining samples exhibit severe connectivity failures. Arrays #32 and #35 show the worst degradation: their active aperture is almost entirely compromised, leaving only a few isolated functional elements.

When subjected to higher operational voltages (30 V in this particular case) on the Verasonics platform to compensate for the severe HF tissue attenuation, this thin-film flexible configuration exhibited a weak acoustic transmission signal and a high vulnerability to voltage stress. The clustered non-operational elements completely disrupt the spatial continuity of the active aperture, severely degrading the quality of the acoustic data and introducing heavy structural noise.

This structural degradation prevents reliable B-mode image reconstruction. Because of the severe channel dropout, the resulting frames suffer from massive vertical shadowing and geometric noise artifacts, making the isolation of consistent regions of interest impossible. This failure justified selecting the more stable, rigid transducer baseline for the subsequent quantitative imaging validation phases.

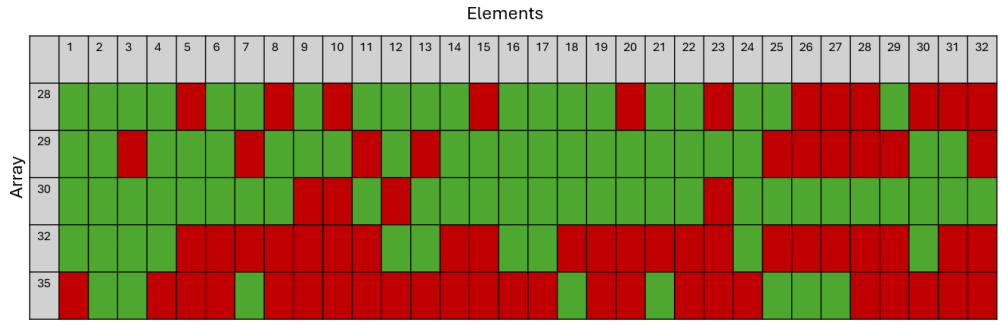

Figure 5.1: Experimental element mapping across five distinct prototypes of the 25 MHz flexible array. Green blocks represent fully operational elements, while red blocks indicate dead or disconnected elements resulting from manufacturing failures or structural stress (courtesy of X. Miller).

5.1.2 Rigid Array Integrity (14 MHz and 28 MHz)

The rigid substrates showed superior mechanical and electrical resilience compared to the flexible prototype. Both the conventional rigid 28 MHz array and the selected 14 MHz rigid hockey-stick transducer featured near-ideal aperture integrity, keeping close to 100% of elements active and functional during baseline checks. The lack of mechanical flexing on these configurations protected the acoustic crystal bonds and the connector solder joints, ensuring uniform transmission and reception across the active aperture. Consequently, the rejection of the 28 MHz iteration stemmed from acoustic penetration limits from ultra-HF tissue attenuation, rather than electrical degradation.

5.1.3 Signal Integrity and Acoustic Penetration Trade-offs

The experimental evaluation of the reconstructed data highlights the fundamental physical limits of the higher-frequency configurations compared to the developed 14 MHz rigid baseline:

- **High-Frequency Attenuation Validation:** For the rigid 28 MHz single-crystal array, experimental profiles confirmed that the acoustic attenuation coefficient drastically limits the penetration depth in biological tissue, preventing the visualisation of deeper structures within the stenotic phantom even when exploiting maximum contrast enhancement configurations.
- **Impact of Structural Degradation on Image Quality:** For the 25 MHz flexible array, the presence of severe artifacts, such as the vertical shadowing and heavy geometric noise observed during preliminary target scans, prevented any reliable statistical segmentation. Because the high density of dead elements compromised the spatial continuity of the active aperture, stable regions of interest could not be isolated. Consequently, quantitative image quality metrics could not be mathematically derived, validating the definitive exclusion of this prototype from the subsequent validation phases.

5.1.4 Direct Functional Validation of the 14 MHz Array via Imaging Tests

In contrast to the preliminary configurations, the operational performance of the 14 MHz unhoused array was validated directly through functional imaging tests using the completed custom hardware interface. Because the rigid hockey-stick geometry completely eliminates element position uncertainty and avoids the high-voltage dropout vulnerabilities of thin-film alternatives, a preliminary channel-by-channel characterisation was not required.

Instead, experimental scans evaluated the integrity of the entire system. Operating at a centre frequency of 13.3 MHz, the system demonstrated enough acoustic penetration depth to resolve deeper structures under attenuating conditions. This experimental result confirms that the custom fPCB interfaces are fully functional, establishing a stable baseline for the wearable ultrasound monitoring framework.

5.2 Quantitative Imaging Performance and MATLAB Validation

To definitively validate the performance of the selected 14 MHz rigid configuration, a quantitative comparative analysis was executed. A dedicated B-mode image processing pipeline was implemented in MATLAB to extract quality metrics from the reconstructed ultrasound frames, benchmarking the custom rigid 14 MHz array directly against the HF commercial Verasonics probe (L35-16vX, operating at a centre frequency of approximately 28 MHz).

The quantitative metrics, specifically CNR and SNR, were organised into a comparative framework, as summarised in Table 5.1. These metrics were computed using rectangular ROIs maintained at equivalent dimensions across the different image sections to ensure a consistent comparative analysis.

Table 5.1: Quality metrics comparison.

Transducer Configuration	CNR (Linear)	CNR (dB)	SNR (Linear)	SNR (dB)
L35-16vX Verasonics Probe	3.79	11.58	47.29	33.50
Custom Rigid 14 MHz Array	2.18	6.77	31.05	29.84

5.2.1 Acoustic Distribution Analysis

To evaluate the contrast resolution and statistical separation between the phantom structures, the probability density functions of the pixel intensities were extracted via histogram analysis, as shown in Figure 5.3.

The acoustic intensity distribution of the Verasonics probe (Figure 5.3a) highlights how severe HF attenuation affects image statistics. The agar matrix population (red) shows a broad Gaussian distribution centred around 0.48. This high value reflects the sensitivity and contrast resolution of the commercial crystals in the near-field. Conversely, the oesophageal lumen distribution (green) collapses almost entirely toward zero, overlapping tightly with the electronic noise floor peak

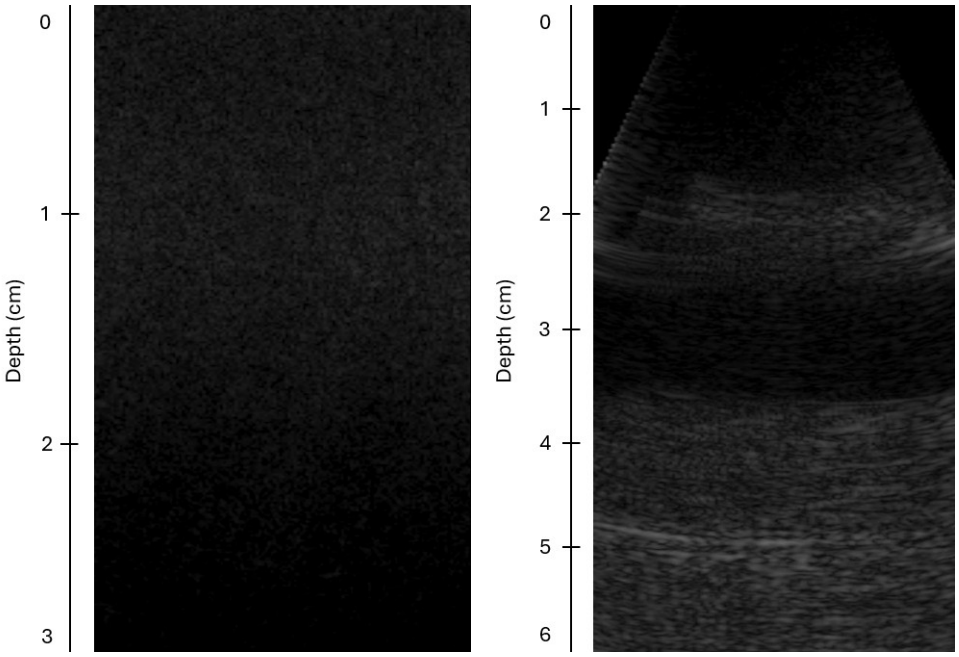

Figure 5.2: Reconstructed B-mode ultrasound scans of the stenotic oesophageal phantom: a) L35-16vX commercial probe showing high resolution but severe attenuation limiting depth to 3 cm; b) Custom rigid 14 MHz array demonstrating full acoustic penetration across the entire phantom structure. The depth axes represent an estimated scale based on the known geometric dimensions of the phantom.

(blue). Only a minimal, decaying tail extends from 0.02 to 0.25, marking the few superficial pixel structures that avoided complete attenuation. This overlap and the left-shift of the lumen population statistically prove signal dropout. The acoustic energy fails to penetrate deeper channel boundaries, reducing the dynamic range of the deeper region to the system's noise floor.

In contrast, the electronic noise floor for the 14 MHz array (Figure 5.3b) shows a sharp, narrow peak centred at zero, confirming a low-noise background. The oesophageal lumen (green) and the surrounding agar matrix (red) display two distinct, Gaussian-like distributions centred at approximately 0.10 and 0.27, respectively. While a minor acoustic overlap is observable between 0.10 and 0.20 due to local speckle interference near the structural boundaries, the statistical separation between the two profiles remains highly defined. This clear distribution separation provides experimental proof of the high contrast resolution achieved by the system, ensuring that the boundaries of the stenotic channel can be clearly segmented.

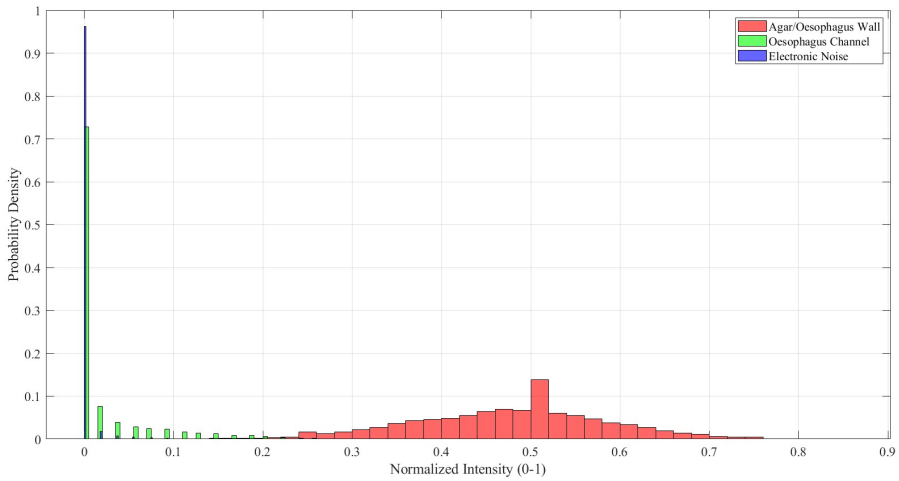

(a)

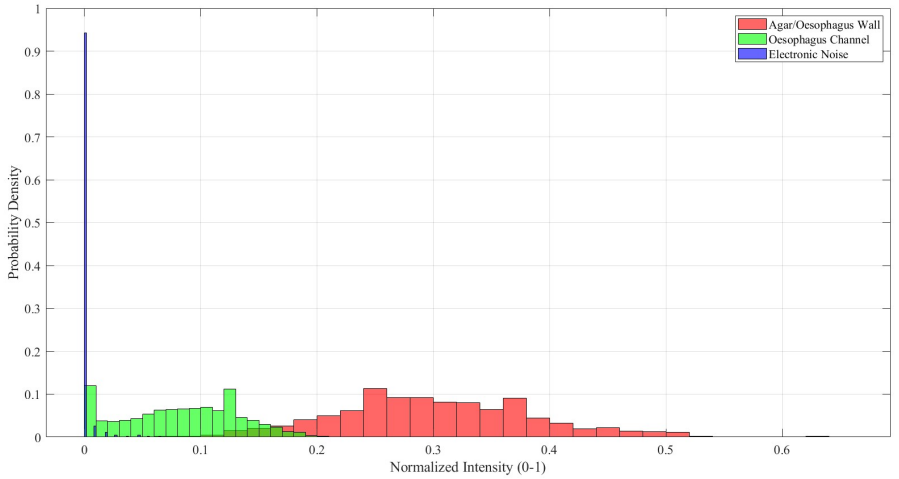

(b)

Figure 5.3: Acoustic intensity distribution analysis displaying the probability density of the agar wall (red), internal oesophageal channel (green), and background noise (blue): a) L35-16vX Verasonics probe; b) custom rigid 14 MHz array.

5.2.2 Axial Signal Intensity Profile and Penetration Depth

The ultrasound penetration capability was assessed by plotting the mean axial intensity profile, as illustrated in Figure 5.4. To maintain mathematical consistency, the signal intensity in decibels (dB) was normalised against the respective true

baseline noise floor of each configuration. This baseline corresponds to the initial anechoic water/gel coupling layer (water noise floor) for the custom 14 MHz array. Conversely, because the commercial Verasonics probe lacked this coupling stand-off layer and suffered from rapid HF decay, its baseline was extracted from the fully attenuated far-field region (electronic noise floor).

The axial profile of the 14 MHz array tracks the physical geometry of the phantom (Figure 5.4b). After the initial anechoic coupling water layer, discarded in the profile window to avoid near-field artifacts, the signal rises above 20 dB where the acoustic wave hits the anterior agar wall. It then sharply drops to 7 dB as it passes through the internal oesophagal lumen, before rising again symmetrically as it encounters the posterior wall.

Using a strict engineering safety threshold of 6 dB (where the signal power is at least twice the noise floor), the system computed a maximum penetration depth (MPD) of 75.78 mm for the 14 MHz configuration. It is crucial to note the signal intensity remains well above the threshold up to the geometric limit of the field of view. This indicates that the true acoustic penetration of the 14 MHz array within the agar matrix extends beyond the captured image boundaries, validating the structural sustainability of the phantom for deep imaging applications.

By comparison, the commercial probe's profile drops below the safety threshold rapidly at approximately 28.11 mm, due to the dominant HF attenuation (Figure 5.4a).

5.2.3 Summary of Analysis Results

The quantitative metrics summarised in Table 5.1 illustrate the fundamental physical trade-offs governing HF ultrasound imaging. In the superficial near-field region, the HF commercial Verasonics probe exhibits a clear superiority in terms of both CNR and SNR performance. Specifically, the commercial probe achieves a CNR of 11.58 dB (3.79 linear) compared to the 6.77 dB (2.18 linear) recorded for the custom system, alongside a higher SNR of 33.50 dB. This performance is a direct result of the superior manufacturing optimisation and the ultra-high centre frequency of the commercial crystals, which provide excellent spatial and contrast resolution, sharply separating the echogenic agar matrix from the anechoic oesophageal lumen, even thought partially visible. However, this elevated contrast resolution is band-limited due to the effects of acoustic attenuation at high frequencies. As demonstrated by the MPD analysis, the commercial probe signal drops below the 6 dB engineering safety threshold at a depth of just 28.1 mm, causing a complete loss of dynamic range and dynamic structure visualisation in the deeper regions of the phantom.

In contrast, the custom rigid 14 MHz array exhibits a highly stable and robust imaging profile. Although its localised near-field metrics are lower than the commercial benchmark due to the longer acoustic wavelength, this configuration

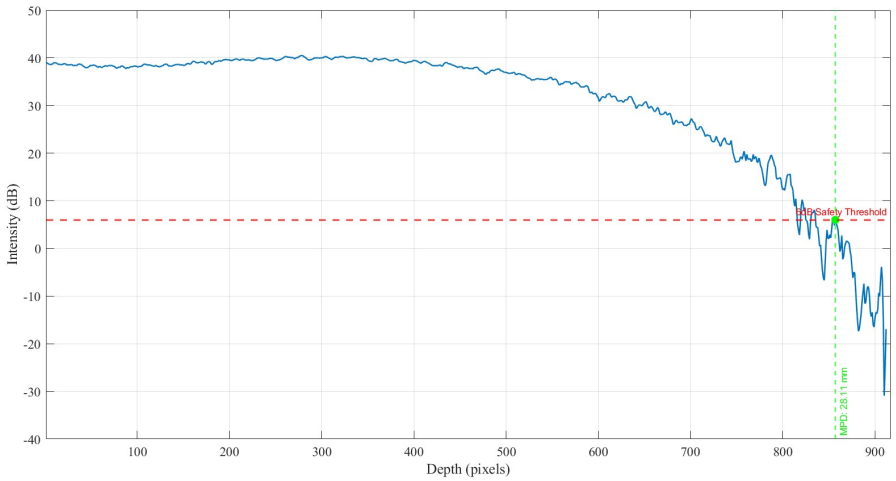

(a)

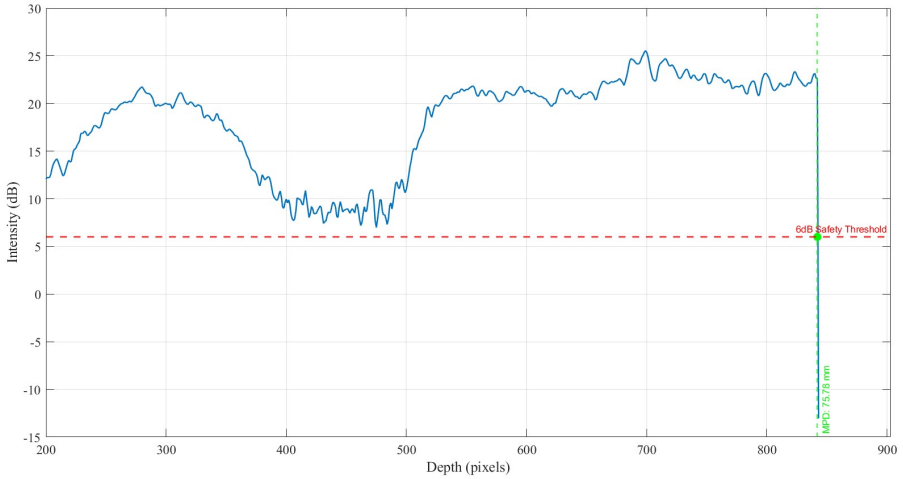

(b)

Figure 5.4: Comparison of the axial signal intensity profiles relative to their respective baseline noise floors, displaying the 6 dB safety threshold for Maximum Penetration Depth (MPD) detection: a) L35-16vX Verasonics probe; b) custom rigid 14 MHz array.

successfully preserves phase coherence and acoustic energy across a significantly wider field of view. It achieves a MPD of 75.78 mm, remaining above the safety threshold up to the geometric boundaries of the scan.

These quantitative findings validate the final system architecture. The commercial probe excels only in superficial resolution; conversely, the custom 14 MHz framework tracks the deeper anatomical boundaries of the stenotic oesophagus. This capability establishes the framework as a reliable baseline for a wearable ultrasound monitoring device. Ultimately, these results bridge the gap between controlled phantom simulations and complex biological environments, paving the way for real-time, non-invasive assessment of swallowing dynamics in clinical applications.

Chapter 6

Conclusions and Future Developments

This final chapter places the primary contributions of this research project into context, evaluating the technical and clinical impact on assistive biomedical technologies. It summarises the experimental and hardware objectives achieved throughout the thesis. A strategic roadmap outlines future research directions toward fully integrated, wearable submental ultrasound monitoring systems. Finally, based on these future milestones, an assessment of preliminary ergonomic investigations and collar mock-ups establishes the physical baseline for future wearable enclosures.

6.1 Impact of the Work

The research presented in this thesis addresses the critical need for high-resolution, wearable monitoring tools in the field of SLT and dysphagia rehabilitation. This work bridges the gap between custom hardware integration and experimental validation on synthetic and biological models, providing a comprehensive foundation for the next generation of real-time neck monitoring ultrasound devices. The impact of this research is characterised by three main contributions:

- **Methodological Innovation in Phantoms:** Research efforts were focused on a custom oesophageal phantom. The use of a tissue-mimicking tool allowed for the repeatable simulation of cervical oesophagus acoustic properties. The developed model serves as a preliminary proof-of-concept for swallowing and dysphagia and it offers a low-cost, high-reliability platform for future developments.
- **Clinical Benchmarking and Validation:** Tests with the SonixTouch Q^+ clinical system established a performance baseline. Using clinical equipment

validated the phantom's realism, providing a "ground truth" for future prototypes. Furthermore, human cadaveric specimen trials evaluated ultrasound propagation in real anatomical structures. This step highlighted the specific challenges of 14 MHz imaging in biological media.

- **Advanced Hardware Integration:** Interfacing the 14 MHz transducer array with the custom fPCB completed a technical step. Overcoming 0.15 mm pitch interconnection limits and defining a micro-soldering protocol provides a validated hardware platform. The system is now ready for future optimisation.

- **Strategic Frequency Selection:** This thesis defined the technical rationale for selecting the 14 MHz operating frequency. Evaluating the limits of previous higher-frequency prototypes guided the hardware integration. This choice balanced clinical relevance with technical feasibility for submental monitoring.

6.2 Summary of Final Results

The research objectives defined at the beginning of this project have been successfully achieved:

1. **Validation of the Oesophageal Phantom:** The custom-made phantom was successfully imaged and validated using clinical ultrasound systems. The results confirmed that the phantom accurately mimics the ultrasonic response of oesophageal tissues, positioning it as a useful tool for training and protocol development. It also showed clear potential for future dynamic testing to assess swallowing, dysphagia, and bolus transit.

2. **Hardware Integrity and Assembly:** The HF array was successfully integrated into the system, with stable electrical paths and mechanical robustness. Troubleshooting of the measurement set up provided critical data on the parasitic effects at high frequencies, which will inform future electronic shielding strategies and lay the groundwork for upcoming wearable system iterations.

3. **Anatomical Proof-of-Concept:** The imaging sessions carried out on cadavers gave a clear map of the 14 MHz array's performance and pave the way for the future use of CE techniques to optimise signal quality. Although the HF naturally limits penetration to superficial layers, the resolution achieved in the dermal and sub-dermal regions is highly promising for the purpose of targeted monitoring of superficial submental muscles.

6.3 Future Work

While the current work provides a solid hardware and experimental framework, several key research directions must be pursued to translate these findings into a functional clinical wearable device:

- **Integration, Comparative Analysis, and Software Optimisation:** The direct integration of the custom 14 MHz array with the experimental protocols developed on the stenotic oesophageal phantom has already been executed, as detailed in Chapter 5. Following these completed validation scans, the immediate next phase involves a comparative study between the clinical SonixTouch Q^+ data and the data acquired by the custom prototype to quantify sensitivity and resolution trade-offs. Concurrently, future work will focus on imaging algorithm improvements, implementing histogram equalisation and optimising SNR and CNR via improved 14 MHz imaging codes.

- **fPCB Scaling and Advanced Interfacing:** The current version of the custom fPCB was designed focusing on ease of assembly and troubleshooting, resulting in a bulky footprint. Proposals for future hardware iterations involve a significant reduction in dimensions, designing a slimmer and longer fPCB architecture. Using multi-layer rigid-flex technology and high-density interconnect strategies, the electronics can be miniaturised to fit within a compact, ergonomic enclosure. This scaling focuses on significantly reducing the hardware bulk and weight, avoiding an obtrusive footprint on the patient's neck. This has the benefit of ultimately maximising comfort and compliance during SLT tasks.

- **Advanced Signal Processing and Depth Optimisation:** To overcome the physical penetration constraints of HF ultrasound, future developments will investigate advanced beamforming techniques and targeted CE techniques. These methodologies aim to enhance acoustic penetration in deeper cervical structures without sacrificing the sub-millimetric spatial resolution of the 14 MHz transducer.

- **Ergonomic Design, Wearable Couplants, and Casing:** For SLT applications, the device must allow hands-free, unconstrained motion during dynamic tasks like speaking and swallowing. Preliminary ergonomic studies were conducted using a 3D-printed replica of the custom transducer integrated into a wearable fabric band setup to establish the baseline for optimal positioning on the neck. Future developments will focus on the engineering of a dedicated, flexible casing to ensure both structural protection for the fPCB and a comfortable, conformal fit during long-term dynamic monitoring.

- **Advanced Validation via Cadaveric Trials:** Finally, the optimised 14 MHz hardware setup, featuring the miniaturised interface and custom casing, will be validated through further, more extensive cadaveric trials at the University of Glasgow Anatomy Facility to confirm tracking robustness under realistic anatomical constraints.

6.3.1 Preliminary Ergonomic Study and Wearable Band Setup

To transition the hardware to a clinically viable wearable device, a preliminary study of ergonomics and positioning was carried out on an elderly volunteer. Figure 6.1 shows the qualitative evaluation: a practical test using a 3D-printed replica of the 14 MHz transducer array attached to an adjustable fabric band secured around the neck. Double-sided adhesive tape was used to hold the replica in place against the skin profile during trials, ensuring acoustic alignment and tilt angle. This prototype made it possible to assess the device's footprint and stability, how well the device sits on the neck and stays stable when applied to a real anatomical structure. In particular, trials evaluated the transducer's positioning within the submental region across transverse (coronal) and longitudinal (mid-sagittal) orientations. These two primary acoustic windows are necessary to track the floor of the mouth stratification, tongue dynamics, and hyoid bone movement during SLT.

Qualitative feedback from these trials highlighted acoustic contact is a challenge, keeping the transducer in consistent contact is challenging due to complex, surface geometries, the shape and curve of the neck. This challenge is especially noticeable in older adults: the primary target population for dysphagia rehabilitation. Observing how the prototype behaved during dynamic activities like jaw movement and speech production also provided crucial insights into how skin compliance, natural movement and elasticity of the skin, can affect sensor displacement.

Future work will focus on the design of a biocompatible enclosure that can house the electronics while maintaining consistent acoustic coupling with the skin, even during the rapid anatomical changes associated with swallowing.

6.4 Final Conclusions

Ultimately, relocating dysphagia management from bulky clinical setups to non-invasive devices requires a shift in continuous monitoring technologies. This thesis addressed this need by validating the trajectory from custom oesophageal phantom fabrication to the integration of a 14 MHz transducer array. The benchmarks from the SonixTouch Q^+ clinical system, alongside data from cadaveric trials, confirmed that targeted frequency selection can bypass traditional acoustic attenuation limits.

(a) **(b)**

Figure 6.1: Ergonomic and positioning study: (a) transverse (coronal) and (b) longitudinal (mid-sagittal) alignment of the 3D-printed transducer replica secured with an adjustable fabric band to evaluate physical footprint, stability, and contact compliance during dynamic jaw movements and speech production.

Consequently, continuous submental monitoring proves technically feasible. By establishing a bridge between advanced hardware design and rigorous experimental protocols, these combined milestones define a functional baseline for autonomous, long-term patient monitoring during remote rehabilitation.

Bibliography

[1] C. Schellen et al. «Management of Dysphagia in Head and Neck Cancer: Current and Future Perspectives». In: *Frontiers in Oncology* (2026). DOI: 10.3389/fonc.2026.1799956. URL: https://www.frontiersin.org/journals/oncology/articles/10.3389/fonc.2026.1799956/full.

[2] Royal College of Speech and Language Therapists. *Scope of Practice of Speech and Language Therapists*. 2026. URL: https://www.rcslt.org/.

[3] Nimrod M. Tole and Harald Ostensen. *Basic physics of ultrasonographic imaging*. Geneva, Switzerland: World Health Organization, 2013. ISBN: 978-92-4-159299-4.

[4] World Health Organization. *Rehabilitation*. 2024. URL: https://www.who.int/news-room/fact-sheets/detail/rehabilitation.

[5] Science Insights. *How ultrasound probe frequency affects image quality*. 2025. URL: https://scienceinsights.org/how-ultrasound-probe-frequency-affects-image-quality/.

[6] M. Loukas and D. Burns. *Essential Ultrasound Anatomy - Second Edition*. Wolters Kluwer, 2025. URL: https://internationalpbs.lwwhealthlibrary.com/book.aspx?bookid=3377&sectionid=0.

[7] A. Thapaliya et al. *Ultrasound Physics and its Application in Medicine*. PALNI Open Press, 2024.

[8] Peter Hoskins, Kevin Martin, and Abigail Thrush. *Diagnostic Ultrasound: Physics and Equipment*. 2nd. Cambridge, UK: Cambridge University Press, 2010.

[9] A. Benjamin, R. E. Zubajlo, et al. «A Novel Approach to the Quantification of the Longitudinal Speed of Sound and Its Potential for Tissue Characterization». In: *Ultrasound in Medicine & Biology* 44.12 (2018), pp. 2739–2748. DOI: 10.1016/j.ultrasmedbio.2018.07.021.

[10] Patsnap. *Longitudinal wave diagram*. https://eureka.patsnap.com/blog/wp-content/uploads/2024/11/longitudinal-wave2.png. 2024.

[11] RadiologyKey. *Ultrasound*. URL: https://radiologykey.com/ultrasound-13/.

[12] S. Jerban et al. «Quantitative Ultrasound Techniques Used for Peripheral Nerve Assessment». In: *Diagnostics* 13.5 (2023), p. 956. DOI: 10.3390/diagnostics13050956. URL: https://doi.org/10.3390/diagnostics13050956.

[13] J. Shepard. *How does voice recognition biometrics work?* 2024. URL: https://www.eeworldonline.com/how-do-voiceprint-recognition-biometrics-work/.

[14] P.M. Palmer. *Swallowing and its Disorders Across the Lifespan*. 2nd. New Mexico Open Educational Resources Consortium, 2026. URL: https://nmoer.pressbooks.pub/swallowingdisorders/.

[15] Artisynth Project. *Mastication and Swallowing Models - OPAL*. 2026. URL: https://www.artisynth.org/OPAL/MasticationAmpSwallowingModels.

[16] Macmillan Cancer Support. *Causes and risk factors of head and neck cancer*. 2026. URL: https://www.macmillan.org.uk/.

[17] S. L. Spaulding et al. «Diagnosis and management of pharyngoesophageal stenosis: A comprehensive approach to prophylactic, endoscopic, and reconstructive treatment options». In: *American Journal of Otolaryngology* 42 (5 2021). URL: https://www.sciencedirect.com/science/article/pii/S0196070921001046.

[18] E. Prisman, B.A. Miles, and E.M. Genden. «Prevention and management of treatment-induced pharyngo-oesophageal stricture». In: *The Lancet Oncology* 14.9 (2013). DOI: 10.1016/S1470-2045(13)70160-8. URL: https://linkinghub.elsevier.com/retrieve/pii/S1470204513701608.

[19] K. Maeda et al. «Ultrasonography for Eating and Swallowing Assessment: A Narrative Review of Integrated Insights for Noninvasive Clinical Practice». In: *Nutrients* 15.16 (2023), p. 3560. DOI: 10.3390/nu15163560. URL: https://www.mdpi.com/2072-6643/15/16/3560.

[20] National Cancer Institute. *Anatomy of the Esophagus*. 2026. URL: https://training.seer.cancer.gov/ugi/anatomy/esophagus.html.

[21] Encyclopædia Britannica. *The muscle groups and their actions*. 2026. URL: https://www.britannica.com/science/human-muscle-system#ref322750.

[22] S. Rothrie et al. «The role of the speech and language therapist in the rehabilitation of speech, swallowing, voice and trismus in people diagnosed with head and neck cancer». In: *British Dental Journal* 233 (2022), pp. 801–805. DOI: 10.1038/s41415-022-5145-2. URL: https://www.nature.com/articles/s41415-022-5145-2.

[23] Z. Dlamini et al. «Survivorship and Quality of Life in Head and Neck Cancer». In: *Navigating Head and Neck Cancer: Advances in Diagnosis and Treatment*. Oxford Academic, 2025. DOI: 10.1093/med/9780197794197.003.0011. URL: https://doi.org/10.1093/med/9780197794197.003.0011.

[24] American Cancer Society. *Cancer Facts and Statistics*. 2026. URL: https://www.cancer.org/research/cancer-facts-statistics.html.

[25] P. Clarke et al. «Speech and swallow rehabilitation in head and neck cancer: United Kingdom National Multidisciplinary Guidelines». In: *The Journal of Laryngology & Otology* 130 (2016). DOI: 10.1017/S0022215116000608. URL: https://www.cambridge.org/core/product/identifier/S0022215116000608/type/journal_article.

[26] E. Sugden, S. Lloyd, et al. «Systematic review of ultrasound visual biofeedback in intervention for speech sound disorders». In: *International Journal of Language & Communication Disorders* 54.5 (2019), pp. 705–728. DOI: 10.1111/1460-6984.12481.

[27] J. E. Allen, G. Clunie, et al. «Translating Ultrasound into Clinical Practice for the Assessment of Swallowing and Laryngeal Function: A Speech and Language Pathology-Led Consensus Study». In: *Dysphagia* 37.6 (2022), pp. 1681–1693. DOI: 10.1007/s00455-022-10413-9. URL: https://link.springer.com/10.1007/s00455-022-10413-9.

[28] J. Preston and N. R. Benway. *Video examples of treatment*. Open Science Framework (OSF). 2022. URL: https://osf.io/z7uet/.

[29] MedTech News Research. «Advancements in Ultrasound Technology and Applications in Healthcare: A Comprehensive Review». In: *MedTech News* (2025). URL: https://medtechnews.uk/research-reports/advancements-in-ultrasound-technology-and-applications-in-healthcare-a-comprehensive-review.

[30] W. Choi, Y. S. Cho, and others. «Role of point-of-care ultrasound in critical care and emergency medicine: update and future perspective». In: *Clinical and Experimental Emergency Medicine* 10.4 (2023), pp. 363–381. DOI: 10.15441/ceem.23.101.

[31] A. Matosova and L. Spreafico. *USES: UltraSound Evaluation of Swallowing*. 2026. URL: https://swallow-vision.com/uses/what-is-uses.

[32] British Medical Ultrasound Society (BMUS). *BMUS Guidelines for the Safe Use of Diagnostic Ultrasound Equipment*. 2026. URL: https://www.bmus.org/policies-statements-guidelines/safety-statements/.

[33] A. Jawli et al. «Tissue-Mimicking Material Fabrication and Properties for Multiparametric Ultrasound Phantoms: A Systematic Review». In: *Bioengineering* 11 (2024). DOI: 10.3390/bioengineering11060620. URL: https://www.mdpi.com/2306-5354/11/6/620.

[34] A. Sharma, S. G. Marapureddy, et al. «Characterizing Viscoelastic Polyvinyl Alcohol Phantoms for Ultrasound Elastography». In: *Ultrasound in Medicine & Biology* 49.2 (2023), pp. 497–511. DOI: 10.1016/j.ultrasmedbio.2022.09.019. URL: https://linkinghub.elsevier.com/retrieve/pii/S0301562922005798.

[35] R.M. Souza, T.Q. Santos, et al. «Standard operating procedure to prepare agar phantoms». In: *Journal of physics: conference series* 733 (2016).

[36] C. Sawhney et al. «Benefits and pitfalls of cadavers as learning tool for ultrasound-guided regional anesthesia». In: *Anesthesia: Essays and Researches* 11 (2017). DOI: 10.4103/0259-1162.186607. URL: https://journals.lww.com/10.4103/0259-1162.186607.

[37] MedBound Times. *Preservation Technologies in Anatomy Labs: Formalin vs Modern Alternatives*. 2026. URL: https://www.medboundtimes.com/medicine/formalin-vs-modern-cadaver-preservation-anatomy-labs.

[38] University of Dundee. *Thiel Cadaver Facility – Centre for Anatomy and Human Identification (CAHID)*. 2026. URL: https://www.dundee.ac.uk/locations/thiel-cadaver-facility.

[39] University of Glasgow. *Laboratory of Human Anatomy – School of Medicine, Dentistry & Nursing*. 2026. URL: https://www.gla.ac.uk/schools/medicine/anatomy/.

[40] J. L. Prince and J. M. Links. *Medical Imaging Signals and Systems*. 2nd. Pearson, 2014. ISBN: 978-0132145183.

[41] *Ultrasonics - Real-time pulse-echo scanners - Part 1: Describes methods for measuring performance systems*. Tech. rep. IEC 61391-1:2006+AMD1:2017. International Electrotechnical Commission (IEC), 2017.

[42] Verasonics Inc. *Vantage Research Ultrasound Systems*. Technical Description and Product Documentation. Kirkland, WA, USA, 2020.

[43] C. Weng, X. Gu, and H. Jin. «Coded Excitation for Ultrasonic Testing: A Review». In: *Sensors* 24 (2024), p. 2167. DOI: 10.3390/s24072167. URL: https://www.mdpi.com/1424-8220/24/7/2167.

[44] R.Y. Chiao and H. Xiaohui. «Coded excitation for diagnostic ultrasound: a system developer's perspective». In: *IEEE Transactions on Ultrasonics, Ferroelectrics and Frequency Control* 52 (2 2005), pp. 160–170. DOI: 10.1109/TUFFC.2005.1406543. URL: http://ieeexplore.ieee.org/document/1406543/.

[45] V. Perrot et al. «So you think you can DAS? A viewpoint on delay-and-sum beamforming». In: *Ultrasonics* 111 (2021). DOI: 10.1016/j.ultras.2020.106309. URL: https://linkinghub.elsevier.com/retrieve/pii/S0041624X20302444.

[46] T. Toosi and H. Benham. «Combined Pulse Compression and Adaptive Beamforming in Coded Excitation Ultrasound Medical Imaging». In: *IEEE - 2009 International Conference on Signal Processing Systems* (2009). DOI: 10.1109/ICSPS.2009.52. URL: http://ieeexplore.ieee.org/document/5166777/.

[47] X. Miller, A. Bruno, and others. «Array Selection for a Wearable Ultrasound Dysphagia Monitoring Biofeedback Device». In: *Book of Abstracts of the 1st IEEE Central and Eastern European Ultrasonics Symposium (CEEUS 2026)*. Warsaw, Poland, June 2026.

[48] Vermon. *LA 14.0/192-2100 Technical Datasheet*. France, 2021.

[49] *Narrow pitch connectors P5KF (0.5mm pitch) Datasheet*. Part Number: AXK5F70547YG. Panasonic Industry Co., Ltd. Osaka, Japan, 2026.

[50] *Product Specification for SS5/ST5 Series 0.50 mm Razor Beam LP Socket/-Header*. Part Number: SS5-80-3.00-L-D-K-TR. Samtec, Inc. New Albany, IN, USA, 2026.

[51] *Glasgow University Wiring Processing Drawing*. Chinese. Connector PN: AXK6F70547YG. Shenzhen Shenchao Transducer Co., Ltd. Shenzhen, China, 2026.

[52] IPC. *Sectional Design Standard for Flexible/Rigid-Flexible Printed Boards*. Tech. rep. IPC-2223E. Bannockburn, IL, USA: Association Connecting Electronics Industries, 2020.

[53] IPC. *Design Guide for High-Speed Printed Circuit Boards*. Tech. rep. IPC-2141A. Bannockburn, IL, USA: Association Connecting Electronics Industries, 2004.

[54] L. Buzzatto. «High Frequency Vibrational Shear Wave Elastography for the Characterisation of Soft Tissues». Master's thesis. Glasgow, UK: University of Glasgow, 2026.

[55] X. Miller. *Ultrasound Imaging Protocol: Obtaining radiofrequency (RF) & in-phase/quadrature (I,Q) data in fresh frozen cadavers*. Internal Research Protocol. In collaboration with the Center for Medical and Industrial Ultrasonics (CMIU). Glasgow, UK: Anatomy Facility, University of Glasgow, 2025.

[56] X. Miller. *Ultrasound Imaging Protocol: Obtaining radiofrequency (RF) & in-phase/quadrature (I,Q) data in fresh frozen cadavers using research prototype wearable ultrasound probe and BK medical imaging system*. Internal Research Protocol. Glasgow, UK: Anatomy Facility, University of Glasgow, 2026.

[57] X. Miller. *Ultrasound Technology for Wearable Imaging: Rigid vs Flexible Arrays*. Poster presented at the SINAPSE 2025 Annual Scientific Meeting (ASM). June 2025. URL: `https://abdn.eventsair.com/sinapse-asm2025/`.